

# **PROCEEDINGS**

**OF INTERNATIONAL CONFERENCE ON  
COMMUNICATIONS, ELECTROMAGNETICS AND MEDICAL  
APPLICATIONS (CEMA'07)**

Organized by:

**FACULTY OF COMMUNICATION TECHNIQUE AND TECHNOLOGIES  
OF TECHNICAL UNIVERSITY OF SOFIA, BULGARIA**

**NATIONAL TECHNICAL UNIVERSITY OF ATHENS, GREECE,  
SCHOOL OF ELECTRICAL AND COMPUTER ENGINEERING**

Sofia, Bulgaria  
25th – 27th October, 2007

**KING**

Edited by **Dimitar Tz. Dimitrov**

*All rights reserved. This book, or parts thereof, may not be reproduced in any form or by any means, electronic or mechanical, including photocopying or any information storage and the retrieval system now known or to be invented without written permission from the Publisher.*

**ISBN 978-954-9518-44-3**

Printed in Bulgaria



*D. Dimitrov*

*Dear Colleagues,*

The preparations for International Conference on 'Communication, Electromagnetics and Medical Applications' CEMA'07 have started. The conference will take place in Sofia, the capital and the leading scientific and cultural centre of Bulgaria. The following pages include a variety of information about the subject matter of the Conference, its program, the terms and conditions of participation and the city of Sofia. We hope that this information will encourage you to take part in this significant event. The final success of the Conference depends heavily upon your active participation. We hope that this Conference will provide you with full insight into European progress in Communication, Electromagnetics and Medical Applications.

Extended version of selected papers will be published in the 'Journal of Applied Electromagnetism':

*International Scientific Journal edited by the School of Electrical and Computer Engineering, National Technical University of Athens, Greece*

On behalf of the International Scientific Committee, we would like to invite you all to Sofia.

*Dimitar Tz. Dimitrov*  
*Conference Chairman*

## SCIENTIFIC PROGRAM

### *Opening ceremony*

25<sup>th</sup> October

09-09h30, room 12134 in 12<sup>th</sup> building

### FIRST SESSION

09h30-11h, room 12134 in 12<sup>th</sup> building

*Chairman: Prof. P. Frangos, NTUA, Athens, Greece*

---

1. *V. Demirev*, Faculty of Communications and Communication Technologies, TU-Sofia, Bulgaria,  
**SCP-RPSC Technology in the Feeder Lines of the LEO,s Communication System.**
2. *Jean Le Biham*, Ecole National d'Ingeniers de Brest, France,  
**Application of Z-transform for calculating locations and amplitudes extrema the case *sinc* related functions.**
3. *M. Schlimbach, J. Wahrburg, H. Roth*, University of Siegen,  
**A surgical planning software for orthopedic applications and its possible use in telemedicine**
4. *D. Tz. Dimitrov, P. Decheva, M. Gavrilov*, Faculty of Communications and Communication Technologies, TU-Sofia, Bulgaria,  
**Investigation on simultaneously influence of low frequency electrical signals with amplitude modulation and low frequency magnetic field on charged particles in the live tissue.**
5. *Dimitar Tz. Dimitrov, Petja Petrova, Borislav Tonev*, Faculty of Communications and Communication Technologies, TU-Sofia, Bulgaria,  
**Investigation on influence of low frequency interference electrical signals with frequency modulation on charged particles.**
6. *Dimitar Tz. Dimitrov, Stojanka Zajcheva, Miglena Donschewa*, Faculty of Communications and Communication Technologies, TU-Sofia,  
**Investigation on simultaneously influence of low frequency interference electrical signals and low frequency magnetic signals on ions in the live tissue.**

### *Coffe-break*

11h – 11h30



## SECOND SESSION

11h30 – 13h, room 12134 in 12<sup>th</sup> building

*Chairman: Prof. V. Demirev, TU-Sofia, Bulgaria*

---

1. *Mathieu Grau, Alexander Bekiarski, Pencho Venkov, Inna Nacheva*, Faculty of Communications and Communication Technologies, TU-Sofia,  
**Robot Control with Camera Eye.**
2. *Karakasiliotis<sup>(1)</sup>, G. Boultsadakis<sup>(1)</sup>, A. Lazarov<sup>(2)</sup> and P. Frangos<sup>(1)</sup>*, School of Electrical and Computer Engineering, National Technical University of Athens, 9 Iroon Polytechniou Street, 15773 Zografou, Athens, Greece <sup>(2)</sup>, Burgas Free University,  
**High-Resolution Stepped Frequency Inverse Synthetic Aperture Radar Imaging Using Time-Frequency Transforms.**
3. *L. Svilainis, V. Dumbrava, G. Motiejunas*, Signal processing department, Kaunas University of Technology, Kaunas, Lithuania,  
**Ultrasonic generator-transducer combined performance enhancement.**
4. *L. Svilainis, L. Sinkunas*, Signal processing department, Kaunas University of Technology,  
**Software considerations for ultrasonic data collection and evaluation systems.**
5. *Snejana Pleshkova-Bekiarska, Damian Damianov*, Faculty of Communications and Communication Technologies, TU-Sofia,  
**Simulation of Reverberation for Acoustic Teaching.**
6. *Marko Porjazoski, Borislav Popovski*, University “St’s Cyril and Methodius”, Faculty of Electrical Engineering and Information Sciences – Skopje, R. Macedonia,  
**Coverage predictions and performance analysis of single base station and cellular systems based on IEEE802.16 standart.**

### *Lunch*

13h – 14h

---

## THIRD SESSION

14h – 15h30, room 12134 in 12<sup>th</sup> building

*Chairman: Prof. A. Bekiarski, TU-Sofia, Bulgaria*

---

1. *B. Dekeris, L. Narbutaite*, Telecommunication department, Kaunas University of Technology, Kaunas, Lithuania,  
**The measurement of WLAN throughput using different security protocols.**
2. *Boncho Angelov Bonchev*, Faculty of Communications and Communication Technologies, TU-Sofia, Bulgaria,  
**Non-relativistic motion of ions in live tissues.**
3. *Boncho Angelov Bonchev*, Faculty of Communications and Communication Technologies, TU-Sofia, Bulgaria,  
**A motion of ions in live tissues under influence of permanent or low frequency magnetic field.**

4. *Valentin Panchev Hristov*, South- West University – Blagoevgrad, Bulgaria  
**A Simulation for WiMax networks.**
5. *M. Penhaker, J. Floder, M. Cerny, M. Rosulek*, VSB Technical University of Ostrava,  
Faculty of Electrical Engineering and Computer Science, Department Measurement  
and Control, Biomedical engineering laboratory,  
**ZigBee biotelemetry application**

### **Closing session**

15h30 – 16h, room 12134 in 12<sup>th</sup> building

---

## **SOCIAL PROGRAM**

### ***Banquet***

*October, 25<sup>th</sup>, 19h30*

### ***Trip to the Rila monastery***

*October 26<sup>th</sup>*

During the trip a lunch for the conference participants  
will be provided as its price is included in the conference fee

---

## **REGISTRATION**

**October, 25<sup>th</sup>, 09h – 16h**

The conference registration desk will be in the room 12134,  
12<sup>th</sup> building,  
Faculty of Electrotechnique, Technical University of Sofia

# INTERNATIONAL CONFERENCE

on

**Communications, Electromagnetics  
and Medical Applications**

**(CEMA'07)**

**Sofia, Bulgaria  
25th – 27th October, 2007**

*Organized by:*



**Faculty of Communication Technologies  
of TU-Sofia, Bulgaria**



**NATIONAL TECHNICAL  
UNIVERSITY OF ATHENS,  
GREECE**



**SCHOOL OF ELECTRICAL  
AND COMPUTER  
ENGINEERING**

## INTERNATIONAL SCIENTIFIC COMMITTEE

---

**Honorary Chairman:** Prof. NIKOLAOS K. UZUNOGLU,  
National Technical University of Athens, Greece

**Chairman:** D. C. DIMITROV,  
Technical University of Sofia, Bulgaria

**Vice Chairman:** P. FRANGOS,  
National Technical University of Athens, Greece

### MEMBERS:

I. ALIFERIS, University of Nice, France  
E. ALTIMIRSKY, Technical University of Sofia, Bulgaria  
N. AMPILOVA, University of Perersburg, Russia  
Q. BALZANO, University of Maryland, USA  
A. BEKJARSKY, Technical University of Sofia, Bulgaria  
J. CATRYSSSE, Katholieke Hogenschool Brugge Oostende, Belgium  
Ph. CONSTANTINOU, National Technical University of Athens, Greece  
J. DAUVIGNAC, University of Nice, France  
B. DEKERIS, Kaunas University of Technology, Litvania  
V. DEMIREV, Technical University of Sofia, Bulgaria  
M. DONTSCHEWA, University of Applied Sciences, Dornbirn, Austria  
V. DUMBRAVA, Kaunas University of Technology, Litvania  
D. EIDUKAS, Kaunas University of Technology, Litvania  
S. Ver HOEYE, University of Oviedo, Spain  
M. HOFMANN, University of Ulm, Germany  
V. HRISTOV, University of Blagoevgrad, Bulgaria  
I. ILIEV, Technical University of Sofia, Bulgaria  
R. KRIVICKAS, Kaunas University of Technology, Litvania  
G. MALLET, University "Sophia Antipolis", Nice, France  
R. De LEO, Università, Politecnica della Marche, Italy  
V. MARINKEV, Medical University of Plovdiv, Bulgaria  
M. MARTINS, Instituto Superior Técnico, Lisboa, Portugal  
K. NIKITA, National Technical University of Athens, Greece  
M. NIKOLOVA, High Naval School, Varna, Bulgaria  
M. PASTORINO, University of Genova, Italy  
J. PETROVSKA, Medical University of Sofia, Bulgaria  
Ch. PICHOT, University of Nice, France  
F. PRATO, University of Western Ontario, Canada  
A. SAVOV, Medical University of Sofia, Bulgaria  
L. SVILAINIS, Kaunas University of Technology, Litvania  
H-P. SCHADE, Technical University of Ilmenau, Germany  
L. SONG, Technical University of Harbin, China  
K. VLADIMIROV, Medical University of Sofia, Bulgaria

### CONTACT US:

<http://www.tu-sofia.bg/fktt/cema07/>  
<http://cema07.atspace.org>

## GENERAL INFORMATION

Submission of contributions  
Hotel reservation

### **Prof. Dr. Dimiter Dimitrov**

*Faculty of Communication Technique and Technologies  
Technical University of Sofia*  
8, Kliment Ohridsky str.  
1756 Sofia, Bulgaria  
Phone: ++359 2 9652278  
Fax: ++3592 9741360  
E-mail: [dcd@tu-sofia.bg](mailto:dcd@tu-sofia.bg)

### **Prof. P. Frangos**

*National Technical University of Athens  
School of Electrical and Computer Engineering*  
9, Iroon Polytechniou Str. ,  
157 73 Zografou, Athens, Greece  
Phone: 00 30 210 772 3694  
Fax: 00 30 210 772 2281  
E-mail: [pfrangos@central.ntua.gr](mailto:pfrangos@central.ntua.gr)

## REVIEWERS

---

N. AMPILOVA, Russia  
M. DONTSCHEWA, Austria  
F. KLETT, Germany  
V. HRISTOV, Bulgaria  
G. MALLET, France  
R. De LEO, Italy  
V. MARINKEV, Bulgaria  
M. MARTINS, Portugal  
M. NIKOLOVA, Bulgaria  
A. SAVOV, Bulgaria  
H-P. SCHADE, Germany  
L. SONG, China  
A. USHEVA, USA  
K. VLADIMIROV, Bulgaria  
E. BOEMO, Spain  
D. DIMITROV, Bulgaria

# TABLE OF CONTENTS

<b>SCP-RPSC TECHNOLOGY IN THE FEEDER LINES OF THE LEO,S COMMUNICATION SYSTEMS .....</b>	<b>1</b>
<i>Veselin Demirev</i>	
<b>INVESTIGATION ON SIMULTANEOUSLY INFLUENCE OF LOW FREQUENCY ELECTRICAL SIGNALS WITH AMPLITUDE MODULATION AND LOW FREQUENCY MAGNETIC FIELD ON CHARGED PARTICLES IN THE LIVE TISSUE.....</b>	<b>6</b>
<i>D. Tz. Dimitrov, P. Decheva, M. Gavrilov</i>	
<b>INVESTIGATION ON INFLUENCE OF LOW FREQUENCY INTERFERENCE ELECTRICAL SIGNALS WITH FREQUENCY MODULATION ON CHARGED PARTICLES .....</b>	<b>13</b>
<i>Dimitar Tz. Dimitrov, Petja Petrova, Borislav Tonev</i>	
<b>INVESTIGATION ON SIMULTANEOUSLY INFLUENCE OF LOW FREQUENCY INTERFERENCE ELECTRICAL SIGNALS AND LOW FREQUENCY MAGNETIC SIGNALS ON IONS IN THE LIVE TISSUE .....</b>	<b>16</b>
<i>Dimitar Tz. Dimitrov, Stojanka Zajcheva, Miglena Donschewa</i>	
<b>ROBOT CONTROL WITH CAMERA EYE .....</b>	<b>21</b>
<i>Mathieu Grau, Alexander Bekiarski, Pencho Venkov, Inna Nacheva</i>	
<b>HIGH-RESOLUTION STEPPED FREQUENCY INVERSE SYNTHETIC APERTURE RADAR IMAGING USING TIME-FREQUENCY TRANSFORMS .....</b>	<b>25</b>
<i>A. Karakasiliotis, G. Boulidakis, A. Lazarov, P. Frangos</i>	
<b>ULTRASONIC GENERATOR-TRANSDUCER COMBINED PERFORMANCE ENHANCEMENT .....</b>	<b>31</b>
<i>L. Svilainis, V. Dumbrava, G. Motiejunas</i>	
<b>SOFTWARE CONSIDERATIONS FOR ULTRASONIC DATA COLLECTION AND EVALUATION SYSTEMS .....</b>	<b>37</b>
<i>L. Svilainis, L. Sinkunas</i>	
<b>SIMULATION OF REVERBERATION FOR ACOUSTIC TEACHING .....</b>	<b>43</b>
<i>Snejana Pleshkova-Bekiarska, Damian Damianov</i>	
<b>COVERAGE PREDICTIONS AND PERFORMANCE ANALYSIS OF SINGLE BASE STATION AND CELLULAR SYSTEMS BASED ON IEEE 802.16 STANDARD .....</b>	<b>47</b>
<i>Marko Porjazoski, Borislav Popovski</i>	
<b>THE MEASUREMENT OF WLAN THROUGHPUT USING DIFFERENT SECURITY PROTOCOLS.....</b>	<b>54</b>
<i>B. Dekeris, L. Narbutaite</i>	
<b>NON-RELATIVISTIC MOTION OF IONS IN LIVE TISSUES .....</b>	<b>58</b>
<i>Boncho Angelov Bonchev</i>	
<b>A MOTION OF IONS IN LIVE TISSUES UNDER INFLUENCE OF PERMANENT OR LOW FREQUENCY MAGNETIC FIELD.....</b>	<b>62</b>
<i>Boncho Angelov Bonchev</i>	
<b>A SIMULATOR FOR WiMAX NETWORKS .....</b>	<b>66</b>
<i>Valentin Panchev Hristov</i>	
<b>ZIGBEE BIOTELEMETRY APPLICATION.....</b>	<b>69</b>
<i>M. Penhaker, J. Floder, M. Cerny, M. Rosulek</i>	
<b>APPLICATION OF Z-TRANSFORM FOR CALCULATING LOCATIONS AND AMPLITUDES OF EXTREMA: THE CASE OF SINC AND RELATED FUNCTIONS.....</b>	<b>74</b>
<i>Jean Le Bihan</i>	
<b>A SURGICAL PLANNING SOFTWARE FOR ORTHOPEDIC APPLICATIONS AND ITS POSSIBLE USE IN TELEMEDICINE .....</b>	<b>80</b>
<i>M. Schlimbach, J. Wahrburg, H. Roth</i>	

# SCP-RPSC TECHNOLOGY IN THE FEEDER LINES OF THE LEO,S COMMUNICATION SYSTEMS

Veselin Demirev

*Faculty of Communications and Communication Technologies,  
TU – Sofia, “Kl. Ohridsky” blvd. N8, 1756 – Sofia, Bulgaria,  
Phone 3592-965-26-60, E-mail: demirev\_v@tu-sofia.bg*

## Abstract

*The space segment of the future global satellite systems for broadband communications can be designed in a number of ways, depending on the orbital type of the satellites and the payload technology available on board. The use of different satellite orbits to provide complementary services, each optimised for the particular orbital type, is certainly feasible. Satellites can be used to connect with each other and the ground networks, through the use of Feeder Lines, Inter – Satellite Links or Inter-Orbit Links, which when combined with on-board routing facilities, can be used to form a network in the sky.*

*A new principle to realize the receiving satellite ground systems antennas - SCP was proposed by the author several years ago. The same approach - RPSC was investigated in transmit mode. The unique properties of the SCP-RPSC approach will give a new support for the future broadband LEO,s communication systems in the service feeder lines, intersatellite and interorbit lines domain. The possible applications of the SCP-RPSC technology in these microwave lines of several different types LEO,s constellations are considered in the report. A review of the possible advantages, supported by a critical analysis, is given too.*

*The conclusion is that the practical SCP-RPSC principles implementations in the feeder lines, intersatellite and interorbit lines will change the existing paradigm in the LEO and mixed LEO-GEO satellite communication business. Many of the existing problems of the proposed LEO, MEO and GEO satellite systems, dealing with the service lines as frequency and orbital resource sharing, beam pointing, station keeping characteristics, beam shadowing, etc., will be solved successfully.*

## 1. Introduction

A new principle to realize the receiving satellite ground systems antennas (Spatial Correlation Processing - SCP) was proposed in [1, 2, 3]. The same approach (Random Phase Spread Coding - RPSC) was investigated in transmit mode [4, 5]. Possible applications of SCP-RPSC technology in quasi-Geostationary satellite (GEO,s) systems [6], broadband High Altitude Platform Systems (HAPS) [7] and telemedicine [8] were reported by the author too. The listed areas of SCP-RPSC applications are in the field of the subscriber lines and terminals, where the low price and the abilities for mass production are of main interest. The unique properties of the SCP-RPSC approach will give a new support for the future broadband Low Earth Orbit satellite (LEO,s) communication systems in the service fee-

der lines domain. The possible applications of the SCP-RPSC technology in the feeder lines of several different types LEO,s constellations, using microwave frequency bands, are considered in the report.

## 2. The main LEO,s communication systems architectures

The space segment of the future global satellite systems for broadband communications can be designed in a number of ways, depending on the orbital type of the satellites and the payload technology available on board [9]. The use of different satellite orbits to provide complementary services, each optimised for the particular orbital type, is certainly feasible. Satellites can be used to connect with each other, through the use of Inter – Satellite Links (ISL) or Inter-Orbit Links (IOL), which when combined with on-board routing facilities, can be used to form a network in the sky. Fig.1, 2 and 3 shows a set of several possible Satellite-Personal Communication Network (S-PCN) architectures as identified by European Telecommunications Standards Institute (ETSI), concentrating on the use of LEO,s, which in some cases interwork with GEO,s. Here, a global coverage scenario is assumed, whereby a particular gateway is only able to communicate with a satellite providing coverage to one of the parties involved in establishing the mobile call. In this case, mobile-to-mobile calls are considered. Establishing a call between a fixed user and a mobile would require the mobile to form a connection with an appropriately located gateway.

In option *A* in Fig.1 transparent transponders are used in the space segment and the network relies on the ground segment Fixed Earth Stations (FES) to connect gateways. Satellites do not have the capability to perform ISLs. This option is used by the existing CDMA LEO,s system **Global Star**.

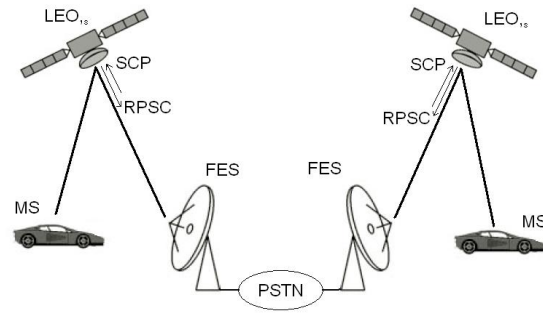


Figure 1. The satellite system architecture option A

The main problems of the FES-satellite feeder lines deal with the pointing of the high gain satellite antennas to the tracking FES antennas because of LEO,s continuous relative movement. For this reason low gain omnidirectional antennas are used in the LEO satellites at the moment. It leads to low feeder lines link margins and poor frequency reuse capabilities.

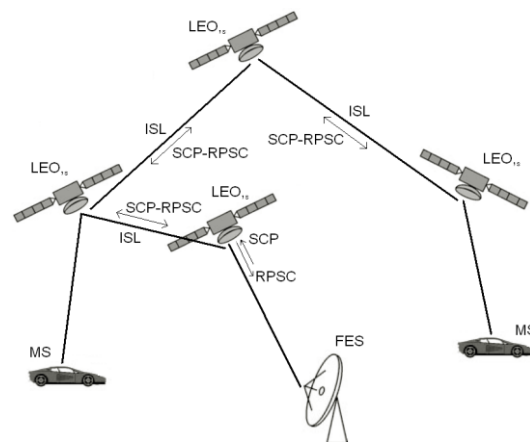
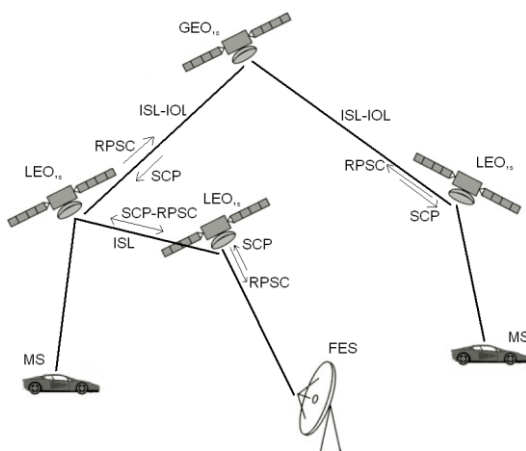


Figure 2. The satellite system architecture option B

Option *B* in Fig.2 uses ISLs to establish links with other satellites within the same orbital configuration. The ground segment may still perform some network functions but the need for FES is reduced. A mobile-to-mobile call may have delays of varying duration depending on the route chosen through the ISL backbone. This option is used by the famous **Iridium** LEO,s system.



The main problem of the existing ISL technology, used by *Iridium*, deals with the precise pointing of the narrow microwave antenna beams (the used frequencies are in 23 GHz band) and the need of tracking techniques to support the ISL work. It imposes very strong limitations over station keeping characteristics – about 2 km in cross-track, 5,7 km in-track and 4,7 km in radial direction [10]. The option A problems of the FES-satellite feeder lines, mentioned above, exist here too.



**Figure 3. The satellite system architecture option C**

In the final option C in Fig.3, a two-tier satellite network is formed through the use of a hybrid constellation. Inter-connection between LEO satellites is established through ISL, as in the previous case, and inter-satellite inter-orbit links (IOL) (ISL-IOL) via a data relay geostationary satellite is employed. In this configuration, the GEO satellite is directly accessed by an LEO,s. To the above mentioned problems of the LEO,s feeder lines and ISL we should add the similar problems of the pointing of the IOL narrow antenna beams of the mobile LEO satellites to the fixed GEO satellite positions.

### 3. Proposals for SCP-RPSC Technology Implementations in LEO,s feeder lines

The unique properties of the SCP-RPSC technology could be very useful if it will be implemented in the feeder lines, ISL and IOL of the future LEO satellite communication networks. In the analysis below the considered options A, B and C are discussed from SCP-RPSC technology implementation point of view.

#### A. Option A

The existing satellite omnidirectional antennas of the satellite-FES feeder lines can be replaced with SCP (up-link) and RPSC (down-link) with the following benefits:

#### SCP (up-link FES-LEO,s):

- The LEO,s receiving antenna systems will be omnidirectional for the cooperative FES, but with high figure of merit G/T.
- The different FES and polarizations could be selected simply by the use of specific allocated PN-codes.
- Soft handover between different FES is feasible because of the LEO,s movement and multiple beam forming properties of the SCP technology.
- Space diversity scheme: one LEO,s – several FES with possible frequency reuse is feasible too.

#### RPSC (down-link LEO,s-FES):

- Providing full duplex system with one simple and cheap transmit-receive antenna.
- The transmitted random poly-phase spread signals will not cause significant harmful interference to the conventional FES, using the same

frequency channels. The interference will be similar to that, caused by the sidelobes of a phased antenna array with random inter elements spacing.

- The transmitted random poly-phase spread signals are uniformly radiated in the space below the LEO,s. Several FES, equipped with the same SCP receivers and providing space diversity, receive them. The knowledge of the receiving FES positions for the transmitting LEO,s is not necessary.
- Close situated LEO,s could communicate with FES, using the same frequency channel without interference. The isolation between the LEO,s will be provided by their specific random phase spread coding, due to their specific random design.

### *B. Option B*

SCP-RPSC feeder lines FES-LEO,s: the same as option A.

SCP-RPSC ISL feeder lines:

The existing directional antennas of the ISL feeder lines can be replaced with SCP (both directions) and RPSC (both directions) with the following benefits:

- The virtual electronic scanning of the LEO,s ISL antenna patterns, typical for SCP-RPSC technology, will reduce significantly the limitations over station keeping characteristics and increase the satellite system reliability.
- LEO,s constellations with random orbits could be implemented instead the existing deterministic LEO,s orbits with their specific problems.

### *C. Option C*

SCP-RPSC feeder lines FES-LEO,s: the same as option A.

SCP-RPSC ISL feeder lines: the same as option B.

LEO,s-GEO,s IOL feeder lines:

The LEO,s omnidirectional antennas of the LEO,s – GEO,s IOL can be replaced with SCP (down-link) and RPSC (up-link) with the following benefits:

SCP (down-link GEO,s-LEO,s).

- The LEO,s receiving antenna system will be omnidirectional for the cooperative GEO,s, but with high figure of merit G/T.
- The different GEO,s and polarizations could be selected simply by the use of specific allocated PN-codes.
- Soft handover between different GEO,s is feasible because of the LEO,s movement and multiple beam forming properties of the SCP technology.
- Space diversity scheme: one LEO,s – several GEO,s with possible frequency reuse is feasible too.

RPSC (up-link LEO,s-GEO,s).

- Providing full duplex system with one simple and cheap transmit-receive antenna.
- The transmitted random poly-phase spread signals will not cause significant harmful interference to the conventional GEO,s, using the same frequency channels. The interference will be similar to that, caused by the sidelobes of a phased antenna array with random inter elements spacing.
- The transmitted random poly-phase spread signals are uniformly radiated in the space above the LEO,s. Several GEO,s, equipped with the same SCP receivers and providing space diversity, receive them. The knowledge of the recei-

ving GEO,s positions for the transmitting LEO,s is not necessary.

#### 4. Phased array antennas with electronic scanning – problems in space environment

Some of the above mentioned existing problems of the LEO,s feeder lines antennas could be solved by means of phased array antennas with electronic scanning. According to the author of the paper it will rise series of new problems, as follows:

- The radiation hazard of the space environment is very high for the electronic components of the unprotected active phased array antennas. It is not dangerous for the simple and passive Radial Line Slot Antennas (RLSA), used by SCP-RPSC technology.
- The temperature variations of the outer parts of LEO,s, where the antennas are situated, are in order of 400 deg. Very dangerous for active antennas too!
- The lack of the gases and humidity attenuations in space environment make the choice of W-frequency band very attractive. Phased array in this band are unpracticable, which is not the same for random RLSA, used in SCP-RPSC technology.

#### 5. Conclusion

The practical SCP-RPSC principles implementations in the feeder lines, intersatellite and interorbit lines will change the existing paradigm in the LEO and mixed LEO-GEO satellite communication business. Many of the existing problems of the proposed LEO, MEO and GEO satellite systems, dealing with the service lines as frequency and orbital resource sharing, beam pointing, station keeping characteris-

tics, beam shadowing, etc., will be solved successfully.

#### References

- [1] V. Demirev, "SCP technology – the new challenge in broadband satellite communications", *ICEST,04 Conference Proceedings*, pp.159-162, Bitola, Macedonia, 2004.
- [2] V. Demirev, A. Efremov, "SCP-CDMA GSO,s system proposal", *ICEST,04 Conference Proceedings*, pp.163-166, Bitola, Macedonia, 2004.
- [3] V. Demirev, "The Probability Theory with Application in SCP Technology", *ICEST,04 Conference Proceedings*, pp. 167-168, Bitola, Macedonia, 2004 .
- [4] V. Demirev, "Radiocommunication method and system with poly-phase spreading", *Bulgarian Patent Office applicant report*, N 106819/ 13.06.02.
- [5] V. Demirev, "Review of SCP-RPSC technology", *ICEST,05 Conference Proceedings*, vol. 2, pp.630-633, Nis, Serbia and Montenegro, 2005.
- [6] R. Markov, V. Demirev, "Application of SCP technology in quasi-GEO satellite systems", *ICEST,05 Proceedings of Papers*, Nis, Serbia and Montenegro, vol. 2, pp.519-521, June 29-July 1, 2005.
- [7] В. Демирев, М. Николова, "Приложение на технологията SCP-RPSC в широко-лентови HAPS", *Телеком,06*, Варна, 2006 г.
- [8] V. Demirev, "Broadband satellite SCP-RPSC communications – the new chance for the telemedicine", *CEMA,06*, Sofia, 2006.
- [9] R. Sheriff, Y. Fun Hu, *Mobile Satellite Communication Networks*, John Wiley & Sons, 2001.
- [10] D. Roddy, *Satellite Communications*, McGraw-Hill, 1996.

# INVESTIGATION ON SIMULTANEOUSLY INFLUENCE OF LOW FREQUENCY ELECTRICAL SIGNALS WITH AMPLITUDE MODULATION AND LOW FREQUENCY MAGNETIC FIELD ON CHARGED PARTICLES IN THE LIVE TISSUE

D. Tz. Dimitrov\*, P. Decheva\*\*, M. Gavrilo\*\*\*

*Technical University of Sofia, Bulgaria*

*\*Faculty of Communication Technique and Technologies of Technical University-Sofia, ,Kl.Ohridsky 8, 1000 Sofia,Bulgaria*

*\*\*Faculty of Computer Sciences of Technical University-Sofia, ,Kl.Ohridsky 8, 1000 Sofia, Bulgaria*

*\*\*\*Department of Physiotherapy of Alexander's University Hospital-Sofia, "G.Sofiisky"40 Sofia, Bulgaria*

## Abstract

*There are experimental evidences that electric and magnetic field, used simultaneously, can aid nerve regeneration and peripheral circulation as well as blood vessels regeneration and soft tissue healing.*

*There is a better analgesic and anti-phlogistic (anti-inflammatory) results when using both methods at the same time. So they are both used when healing arthritis, suppurative wounds and proceses.*

*In spite of that electrotherapy and magnetotherapy are widely used, there is not any program (these conclusion is made after some researches for that kind of program), used in practice, for visualization of their both influence of the humans. That is why the development of a software for that kind of visualization could contribute of more efficient use of those methods.*

## 1. Introduction

Nowadays, electrotherapy and magnetotherapy are more and more used in the field of medicine[...].

Electrotherapy is often used[...] in cases of damaged peripheral nerves,

but it is also worth much in cases of muscular atrophies after serious bone's fractures, and some other diseases.

Magnetotherapy is a method that uses the effect of the magnetic fields for the purposes of medical treatment. It uses either constant or low-frequency magnetic field. One of the most popular applications of magnetic field is to assist fractured bone repairing and healing[...].

## 2. Main text

It is interesting to see the cases when one electrical and one magnetic signal have influenced on a charged particle. Both signals are constant or low-frequency, and they are independent at each other. Each of them can vary in different way within time.

The location of the vectors of intensity of the electric field  $\vec{E}(x, y, z, t)$  and magnetic induction  $\vec{B}(x, y, z, t)$ , when both fields influence on the charged particle at the same time is shown on fig.1 in three-dimensional frame of reference XYZ.

For the very first moment it is accepted that the beginning of the frame of reference is exactly where the char-

ged particle is situated. Moreover, but without lessen the size of the examinations, it is accepted that the axes of the tree-dimensional frame of reference have a direction so the vector of magnetic induction of the magnetic field  $\vec{B}(x, y, z, t)$  coincide with the Z axis. The vector of intensity of the electric field  $\vec{E}(x, y, z, t)$  could be situated in every place in the space. Gamma ( $\gamma$ ) is the angle between  $\vec{E}(x, y, z, t)$  and the Z axis, and beta ( $\beta$ ) is the angle between the projection of  $\vec{E}(x, y, z, t)$  in XOY and the X axis.

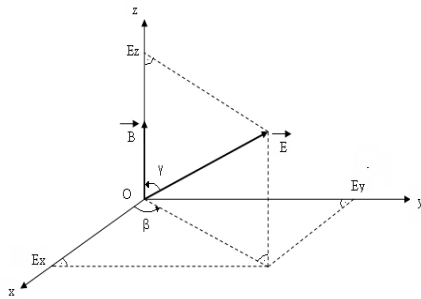


Fig. 1

The components of the vector  $\vec{E}(x, y, z, t)$  on the X,Y,Z axes of the frame of reference are  $E_x, E_y, E_z$ . A differential equation about the movement of the charged particle could be written in correspondence of fig.1. Generally the differential equation is:

$$m \frac{d^2 \vec{r}(t)}{dt^2} = q \vec{E}(x, y, z, t) + q \left[ \frac{d\vec{r}(t)}{dt} \times \vec{B}(x, y, z, t) \right] \quad (1)$$

Where:

$m$  is the mass of the charged particle;

$q$  is the electrical charge of the charged particle;

$\vec{r}$  is the tangential vector of the trajectory of movement of the charged particle.

According to fig.1 the components of the vector of intensity of the electric field of  $\vec{E}(x, y, z, t)$  are:

$$\begin{aligned} E_x &= |\vec{E}(x, y, z, t)| \sin \gamma \cos \beta \\ E_y &= |\vec{E}(x, y, z, t)| \sin \gamma \sin \beta \\ E_z &= |\vec{E}(x, y, z, t)| \cos \gamma \end{aligned} \quad (2)$$

The equation (1) could be written for each of the axes X, Y, Z. As a result the equation (1) turns out into a system of differential equations.

$$\begin{aligned} m \frac{d^2 x(t)}{dt^2} &= q [E(x, y, z, t) \sin \gamma \cos \beta + \\ &+ B(x, y, z, t) \frac{dy(t)}{dt}] \\ m \frac{d^2 y(t)}{dt^2} &= q [E(x, y, z, t) \sin \gamma \sin \beta + \\ &+ B(x, y, z, t) \frac{dx(t)}{dt}] \end{aligned} \quad (3)$$

$$m \frac{d^2 z(t)}{dt^2} = q E(x, y, z, t) \cos \gamma$$

The system of differential equations (3) has been written for the general case when the electric and the magnetic fields are non homogeneous, and when they are changing slowly (with low-frequency) into the time. All manner of mathematical expressions describing space-temporal configuration of the external low-frequently electrical and magnetic signals could be used into these differential equations.

The mostly examined case is when the charged particle is placed into a homogeneous electrical and magnetic field.

It is interesting when there is more complicated signal that influence upon the charged particle, for example, when the "external" electrical signal is ampli-

tude modulated. The algorithm for visualization the influence of the electrical

and magnetic field over the human's body is on the fig.2

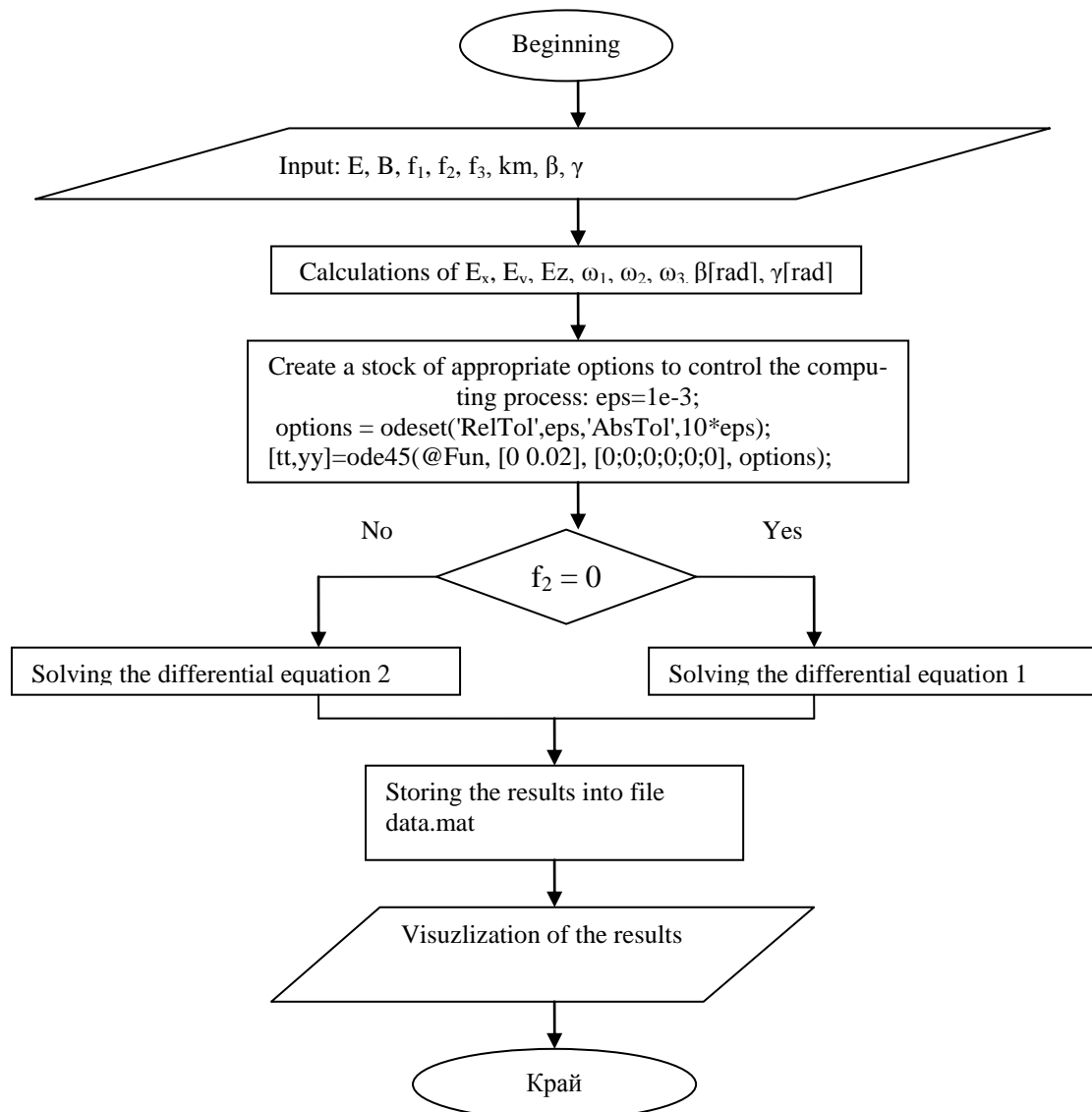


Fig. 2

### Description of the algorithm

Input is an interface for entering data. After that into the "Calculation" block the input data has been used for calculating  $E_x, E_y, E_z, \omega_1, \omega_2, \omega_3, \beta[\text{rad}], \gamma[\text{rad}]$ . The results of these calculations are necessary for the execution of the program. The next stage describes creating a stock of appropriate options to control the computing process. This one includes setting an appropriate accuracy of the calculations, choosing a

solver that gives best results using the common data for the examined cases, setting initial values for solving the differential equations.

The next "Condition" block defines if the chosen electrical signal is harmonious or if it is amplitude modulated. If  $f_2 = 0$ , it means that the signal is harmonious and the program continues with solving the differential equations 1. Otherwise the differential equations 2 would be solved. After that the results from the equations have been stored

into a file, named data.mat. These results will be used later as an input data of another program that calculates and visualizes the amplitude-frequency spectrums of the signals. The last step is visualization of the results in two- and three-dimensional graphics.

For the case when the charged particle is placed into homogeneous electrical and magnetic fields, the realized conditions are:

$$\begin{aligned}\vec{E}(t) &= \vec{E}_m \cos \omega_1 t \wedge \vec{E}_m(x, y, z) = \text{const} \\ \vec{B}(t) &= \vec{B}_m \cos \omega_3 t \wedge \vec{B}_m(x, y, z) = \text{const} \quad (4) \\ \beta &= \gamma = 45^\circ\end{aligned}$$

where:

$\vec{E}_m$  is the amplitude of the electrical intensity

$\omega_1$  is the circular frequency of intensity of the electrical field;

$B_m$  is the amplitude of the magnetic inductions;

$\omega_3$  is the circular frequency of the magnetic field;

In that case the system of differential equations is:

$$\begin{aligned}m \frac{d^2 x(t)}{dt^2} &= q[E_m \sin \gamma \cos \beta \cos \omega_1 t + \\ &+ \frac{dy(t)}{dt} B_m \cos \omega_3 t] \quad (5)\end{aligned}$$

$$\begin{aligned}m \frac{d^2 y(t)}{dt^2} &= q[E_m \sin \gamma \sin \beta \cos \omega_1 t + \\ &+ \frac{dx(t)}{dt} \cos \omega_3 t]\end{aligned}$$

$$m \frac{d^2 z(t)}{dt^2} = qE_m \cos \gamma \cos \omega_1 t$$

The solutions of the system are shown below in a graphic mode, and these solutions are calculated using concrete values of the parameters:

$$E_m = 200[V.m^{-1}]; \omega_1 = 2\pi 100[s^{-1}]$$

$$B_m = 30[mT], \omega_3 = 2\pi 50[s^{-1}]$$

The components of the trajectory of the movement of the charged particle are shown on fig.3 a, b and c. The trajectory of the movement of the charged particle in 3-D is shown on fig.3 d. It is obvious, from the system of differential equations, that the components of the “external” electrical signal take part in all of the equations of the system. . That is the reason that the electrical signal influences onto the components of the X, Y and Z axes of the trajectory and the speed of the charged particle. It is also obvious, that the components of the “external” magnetic signal take part only into the differential equations for the X and Y axes, so the magnetic signal influence onto the components of the trajectory and speed for X and Y axes only. The functions that describe the trajectory and speed over the Z component are periodic, and they are defined only by the function that describes the simple “internal” electrical harmonious signal.

Another interesting case is when the “external” electrical signal is amplitude modulated, and the magnetic signal is harmonious. In that circumstance, the conditions of influence from the “external” signals over the charged particle are:

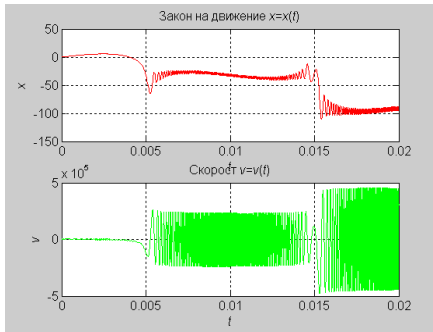
$$\begin{aligned}\vec{E}(t) &= \vec{E}_m (1 + m \cos \omega_1 t) \cos \omega_2 t \wedge \\ &\wedge \vec{E}_m(x, y, z) = \text{const} \wedge \vec{B}_m(x, y, z) = \text{const} \wedge \\ &\wedge \vec{B}(t) = \vec{B}_m \cos \omega_3 t \wedge \beta = \gamma = 45^\circ\end{aligned} \quad (6)$$

where:

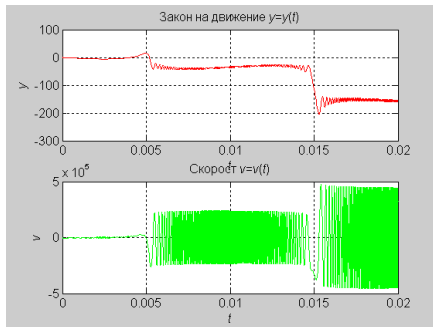
$\vec{E}_m$  is the amplitude of the electrical intensity;

$\omega_1$  is the circular frequency of intensity of the electrical field;

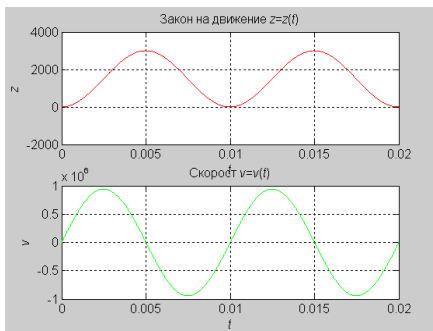
$\omega_2$  is the circular frequency of the carrier signal when there is an amplitude modulations of the intensity of electrical field;



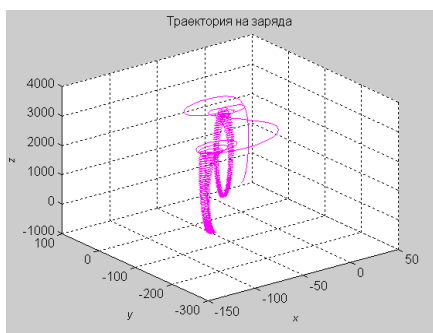
a)



b)



c)



d)

Fig. 3

In that case the system of differential equations is:

$$m \frac{d^2 x(t)}{dt^2} = q[E_m \sin \gamma \cos \beta (1 + m \cos \omega_1 t) \cos \omega_2 t + \frac{dy(t)}{dt} B_m \cos \omega_3 t] \quad (7)$$

$$m \frac{d^2 y(t)}{dt^2} = q[E_m \sin \gamma \sin \beta (1 + m \cos \omega_1 t) \cos \omega_2 t + \frac{dx(t)}{dt} \cos \omega_3 t]$$

$$m \frac{d^2 z(t)}{dt^2} = qE_m \cos \gamma (1 + m \cos \omega_1 t) \cos \omega_2 t$$

The solutions of the system are shown below in a graphic mode, and these solutions are calculated using concrete values of the parameters:

$$E_m = 200[V.m^{-1}]; \omega_1 = 2\pi 100[s^{-1}]$$

$$B_m = 30[mT], \omega_3 = 2\pi 50[s^{-1}]$$

$$\omega_2 = 2\pi 4000[s^{-1}], m = 1$$

The components of the trajectory of the movement of the charged particle are shown on fig.4 a, b and c. The trajectory of the movement of the charged particle in 3-D is shown on fig.4 d.

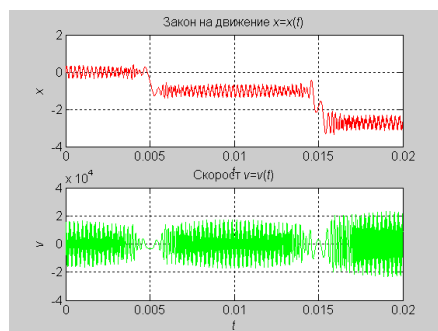
This case shows a very complicated process of amplitude modulation.

$m$  is the coefficient of the amplitude modulation;

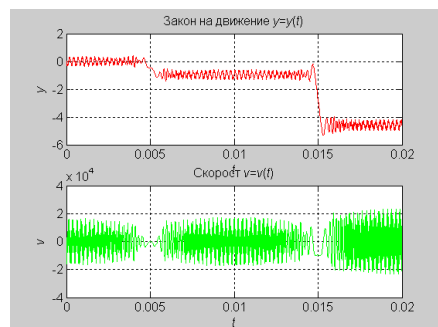
$B_m$  is the amplitude of the magnetic inductions

$\omega_3$  is the circular frequency of the magnetic field;

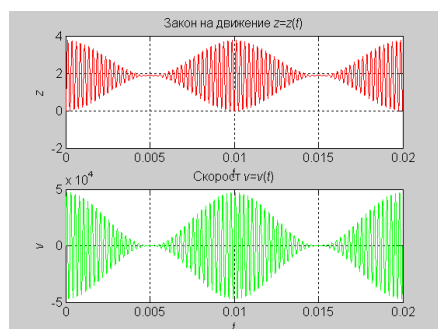




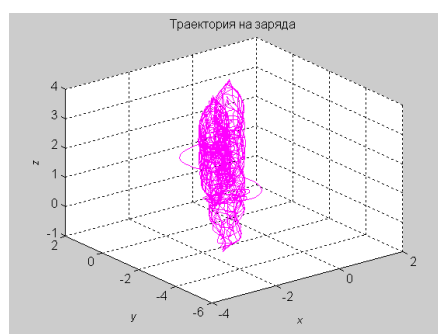
a)



b)



c)

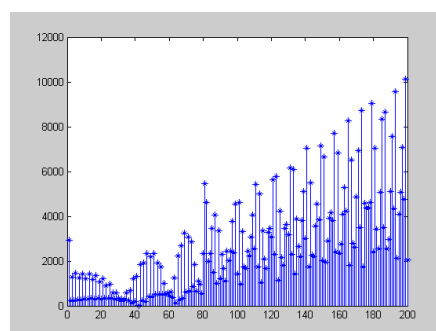


d)

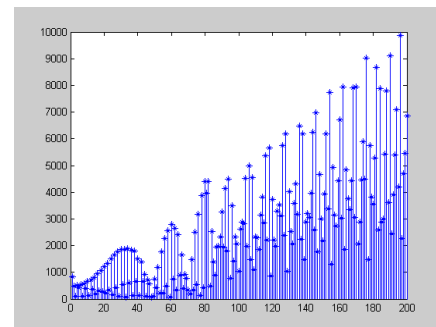
Fig. 4

### Spectral analysis

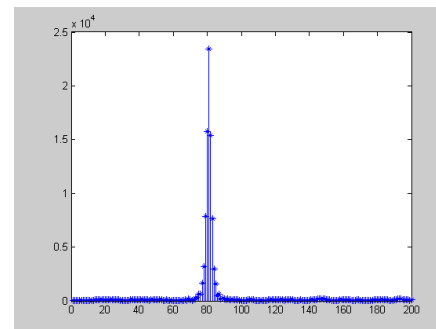
The results of the examination in the frequency area on the “internal” signals of the system, is shown below. The calculations of the amplitude-frequency spectrums are made by some computer methods.



a)



b)



c)

Fig. 5

Most interesting amplitude-frequency spectrums are those, when the “external” electrical signal is amplitude modulated and magnetic signal is low frequency sinusoidal signal. In this case the amplitude-frequency spectrums of the reaction of the system are, according to X, Y and Z axes (fig.5a, b, c). It's clear that there are many new components in the frequency spectrum in the “internal” electric signals as results of influence of two low frequency “external” signals on the human body.

## Conclusion

As result of the above investigation, a new method for therapy with simultaneously application of low frequency electrical and magnetic signals is obtained. This method has been checked in the Medical University of Sofia, Bulgaria and after its successful application, the method has been recommended in medical therapy.

## References

- [1] Dimitrov, D.Tz. Computer Simulation of Space Configuration of Low Frequency Magnetic Field in Magnetotherapy, Electronics and Electrical Engineering, Nr.3 (59), 2005, p.28-32.
- [2] Foley, J.D., A. van Dam, S. Feiner, J. Hughes, Computer Graphics: Principles and Practice, Addison-Wesley, Reading, MA,1990
- [3] Todorova,V. "3D Computer Simulation of the Static Magnetic Field Distribution over the Virtual Human Body", "Information Technologies and Control", ISSN 1312-2622, 2005
- [4] B. Тодорова, Ст. Малешков, "Geometric Data Exchange in XML format Using .NET Environment", Computer Science'2004, Technical University of Sofia, Bulgaria
- [5] Hearn, D., M. P. Baker. Computer Graphics, Prentice-Hall, NJ, 1997

# INVESTIGATION ON INFLUENCE OF LOW FREQUENCY INTERFERENCE ELECTRICAL SIGNALS WITH FREQUENCY MODULATION ON CHARGED PARTICLES

Dimiter Tz. Dimitrov\*, Petja Petrova\*\*, Borislav Tonev\*\*\*

Technical University of Sofia, Bulgaria

\*Faculty of Communication Technique and Technologies of Technical University-Sofia, ,Kl.Ohridsky 8, 1000 Sofia,Bulgaria

\*\*Faculty of Computer Sciences of Technical University-Sofia, ,Kl.Ohridsky 8, 1000, Sofia, Bulgaria

\*\*\*Medical University of Sofia, Departmet of Physiotherapy, Praga str.40

## Abstract

*There are some results about investigations of low frequency electrical currents on the human body. An description of influence and space configuration of two independent low frequency currents on the human body is done in the paper. The main results of investigation are connected with the case when one of the electrical signals is frequency modulated.*

## 1. Introduction

It's well known that the in the case of low frequency electromagnetic field it's possible to investigate the electrical and magnetic field separately [1,2,3]. In this case the vector of current density  $\vec{\delta}$  is connected with intensity of electrical field  $\vec{E}$  by the electrical conductance of live tissues  $\gamma$ .

$$\vec{\delta}(t) = \gamma \vec{E}(t) \quad (1)$$

Usually in the live tissues:

$$\gamma(x, y, z, t) \approx const \quad (2)$$

In this case the space configuration of the current density  $\vec{\delta}$  is the same as the space configuration of intensity of

electrical field  $\vec{E}$  [4,5]. So, it's possible to use the results on investigation of space configuration of intensity of electrical field  $\vec{E}$  for investigation of space configuration of of the current density  $\vec{\delta}$ .

## 2. Mathematical description

The space disposition of two pairs of patient's conductors can be seen on the fig.1. The two pairs of patient's conductors are connected to two independent low frequency generators of sinusoidal signals with different frequencies  $\omega_1$  and  $\omega_2$ , where:

$$\begin{aligned} \omega_1(t) = const \wedge \omega_2(t) \neq const \wedge \\ \wedge \omega_1(t) \neq \omega_2(t) \wedge \omega_1(t) \approx \omega_2(t) \end{aligned} \quad (3)$$

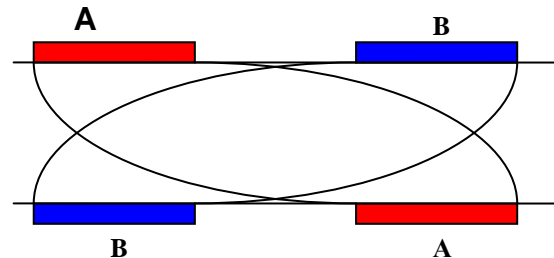


Fig. 1

The conductors A-A are connected with the first generator with the output tension  $U_1(t)$  and the conductors B-B are connected with the second generator with output tension  $U_2(t)$ , where:

$$U_1(t) = U_{1m} \cos \omega_1 t \quad (4)$$

$$U_2(t) = U_{2m} \cos \omega_2(t) \quad (5)$$

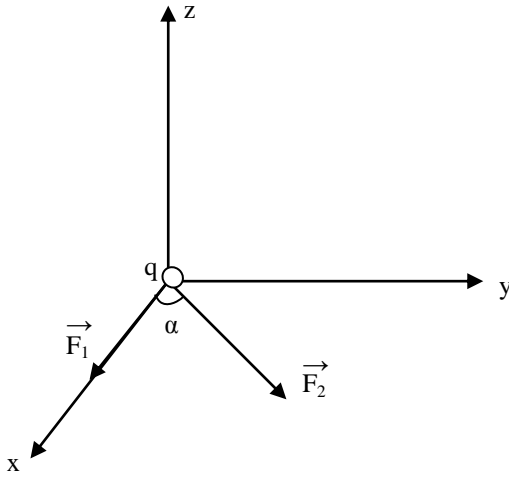


Fig. 2

In every moment and in every point in the space between two pairs of patient's conductors A-A and B-B there is an influence of two independent electrical forces  $\vec{F}_1$  and  $\vec{F}_2$  on every particle (ion) with mass  $m$  and electrical charge  $q$ . It would be easy for the next calculation if the ion is in the centre of coordinate system X,Y,Z (fig.2) and one of the forces  $\vec{F}_1$  is on the axis X. The angle between two forces is  $\alpha$ . It's clear that:

$$\vec{F}_1(t) = q\vec{E}_1 \cos \omega_1 t \quad (6)$$

$$\vec{F}_2(t) = q\vec{E}_2 \cos \omega_2 t \quad (7)$$

According to the main equation of the dynamic and fig.2:

$$\begin{cases} m\ddot{x} = \vec{F}_1(t) + \vec{F}_2(t) \cos \alpha \\ m\ddot{y} = \vec{F}_2(t) \sin \alpha \end{cases} \quad (8)$$

The components of velocity of ions on the two axis X and Y are:

$$\begin{cases} \dot{x} = \frac{1}{m} \int_0^t (\vec{F}_1(t) + \vec{F}_2(t) \cos \alpha) dt \\ \dot{y} = \frac{1}{m} \int_0^t \vec{F}_2(t) \sin \alpha dt \end{cases} \quad (9)$$

The components of movement of ions on the two axis X and Y are:

$$\begin{cases} x(t) = \frac{1}{m} \int_0^t \int_0^t (|\vec{F}_1(t)| + |\vec{F}_2(t)| \cos \alpha) dt dt \\ y(t) = \frac{1}{m} \int_0^t \int_0^t |\vec{F}_2(t)| \sin \alpha dt dt \end{cases} \quad (10)$$

Usually the electrical field between the two pairs of patient's conductors is homogeneity.

$$\vec{E}_1(h, y, z) = \text{const} \wedge \vec{E}_2(x, y, z) = \text{const} \quad (11)$$

Therefore in every point in the space between the patient's conductors:

$$E_1(t) = \frac{U_1}{l_1} \wedge E_2(t) = \frac{U_2}{l_2} \quad (12)$$

where:  $l_1, l_2$  are the respective distance between conductors A-A and B-B (fig.1).

Equations (12) can be put in the equations (6) and (7). Then the equations (6) and (7) can be put in the equations (8):

$$\begin{cases} \frac{d^2 x}{dt^2} = \frac{q}{m} \left( \frac{U_1}{l_1} \cos 2\pi f_1 t + \frac{U_2}{l_2} \cos \alpha \cos 2\pi f_2 t \right) \\ \frac{d^2 y}{dt^2} = \frac{qU_2}{ml_2} \sin \alpha \cos 2\pi f_2 t \end{cases} \quad (13)$$

It's clear that an optimization of the components of velocity and movement of ions on the two axis X and Y is possible by optimization of the value of angle  $\alpha$  and values of output tensions  $U_1(t)$  and  $U_2(t)$  of two generators. These components depend to the mass  $m$  and electrical charge of ions, according to the equation (9) and (10), also. The ion's current on the axis X and Y can be calculated by equations (14) and (15):

$$i_x(t) = \frac{q^2 s_x}{m} \left( \frac{U_1}{2\pi f_1 l_1} \sin 2\pi f_1 t + \frac{U_2 \cos \alpha}{2\pi f_2 l_2} \sin 2\pi f_2 t \right) \quad (14)$$

$$i_y(t) = \frac{q^2 s_y U_2 \sin \alpha}{2\pi f_2 m l_2} \sin 2\pi f_2 t \quad (15)$$

Where:

$f_1$  and  $f_2$  are the frequencies of two generators;

$s_x$  and  $s_y$  are the sections of ion's flows on the axis X and Y.

The ions of  $Na^+$  and  $Cl^-$  are the main kind of ions in the human body. For example the trajectory of ions of  $Cl^-$  can.

be seen on fig.3 in the case of following parameters:

$$U_{1m} = 15V, U_{2m} = 30V, \alpha = 45^\circ,$$

$$f_1 = 4000[Hz], f_2 = 4000 - 4100[Hz]$$

$$l_1 = l_2 = 0,08[m]$$

The output signal of the second generator is frequency modulated and the deviation is:  $\Delta f = 100[Hz]$ . The dimensions on the axis X and Y are  $[m \cdot 10^{-2}]$ .

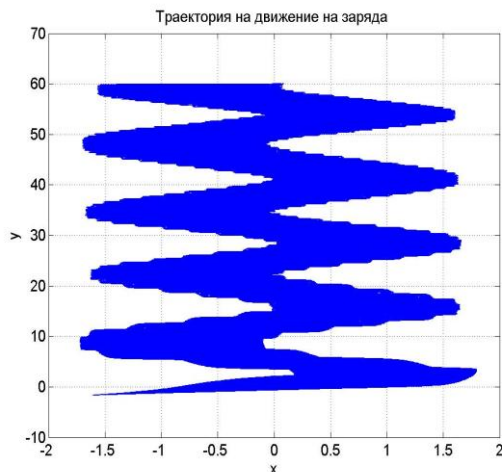


Fig. 3

The moment trajectory of the ions can be seen on fig. 4. Usually these kind of therapy is used in medicine in physiotherapy for reducing

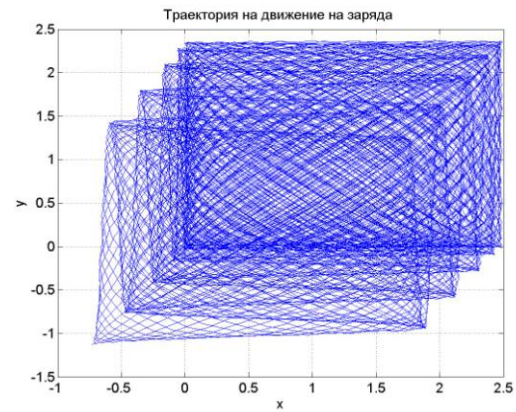


Fig. 4

of pain. An application of this method in the case where the pain is in the foot can be seen on fig.5.

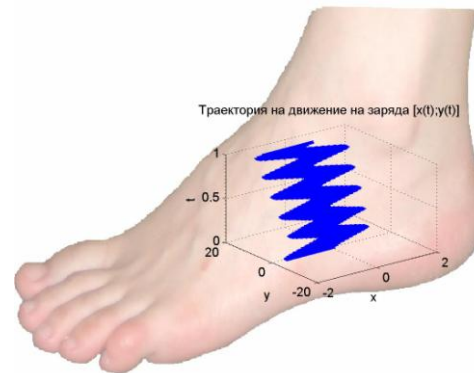


Fig. 5

## Conclusion

A mathematical description and computer visualization of movement of ions in the live tissues is described in the paper.

The results of investigations can be used for obtaining of more good effect in the process of therapy with interferent currents.

## References

- [1] Hristov, V. A MODIFICATION OF PUSH-OUT MECHANISM. Proc. of the Conference Computer Science'2005, Chalkidiki, Greece, 30 September – 2 October, 2005, Part I, pp. 37- 41.
- [2] Hristov, V., and V. Vatchkov, Web based system for microscope observation with structural analyzer EPIQUANT, Engineering Science Magazine, 2006, No 2, pp. 17-24.

# INVESTIGATION ON SIMULTANEOUSLY INFLUENCE OF LOW FREQUENCY INTERFERENCE ELECTRICAL SIGNALS AND LOW FREQUENCY MAGNETIC SIGNALS ON IONS IN THE LIVE TISSUE

Dimiter Tz. Dimitrov\*, Stojanka Zajcheva\*\*, Miglena Donschewa\*\*\*

Technical University of Sofia, Bulgaria

\*Faculty of Communication Technique and Technologies of Technical University-Sofia, ,Kl.Ohridsky 8, 1000 Sofia,Bulgaria

\*\*Faculty of Computer Sciences of Technical University-Sofia, ,Kl.Ohridsky 8, 1000 Sofia,Bulgaria  
University of Applied Sciences, Vorarlberg, Austria

## Abstract

*An investigation of simultaneously influence of two low frequency electrical signals and one magnetic signals on the ions in the live tissue is described in the paper. The results of computer simulation of the movement of ions is shown. The investigations are in connections with medical application of electrotherapy (application ointerferent currents) together with magnetotherapy.*

## 1. Introduction

The clinical results obtained by separate application of interferent currents and low frequency or permanent magnetic field are well known in medicine[...]. Nevertheless the results of investigation on the movement of ions in the live tissue provided by influence of external low frequency electrical or magnetic field are not known. There are not scientific results in medicine and in engineering, also on simultaneously application of low frequency electrical and magnetic field on the human body. These investigations are the goal of the present paper.

## 2. Mathematical description

The two low frequency electrical field are provided by two independent

generators. The output tensions  $U_1$  and  $U_2$  are on the respective pair patient's conductors A-A and B-B (fig.1)

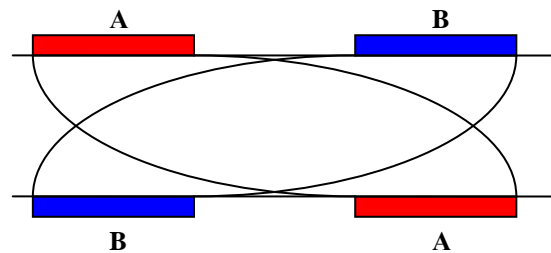


Fig. 1

The space disposition of the vectors of two electrical forces  $\vec{F}_1$  and  $\vec{F}_2$  and the vector of magnetic induction  $\vec{B}$  can be seen on fig.2.

The ion with masse  $m$  and electrical charge  $q$  is situated in the centre of co-ordinate system  $X,Y,Z$ . There are influence of three forces  $\vec{F}_1, \vec{F}_2, \vec{F}_3$  on the ions.

$$\vec{F}_1(t) = q\vec{E}_{1m} \cos \omega_1 t \quad (1)$$

$$\vec{F}_2(t) = q\vec{E}_{2m} \cos \omega_2 t \quad (2)$$

$$\vec{F}_3(t) = q(\vec{V} \times \vec{B}_m \cos \omega_3 t) \quad (3)$$

where:

$U_1$  and  $U_2$  are the tensions on the two pairs of patient's conductors;

$\omega_1$  and  $\omega_2$  are the frequencies of the two independent generators;

$\vec{E}_1, \vec{E}_2$  are the intensities of the two electrical fields;

$\vec{B}$  is the magnetic induction in the point of particle;

$V$  is the velocity of particle.

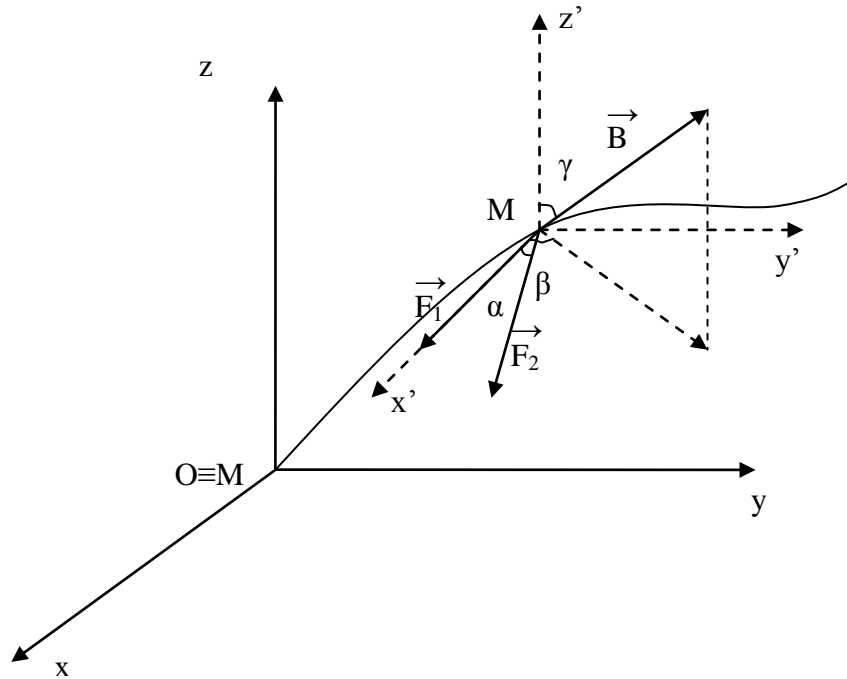


Fig. 2

$$\vec{F}_1(t) = \vec{i}F_{1x}(t) + \vec{j}F_{1y}(t) + \vec{k}F_{1z}(t) \quad (4)$$

$$\vec{F}_2(t) = \vec{i}F_{2x}(t) + \vec{j}F_{2y}(t) + \vec{k}F_{2z}(t) \quad (5)$$

$$\vec{F}_3(t) = \vec{i}F_{3x}(t) + \vec{j}F_{3y}(t) + \vec{k}F_{3z}(t) \quad (6)$$

where:

$\vec{i}, \vec{j}, \vec{k}$  are the single vectors on the axis X, Y and Z;

$F_{1x}, F_{1y}, F_{1z}$  are the components of  $\vec{F}_1$  on the axis X, Y, Z;

$F_{2x}, F_{2y}, F_{2z}$  are the components of  $\vec{F}_2$  on the axis X, Y, Z;

$F_{3x}, F_{3y}, F_{3z}$  are the components of  $\vec{F}_3$  on the axis X, Y, Z.

If the superposition can be used:

$$\vec{F}(t) = \vec{F}_1(t) + \vec{F}_2(t) + \vec{F}_3(t) \quad (7)$$

The equations (8), (9) and (10) are the equations of movement of charged particle under simultaneously influence of two electrical fields and magnetic field.

$$m \frac{d^2 x(t)}{dt^2} = F_x(t) = F_{1x}(t) + F_{2x}(t) + F_{3x}(t) \quad (8)$$

$$m \frac{d^2 y(t)}{dt^2} = F_y(t) = F_{1y}(t) + F_{2y}(t) + F_{3y}(t) \quad (9)$$

$$m \frac{d^2 z(t)}{dt^2} = F_z(t) = F_{1z}(t) + F_{2z}(t) + F_{3z}(t) \quad (10)$$

where:

$x(t), y(t), z(t)$  are the components of movement of the charged particle.

$$\begin{cases} F_{1x} = qE_1 \cos \omega_1 t \\ F_{1y} = 0 \\ F_{1z} = 0 \end{cases} \quad (11)$$

$$\begin{cases} F_{2x} = qE_2 \cos \alpha \cos \omega_2 t \\ F_{2y} = qE_2 \sin \alpha \cos \omega_2 t \\ F_{2z} = 0 \end{cases} \quad (12)$$

$$\vec{F}_3 = q(\vec{V} \times \vec{B}) = q \begin{vmatrix} \vec{i} & \vec{j} & \vec{k} \\ V_x & V_y & V_z \\ B_x & B_y & B_z \end{vmatrix} \quad (13)$$

where:

$$\begin{cases} V_x = \frac{dx(t)}{dt} \\ V_y = \frac{dy(t)}{dt} \\ V_z = \frac{dz(t)}{dt} \end{cases} \quad (14)$$

$$\begin{cases} B_x = B \sin \beta \sin \gamma \cos \omega_3 t \\ B_y = B \cos \beta \sin \gamma \cos \omega_3 t \\ B_z = B \cos \gamma \cos \omega_3 t \end{cases} \quad (15)$$

Finally:

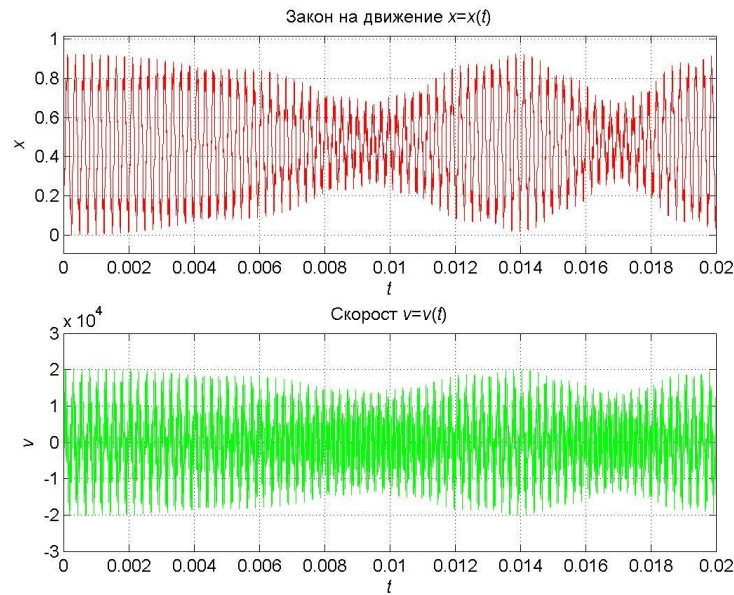
$$\begin{aligned} m \frac{d^2 x(t)}{dt^2} = & q \left( \frac{U_{1m}}{l_1} \cos \omega_1 t + \right. \\ & + \frac{U_{2m}}{l_2} \cos \alpha \cos \omega_2 t + \\ & + q \left[ \frac{dy(t)}{dt} \cos \gamma - \right. \\ & \left. \left. - \frac{dz(t)}{dt} \sin \gamma \sin \beta \right] B \cos \omega_3 t \right) \end{aligned} \quad (16)$$

$$\begin{aligned} m \frac{d^2 y(t)}{dt^2} = & q \frac{U_{2m}}{l_2} \sin \alpha \cos \omega_2 t + \\ & + q \left[ \frac{dz(t)}{dt} \sin \gamma \cos \beta - \right. \\ & \left. - \frac{dx(t)}{dt} \cos \gamma \right] B \cos \omega_3 t \end{aligned} \quad (17)$$

$$\begin{aligned} m \frac{d^2 z(t)}{dt^2} = & q \left[ \frac{dx(t)}{dt} \sin \beta \sin \gamma - \right. \\ & \left. - \frac{dy(t)}{dt} \cos \beta \sin \gamma \right] B \cos \omega_3 t \end{aligned} \quad (18)$$

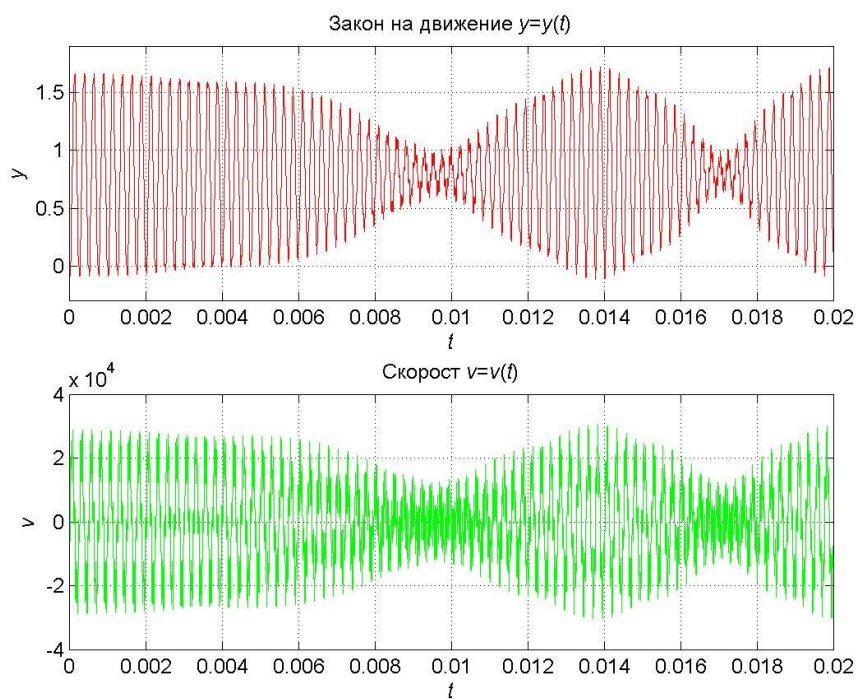
The investigations have been done in the case when the signal of the second generator is frequency modulated. The results of computer simulation of components of movements and velocity on the three axis X,Y,Z in the case of ions of  $Na^+$  can be seen on fig.3. The parameters for this investigation are:

$$\begin{aligned} f_1 = 4000 \text{ Hz}, f_2 \in 4000 - 4100 \text{ Hz}, B = 0,03 \text{ mT}, \\ U_1 = U_2 = 16 \text{ V}, \alpha = 30^\circ, \beta = 60^\circ, \gamma = 45^\circ \end{aligned}$$

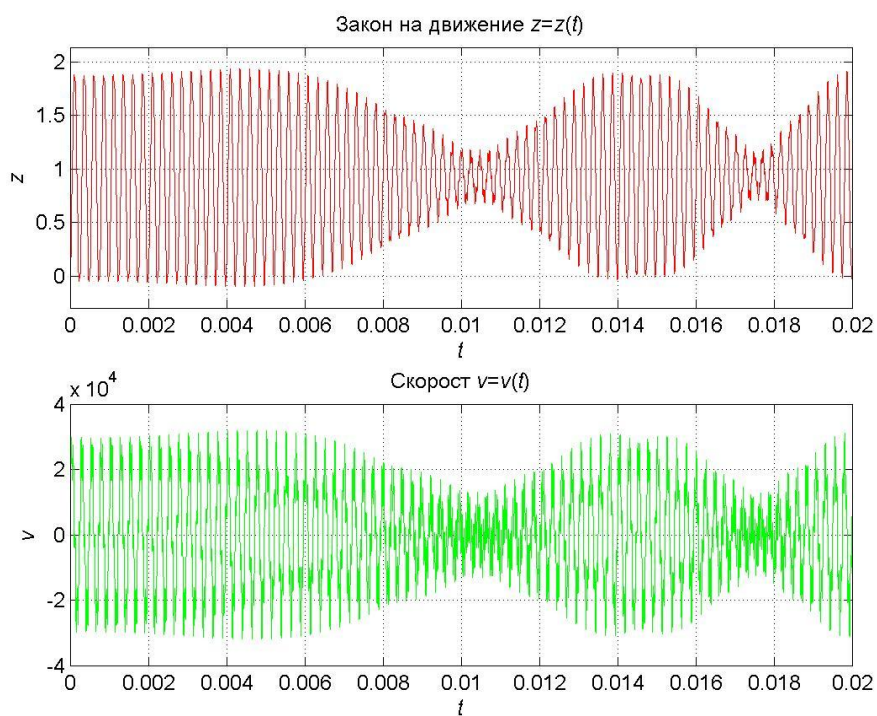


**Fig. 3a.** The movement and velocity of  $Na^+$  on X



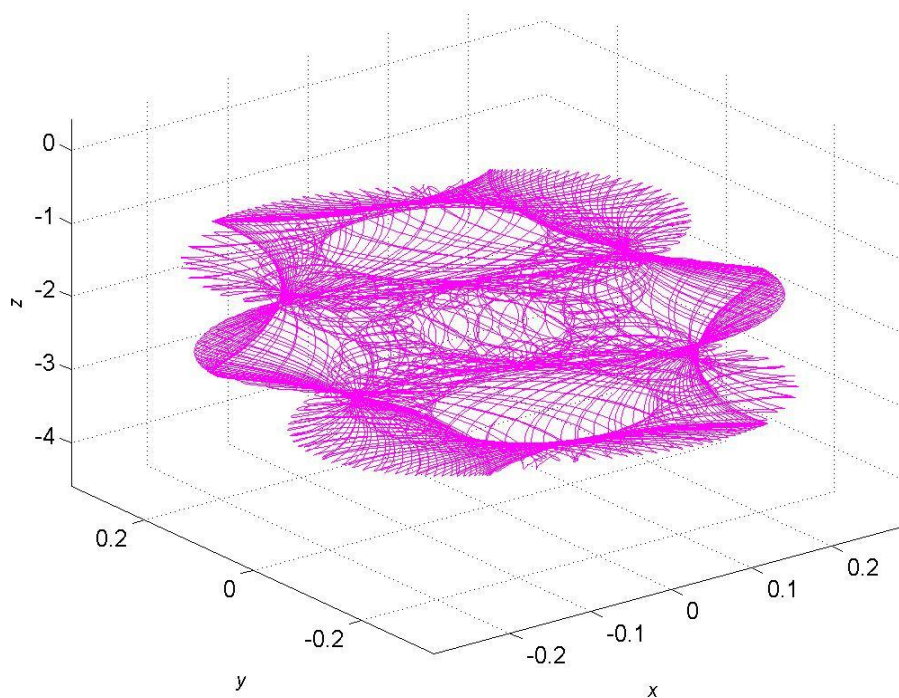


**Fig. 3b.** The movement and velocity of  $Na^+$  on Y



**Fig. 3c.** The movement and velocity of  $Na^+$  on Z

Траектория на заряда

Fig. 3d. The movement of  $Na^+$ 

### 3. Conclusion

The results of investigations, described in the paper are connected with new method for simultaneously application of permanent magnetic field and low frequency interferent currents.

### References

- [1]. <http://www.andrew.cmu.edu/use/sonen/survey/>
- [2]. David Meeker, Finite Element Method Magnetics Ver 3.1. Users Manual, 2001
- [3]. [www.qwed.com.pl](http://www.qwed.com.pl)
- [4]. <http://users.wpi.edu/~vadim/Projects/ISP-02-03>
- [5]. [www.vizimag.com](http://www.vizimag.com)
- [6]. [www.magneticasoft.com](http://www.magneticasoft.com)
- [7]. [www.integratedsoft.com](http://www.integratedsoft.com)
- [8]. [www.falstad.com/emwave2/directions.html](http://www.falstad.com/emwave2/directions.html)
- [9]. David Meeker, Finite Element Method Magnetics Ver 3.1. Users Manual, 2001
- [10]. Н. Тодоров, Магнитотерапия, Медицина и физкултура, София, 1990
- [11]. Hristov, V., Investigation of vehicular users' fairness in CDMA-HDR networks, Proceedings of the International Conference on Information Technologies (InfoTech-2007), September 21-23, 2007, Bulgaria vol. 2, pp.119-124
- [12]. Hristov, V., 1.1 Improving fairness for pedestrian users of CDMA-HDR networks, Proceedings of the International Conference on Information, Communication and Energy Systems and Technologies, June 24-27, 2007, Ohrid, Macedonia, vol. 2, pp.845-847.

# ROBOT CONTROL WITH CAMERA EYE

**Mathieu Grau**

*Ecole Supérieure d'ingénieurs en Electrotechnique et Electronique – Amiens, France*  
[mathieugrau@gmail.com](mailto:mathieugrau@gmail.com)

**Alexander Bekiarski, Pencho Venkov, Inna Nacheva**

*Technical University – Sofia, Bulgaria, St. Kliment Ohridski, 8*  
Tel.: +359 965 2674; E-mail: [aabbv@tu-sofia.bg](mailto:aabbv@tu-sofia.bg); Tel.: +359 965 3735; E-mail: [pven@tu-sofia.bg](mailto:pven@tu-sofia.bg) Tel.:  
+359 965 3735; E-mail: [i\\_nacheva@mail.bg](mailto:i_nacheva@mail.bg)

## Abstract

Visual robots are very popular in this moment, because of the technological innovations in the image sensors. There are many propositions of using image sensors to control the movements and reactions of a mobile robot. Such robots can see the space around, analyze the situations and make decisions for the right direction of movement. The visual robots equipped with image sensors became autonomous and are used in many practical cases as surveillance, services, toys etc. There are some other cases when it is necessary a person to control a visual robot. In such cases the possibilities are to make this control with some buttons or keyboard and transmit the control signals with wires or wireless to robot. The goal of this article is to control the robot from the human eyes movements, which are followed with a camera eye. It is chosen for experiments Lego Robot, equipped with a camera eye.

## 1. Introduction

The visual information can give to the robots very useful information for the real and current situation in the ob-

servation space, where the robot is placed and make the decisions for his movements [1]. This information can be processed and then send to the robot moving system to guaranty the right control the robot movements in the observed space [2]. This general goal can be divided to some problems, which can be solved first separate and then arranged in a sequence for right execution. The first problem is to input the visual information in robot system using a visual sensor. The second operation is to process this information for finding the eye as an object in the image information. Then it must to find the eye iris and to calculate camera eye coordinates. The next step is to transform the camera eye co-ordinates in the robot co-ordinate system. Finally it is necessary to interpret the robot coordinates as the specific robot commands for choosing right direction of robot movements. It is possible and necessary to add a communication system to link the mobile robot system with computer for distance control of the mobile robot. All of the mentioned steps are the goal and the parts of this article and are presented more clearly in the Figure 1 as the blocks of an algorithm.

## 2. Matlab program for visual information processing

### 2.1. Find and tracking the eye iris

Matlab simulation is made to examine the eye finding, iris of eye fixing, calculating the iris co-ordinates and eye movement track.

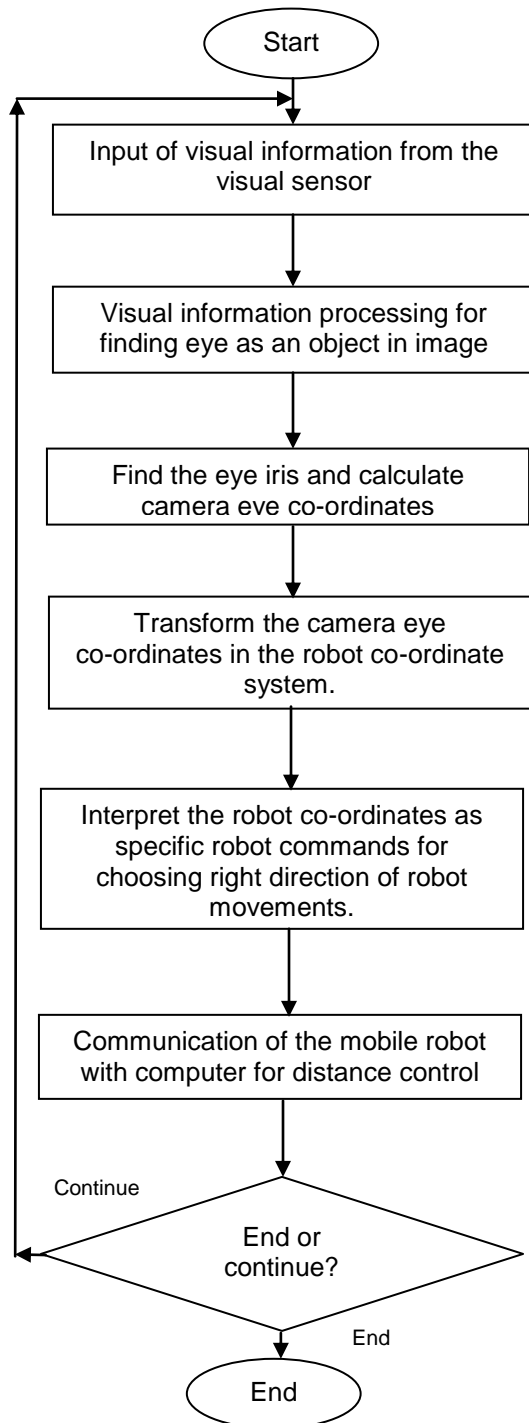


Figure 1. General view of algorithm

The image is input in real time or is stored and load in Matlab program as file in AVI format to use as test of visual information for human eye movements. The general view of the input image is shown in Figure 2.



Figure 2. General view of input image

For the simulation, the automatic eye find is substituted with a simplified manual specifying of the place of the eye, shown in Figure 3 and marked with crosses. The result of eye separating is shown in Figure 4. Then it is find the iris of the eye, determining their co-ordinates as a centre of gravity  $X_g, Y_g$ , thinking iris as a simple circle. In the calculation are used the common equation for the centre of gravity for the objects in an image:

$$X_g = \frac{\sum_{i=1}^n a_i * x_i}{\sum_{i=1}^n a_i} \quad (1)$$

$$Y_g = \frac{\sum_{i=1}^n a_i * y_i}{\sum_{i=1}^n a_i}, \quad (2)$$

Where

$X_g, Y_g$  are the co-ordinates of the eye iris;

$x_i, y_i$  – the current co-ordinates of image points;

$a_i$  – the values of current image point brightness.





**Figure 3.** Manual eye specifying



**Figure 4.** Result of eye separating

The result of iris eye fixing is shown in Figure 5 as crossing point of two lines.

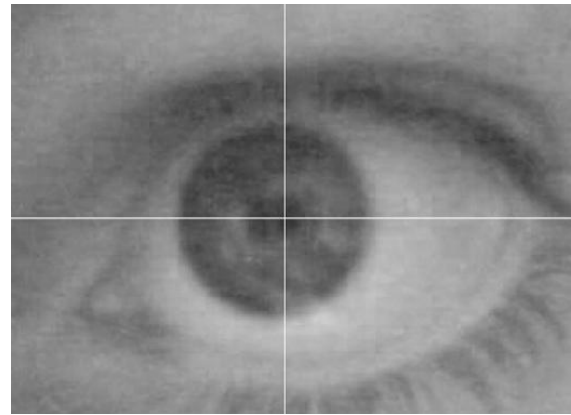


**Figure 5.** Result of eye iris co-ordinates calculation

The result of iris of eye fixing and find their co-ordinates is using for eye movements movement tracking with a suitable Matlab program. For a presentation of the eye movements tracking, in the Figure 6 is shown an appropriate trajectory for some little eye movement, dominantly in horizontal direction. This simulate the eye observation of some objects of interest in the space of human, to turn the attention of the visual moving robot in this direction.

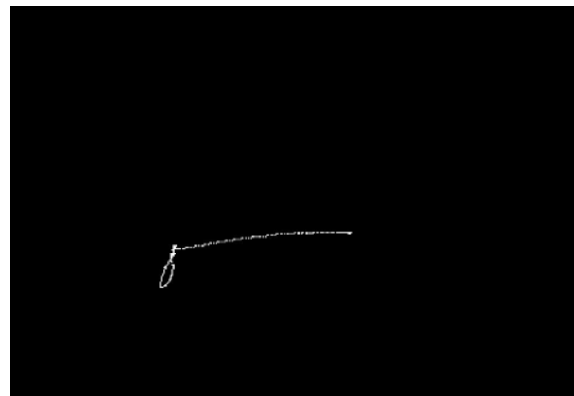


**Figure 6.** The trajectory of some little eye movements tracking

The information for eye iris movements as co-ordinates is transformed as robot co-ordinates and then as control commands to direct the robot movements in accordance to the human eye movements. A part of the program making this is shown in Figure 7.

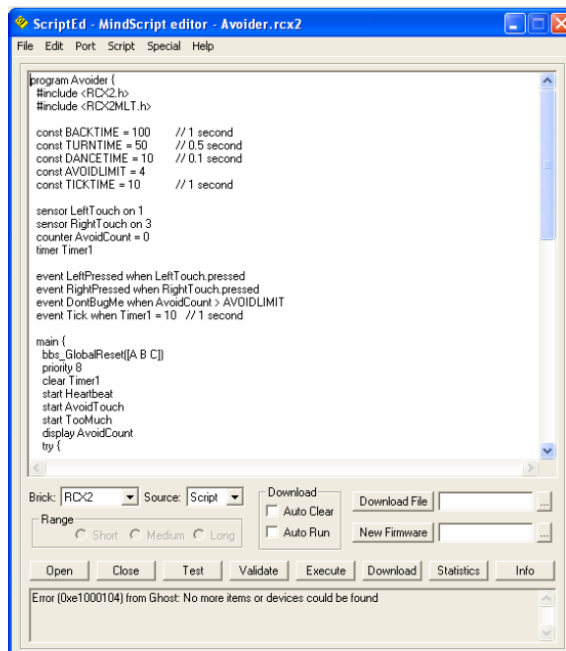


Figure 7. Robot control program

The steps of preparing and execution of the robot program are shown in Figure 8.

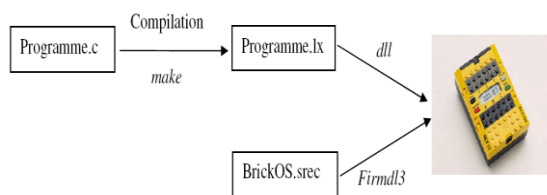


Figure 8. The steps of robot program preparation

Finally the working block algorithm of robot control with camera eye and the general view of the experimental visual robot system is presented in Figure 9 and Figure 10, respectively.

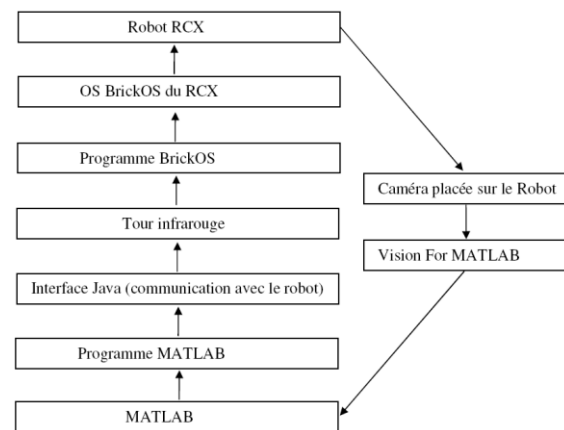


Figure 9. Workink algorithm of the robot program

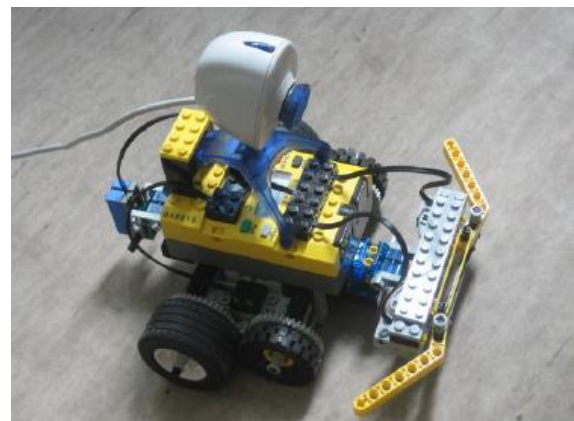


Figure 10. The general view of the robot system

### 3. Conclusion

A camera eye robot control system is proposed and present with some experimental results of its practical working. It is necessary to say, that this is only a little step for some more deeply following investigations in this direction.

### References

- [1]. M. Fujita, "Digital creatures for future entertainment robotics", IEEE Int. Conf. on Robotics ,2000.
- [2]. S. Mann, "Wearcam" in IEEE Int. Symp. of Wearable Computing, 1998.

# HIGH-RESOLUTION STEPPED FREQUENCY INVERSE SYNTHETIC APERTURE RADAR IMAGING USING TIME-FREQUENCY TRANSFORMS

A. Karakasiliotis<sup>(1)</sup>, G. Bouladakis<sup>(1)</sup>, A. Lazarov<sup>(2)</sup> and P. Frangos<sup>(1)</sup>

<sup>(1)</sup>*School of Electrical and Computer Engineering,  
National Technical University of Athens,  
9 Iroon Polytechniou Street, 15773 Zografou, Athens, Greece  
e-mail: anastasiskarak@yahoo.gr, geoboult@mail.ntua.gr, pfrangos@central.ntua.gr*  
<sup>(2)</sup>*Burgas Free University,  
62 San Stefano Street, Burgas, Bulgaria  
e-mail: lazarov@bfu.bg*

## Abstract

*In this paper, a two-dimensional (2-D) inverse synthetic aperture radar (ISAR) return signal model, recently proposed for the interesting case of illuminating a moving target with stepped frequency (SF) modulated pulses, is employed to describe the scattering response of simulated air-craft targets. Moreover, we propose an ISAR imaging approach that consists of a cross-correlation algorithm for range compression and a linear or bilinear time-frequency (TF) transform for azimuth compression.*

*The proposed approach circumvents the motion compensation necessity through averaging of all image frames. Additionally, simulation results, for signal-to-noise ratio (SNR) of 20dB and target orientation angle of 40°, indicate that the most efficient TF transformations result in clear ISAR images and outperform the classical FFT based azimuth compression.*

## Introduction

In this paper, a two-dimensional (2-D) inverse synthetic aperture radar (ISAR) return signal model, recently proposed for the case of stepped fre-

quency (SF) modulation [1], is exploited for realistic description of the scattering behaviour of the target to be imaged. Moreover, we propose an ISAR imaging approach that consists of a cross-correlation algorithm for range compression and a linear or bilinear time-frequency (TF) transform for azimuth compression.

The target to be imaged is represented by a rectangular grid of point scatterers, with the corresponding scattering intensities describing its geometrical shape. In contrast to the usual assumption in ISAR imaging, that of uniform rotational motion of the target around its mass-center, in this paper we assume that the target moves along a rectilinear trajectory at constant speed, without any rotational motion. Thus, the inverse synthetic aperture results from the translational motion of the target for a short period of time.

The cross-correlation based range compression technique [1] is applied to the synthetic 2-D raw data, which are generated via the employed 2-D SF ISAR return signal model. The resultant range profiles constitute the input data for the TF transform based azimuth compression technique. For each range cell, a time history series, with length equal to the number of SF bursts trans-

mitted during the coherent processing interval, is transformed to a range and instantaneous Doppler image. Furthermore, time sampling leads to a reduced number of image frames, adequate to describe the time-varying Doppler frequency shift of each point scatterer of the target of interest. The final step of the proposed ISAR imaging approach is the integration of the retained image frames, which results in a superresolution range-Doppler image.

Conventional linear TF transforms, such as the short-time Fourier transform (STFT), and, more sophisticated bilinear TF transforms, such as the pseudo Wigner-Ville distribution (PWVD) and its smoothed version (SPWVD), are used in the present study. Low cross-term interference is a desirable feature for the bilinear transforms, which usually exhibit better resolution in both time and frequency than the linear transforms. In this paper, we examine the image focusing efficiency of each transform.

As a means of assessing the validity of the proposed ISAR imaging approach, numerical simulations are carried out for a particular SF ISAR scenario causing unfocusing in case of FFT based image formation, and high-resolution ISAR images are generated for a simulated Mirage 2000 aircraft geometry. Based on the visual examination of the obtained ISAR images, we conclude that the proposed imaging methodology is very efficient for realistic ISAR scenarios.

This paper is organized as follows. In Section 2, we briefly describe the employed 2-D SF ISAR return signal model. Section 3 includes the mathematical description of the proposed ISAR imaging approach. Section 4 presents the simulation results for the examined ISAR scenario, and, the performance of the applied TF transformations is evaluated in terms of ISAR image resolution and cross-term interference reduction.

Finally, in Section 5, useful conclusions are drawn with respect to the present study.

## 2. 2-D ISAR Return Signal Model

It is a common practice to consider the target to be imaged as an assembly of point scatterers or distributed scattering centers [2], an approach which is widely adopted for high radar frequencies. In this paper, we adopt for simplicity a point scatterer model.

Furthermore, we model the 2-D ISAR geometry with the object and the ISAR being placed in separate coordinate systems. Details with respect to the geometrical modelling can be found in [1].

An analytical geometrical model of the time-domain ISAR return signal for the case of SF modulation has been recently proposed [1], and its validity has been proven for realistic ISAR scenarios. In the present study, we employ this model as an ideal characterization of the point scattering behaviour of the target to be imaged.

For the SF ISAR functionality, a series of bursts of SF pulses is emitted. Here, we assume that each burst consists of  $M$  pulses, to which SF modulation is applied. Moreover,  $N$  bursts are transmitted during the coherent processing interval.

The overall ISAR return signal is the sum of the deterministic data component  $S(p, m)$  and the random noise component  $n(p, m)$ , which is assumed to be white Gaussian. The following equations summarize the 2-D SF ISAR return signal model proposed and thoroughly described in [1].

$$S_n(p, m) = S(p, m) + n(p, m) \quad (1)$$

$$S(p, m) = \sum_{i=0}^{I-1} \sum_{j=0}^{J-1} \left\{ a_{ij} \cdot \text{rect} \left( \frac{t - t_{ij}(p)}{T_b} \right) \cdot \exp \left[ j 2\pi \cdot f_{m-r+1} \cdot (t - t_{ij}(p)) \right] \right\} \quad (2)$$



where

$a_{ij}$  denotes the scattering intensity for the  $ij^{\text{th}}$  point scatterer;

$t_{ij}(p) = \frac{2 \cdot R_{ij}(p)}{c}$  is the round-trip delay

of the ISAR signal backscattered from the  $ij^{\text{th}}$  point scatterer, for the  $p^{\text{th}}$  emitted burst;

$R_{ij}(p)$  denotes the magnitude of the distance vector from the ISAR to the  $ij^{\text{th}}$  point scatterer of the target;

$t = t_{ij\min}(p) + (m-1) \cdot T$  is the dwell time of the  $ij^{\text{th}}$  point scatterer;

$T$  and  $T_b$  stand for the pulse and burst repetition intervals respectively;

$f_{m-r+1} = f_0 + (m-r) \cdot \Delta f$  is the received pulse frequency, appropriately indexed in order to take into account the reception time offset of the ISAR signal reflected from the  $ij^{\text{th}}$  point scatterer, with respect to  $t_{ij\min}(p)$ ;

$\Delta f$  is the frequency step of the SF modulation.

In the above equations,  $p$  and  $m$  are the burst and sample indices respectively ( $p = \overline{1, N}$ ,  $m = \overline{1, M + L(p)}$ ,

$L(p) = \left\lceil \frac{t_{ij\max}(p) - t_{ij\min}(p)}{T} \right\rceil$ ), while indices  $i, j$  determine a particular point scatterer on the target grid, whose size is  $I \times J$ .

### 3. Proposed ISAR Imaging Approach

Range and azimuth compression are the fundamental procedures performed by a conventional radar receiver, in order to form a well-focused 2-D ISAR image.

#### 3.1. Cross-Correlation Based Range Compression

The cross-correlation based approach to range compression is realized by cross-correlating each burst of

the received raw data  $S_n(p, m)$  with a reference signal of the form  $s_{ref}(m) = \exp[j2\pi f_m(m-1)T]$ ,  $m = \overline{1, M}$ , i.e. a SF burst starting to be transmitted at  $t = 0$ . The result is one range profile for each received burst.

The cross-correlation based range compression is mathematically described by

$$\hat{S}(p, n_{ccl}) = \sum_{m=n_{ccl}}^{n_{ccl}+M-1} \left\{ S_n(p, m) \cdot \exp[-j2\pi f_{m-n_{ccl}+1}(m-n_{ccl})T] \right\} \quad (3)$$

where  $f_{m-n_{ccl}+1} = f_0 + (m-n_{ccl}) \cdot \Delta f$  and  $n_{ccl} = \overline{1, L_{\max} + 1}$  ( $L_{\max} = \max\{L(p)\}$ ) is the cross-correlation lag.

#### 3.2. Time-Frequency Transform Based Azimuth Compression

Our basic goal is the generation of a clear ISAR image of the moving target. In order to achieve this goal, a TF transform with superior resolution and low cross-term interference is needed. To apply the TF transform based image formation, we need a transform specially designed for computing time-varying spectrum and retrieving instantaneous Doppler frequency information. Having achieved a high-resolution time-varying Doppler spectrum, it is not necessary to flatten out the distribution of the radar frequency spectrum and to compensate for the individual motions of target's scatterers [3].

The range profiles, obtained by range compression of the received ISAR signal, constitute the input data for the TF transform based azimuth compression technique. For each range cell, a time history series, with length equal to the number of SF bursts, is transformed to a range and instantaneous Doppler image (image frame).

In our numerical experiments, an averaging of all image frames, produced from the TF transformation, is carried out to obtain a high-resolution ISAR (or range-Doppler) image.

### 3.2.1. Linear Transformation

One of the most known linear TF transforms is the Short Time Fourier Transform (STFT). STFT is based on the Fourier transform and its basic idea is the application of a moving time-domain window ( $w(t)$ ). Mathematically expressed

$$\text{STFT}(t, \omega) = \int s(t') w(t' - t) \exp(-j\omega t') dt' \quad (4)$$

In our simulations, a Hamming window is applied.

### 3.2.2. Bilinear Transformations

The most classical bilinear TF transform is the Wigner-Ville Distribution (WVD) [4]. In the WVD, the time-dependent autocorrelation function is given by the following equation.

$$\text{WVD}(t, \omega) = \int s(t + \frac{t'}{2}) s^*(t - \frac{t'}{2}) \cdot \exp\{-j\omega t'\} dt' \quad (5)$$

Even though the usefulness of the WVD for signal processing purposes has been well recognized for a rather long period, its applications are limited mainly due to the “cross-term interference” problem.

In order to reduce the problem of cross-term interference, a wide variety of bilinear TF transforms has been proposed in the literature [3]. Of particular importance is the Cohen's class of bilinear TF transforms [5]. The TF distributions, according to Cohen, can be written in a more generalized form, each using a different two-dimensional kernel function called the “parameterization function”.

A member of Cohen's class is the Pseudo Wigner-Ville Distribution (PWVD). Its mathematical definition is given in [6]

$$\text{PWVD}(t, \omega) = \int h(t') s(t + t'/2) s^*(t - t'/2) e^{-j\omega t'} dt' \quad (6)$$

It is obvious that the PWVD is a windowed version of WVD. The new pa-

rameter  $h(t')$  is a regular window, which typically results in frequency-domain smoothing of the WVD [6]. This means that the interference terms of the basic Wigner-Ville Distribution, because of their oscillatory nature, are attenuated in this new distribution. A Hamming time-domain window is used in our simulations.

By considering a separable smoothing function [6], we add a degree of freedom in the PWVD. This smoothing function is mathematically described by

$$\mathbf{H}(t, \omega) = \mathbf{g}(t) \mathbf{H}(-\omega) \quad (7)$$

where  $H(\omega)$  is the Fourier transform of a smoothing window  $h(t)$ . In this way, we allow for independent control of the smoothing applied on the WVD, in both time and frequency. This becomes obvious in the following distribution

$$\text{SPWVD}_s^{(g, H)}(t, \omega) = \iint_{t' \omega'} \mathbf{g}(t - t') \mathbf{H}(\omega - \omega') \cdot \mathbf{W}_s(t', \omega') dt' d\omega' \quad (8)$$

which is known as the Smoothed Pseudo Wigner-Ville distribution (SPWVD) [5]. The SPWVD allows the smoothing spreads,  $\Delta t$  and  $\Delta \omega$ , to be adjusted independently. This distribution is characterized by a separable smoothing kernel with two windows, whose effective lengths independently determine the time and frequency smoothing spread [5]. In our simulations, Hamming windows are used for time and frequency smoothing.

Furthermore, another important form of bilinear TF transformations is the Butterworth Distribution (BUD). Its parameterization function is defined as

$$\phi_{\text{BUD}}(\omega', t') = \frac{1}{1 + \left(\frac{\omega'}{\omega'_1}\right)^{2N} + \left(\frac{t'}{t'_1}\right)^{2M}} \quad (9)$$

$$(N, M, \omega'_1, t'_1 > 0)$$

It acts as a 2-D low-pass filter with a variably flat passband and narrow transition region. Thus, it results in simultaneous reduction of the cross terms and preservation of the auto-terms [8]. Butterworth distribution is defined as

$$BUD(t, \omega) = \frac{1}{2\pi} \int \left\{ \sum_{i=1}^N \alpha_i \left| \frac{t'}{t} \right|^{M/N} \exp[-\beta_i \left| \frac{t'}{t} \right|^{M/N} |t|] \cdot \cos(\omega_i \left| \frac{t'}{t} \right|^{M/N} |t| - \psi_i) \cdot s(u + \frac{t'}{2}) s^*(u - \frac{t'}{2}) \exp[-j\omega t'] du dt' \right\} \quad (10)$$

#### 4. Simulation Results

In our numerical experiments, we have simulated the 2-D SF ISAR scenario with the specific parameters included in Table 1.

For all TF transforms, except for the STFT, averaging of all generated image frames is carried out and the resultant ISAR images are presented below (Figs. 1-6). The middle image frame is shown for the STFT case (Fig. 2).

Notice that the image focusing efficiency is significantly increased for the PWVD, the SPWVD and the BUD, compared to the conventional FFT technique.

TABLE 1. 2-D SF ISAR Scenario

Simulation Parameter	Parameter Value
aircraft type	Mirage 2000C
aircraft length	15.5 [m]
aircraft wingspan	8.5 [m]
target grid cell dimensions $\Delta X = \Delta Y$	0.5 [m]
“reference” point coordinates $\{x_{00}(0), y_{00}(0)\}$	$\{0, 10\}$ [Km]
vector velocity magnitude $V$	300 [m/sec]
vector velocity angle $\alpha$	180 [°]

target orientation angle $\varphi$	40 [°]
initial carrier frequency $f_0$	10 [GHz]
square resolution $\Delta r_s = \Delta r_c$	0.5 [m]
radar bandwidth $B$	300 [MHz]
number of pulses $M$	64
frequency step $\Delta f$	4.6875 [MHz]
pulse repetition interval $T$	26.562 [µsec]
burst duration $T_b$	1.699 [msec]
number of bursts $N$	768

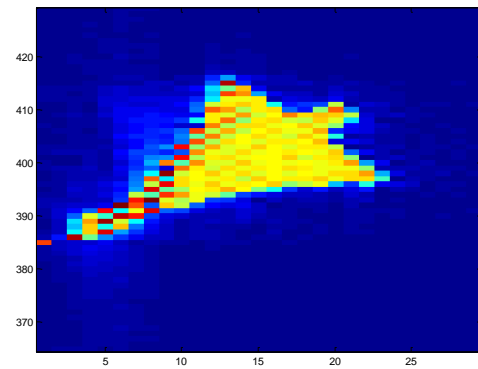


Figure 1. Reconstructed ISAR image via FFT based azimuth compression

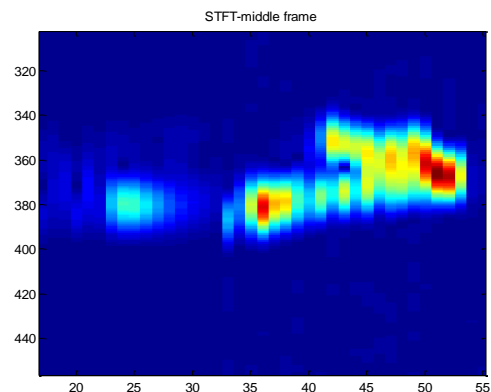
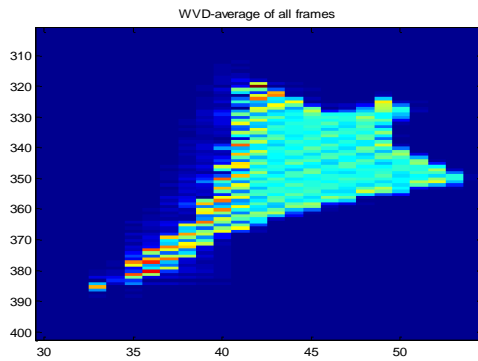
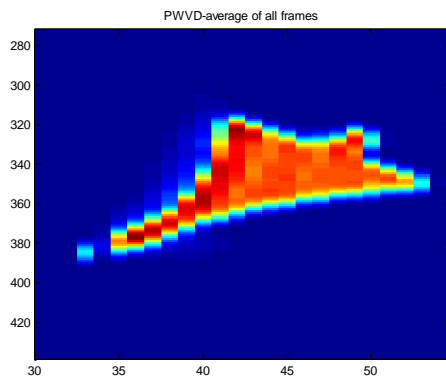


Figure 2. Reconstructed ISAR image via STFT based azimuth compression



**Figure 3.** Reconstructed ISAR image via WVD based azimuth compression



**Figure 4.** Reconstructed ISAR image via PWVD based azimuth compression

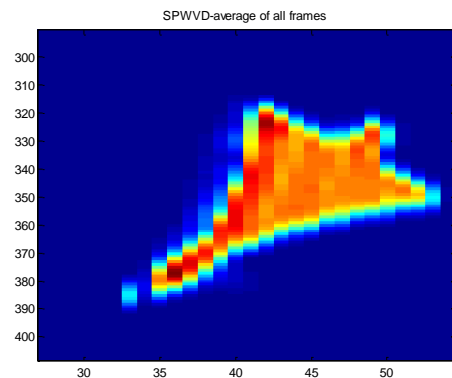


**Figure 5.** Reconstructed ISAR image via SPWVD based azimuth compression

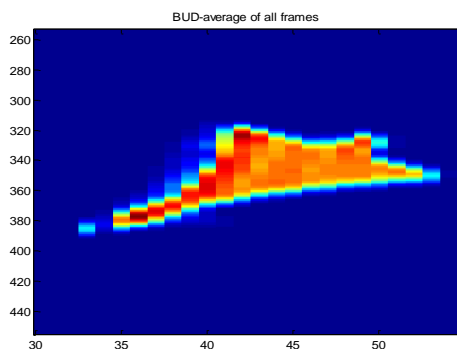


**Figure 6.** Reconstructed ISAR image via BUD based azimuth compression

## 5. Conclusions

In this paper, we have applied several TF transforms for realistic ISAR imaging. Bilinear transforms result in quite clear images, while circumventing the motion compensation necessity. For the simulated ISAR scenario, PWVD, SPWVD and BUD transformations have outperformed the classical FFT based azimuth compression.

## Acknowledgment

The authors thank Prof. Anton Lazarov, for the fruitful discussions on ISAR imaging and the common research activity.

## References

- [1] A. Karakasiliotis, A. Lazarov, and P. Frangos, "Two-dimensional ISAR Model and Image Reconstruction with Stepped Frequency Modulated Signal," *submitted to IET Signal Proc.*, July 2007.
- [2] M. Gerry, L. Potter, I. Gupta, and A. van der Merwe, "A Parametric Model for Synthetic Aperture Radar Measurements," *IEEE Trans. Antennas Propag.*, July 1999, Vol. 47, no. 7, pp. 1179-1188.
- [3] V. Chen, and H. Ling, *Time-Frequency Transforms for Radar Imaging and Signal Analysis*, Artech House, Boston-London, 2002.
- [4] S. Qian, and D. Chen, "Decomposition of the Wigner-Ville Distribution and Time-Frequency Distribution Series," *IEEE Trans. Signal Proc.* Oct. 1994, Vol. 42, no. 10, pp. 2836-2842.
- [5] F. Hlawatsch, and G. F. Boudreaux-Bartels, "Linear and Quadratic Time-Frequency Signal Representations," *IEEE Signal Proc. Mag.*, Apr. 1992, pp. 21-67.
- [6] F. Auger, P. Flandrin, P. Goncalves, and O. Lemoine, "Time-Frequency Toolbox for Use with MATLAB (tutorial)," July 1997.
- [7] H. Choi, and W. Williams, "Improved Time-Frequency Representation of Multi-component Signals using Exponential Kernels," *IEEE Trans. Acoust. Speech and Signal Proc.*, June 1989, Vol. 37, no. 6, pp. 862-871.
- [8] A. Papandreou, and G. F. Boudreaux-Bartels, "Generalization of the Choi-Williams Distribution and the Butterworth Distribution for Time-Frequency Analysis," *IEEE Trans. Signal Proc.*, Jan. 1993, Vol. 41, no. 1, pp. 463-472.

# ULTRASONIC GENERATOR-TRANSDUCER COMBINED PERFORMANCE ENHANCEMENT

L. Svilainis, V. Dumbrava, G. Motiejunas

Signal processing department, Kaunas University of Technology

Studentu str. 50, LT-51368 Kaunas, Lithuania

T, +370 37 300532; F, +370 37 753998; E, linas.svilainis@ktu.lt / vytautas.dumbrava@ktu.lt / giedrius@selteka.balt.net.

## Abstract

*The methods to improve the generator power transmission to ultrasonic transducer performance enhancement are analyzed. This is important in portable equipment. Performance is analyzed using the transducer mathematical model, obtained from complex impedance measurement results as the frequency-dependent response. The matching circuits are analyzed as well as the transformer matching case. The matching circuitry type influence has been evaluated. The performance is analyzed by P-SPICE simulation. Various secondary parameters related to voltage step-up and available bandwidth have been calculated. The presented configuration can be used for ultrasonic transducer excitation using an arbitrary waveform generator output stage which is important in nonlinear medical ultrasound studies.*

## 1. Introduction

In the power ultrasound applications such as the medical therapy, nonlinear ultrasound and resonant technique used in nondestructive testing (NDT), the equipment performance is defined by the transducer matching. In such applications the power delivery to the load is of primary importance. The performance of high resolution techniques

is also dependant of matching. But here the transducer time response and bandwidth are most important.

The electronic circuits, filters and inter-stages design usually aims to match out the load to a resistive generator, which maybe the Thevenin equivalent of some other network, so that the transfer of power from the source to the load is maximized over a given frequency band of interest. Variety of publications dedicated to this problem can be found [1-3].

The goal of this paper is to analyze the several standard methods of ultrasonic transducer matching to excitation electronics using various performance evaluation criteria.

## 2. Transduction model

In order to evaluate the whole system performance, transducer, excitation electronics and matching circuits' models are included. Power delivery from generator to media is analysed. Simplified model structure is presented in Figure 1.

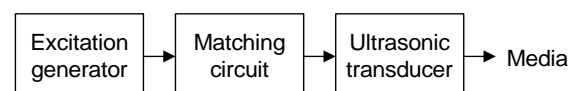


Figure 1. Transduction model

For model to be accomplished excitation electronics, transducer and ma-

tching stages have to be simplified to some extent and be presented as electronic equivalent model.

## 2.1. Ultrasonic transducer

Most of the ultrasonic transducer modeling techniques are based on the theoretical models. The Mason [4], Redwood [5], KLM [6] and other require the knowledge of the transducer's material properties and physical dimensions. Near the main resonant frequency piezoelectric ultrasonic transducer can be replaced by more simple equivalent circuit, described as *Butterworth-Van Dyke* (BVD) model [1]. (Figure 1).

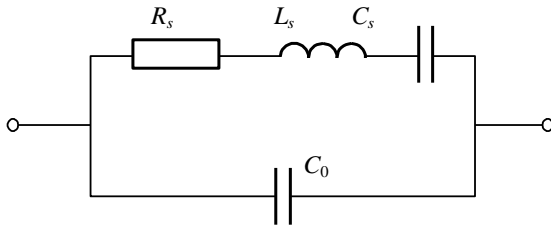


Figure 2. BVD model of transducer

We consider BVD as the best lumped parameter equivalent circuit suitable for our purpose since they are fitting typical piezoelectric converter impedance and are able to represent the transduction. The capacitance of the piezoelectric material is represented by  $C_0$ . The mechanical system is described by a series resonant circuit  $L_s$ ,  $C_s$ ,  $R_s$ . Changes in the mechanical boundary conditions are modeled by alteration of  $R_s$ , and  $C_s$ , while changes of inductance  $L_s$  describe the mass of the mechanical system. The  $R_s$ , can be split [2]:

$$R_s = R_0 + R_{xm}, \quad (1)$$

where  $R_0$  is the part representing the losses in piezo-ceramic material and  $R_{xm}$ - acoustic transmission into media. Since  $R_{xm}$  is the largest part, the power

supplied to  $R_s$  can be considered as the acoustic emission.

The impedance  $Z_T$  of the ultrasonic transducer then can be expressed as:

$$Z_T = \frac{\left( R_s + j\omega L_s + \frac{1}{j\omega C_s} \right) \cdot \frac{1}{j\omega C_0}}{R_s + j\omega L_s + \frac{1}{j\omega C_s} + \frac{1}{j\omega C_0}}. \quad (2)$$

System for ultrasonic transducer impedance measurement [7] was used to obtain the complex transducer impedance. Then impedance was approximated by BVD model. Results are presented in Figure 3.

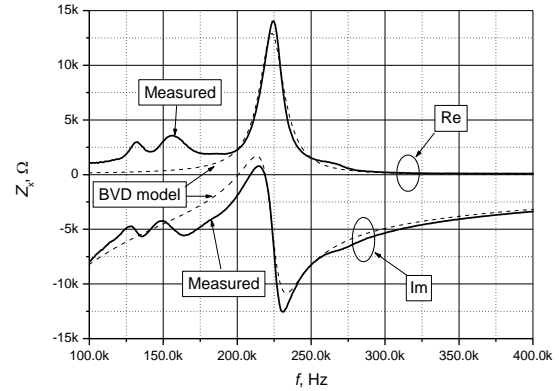


Figure 3. Measured impedance approximation by BVD model

The parameters of BVD model obtained by least mean square fitting to measured impedance are presented in Table 1.

Table 1. Transducer parameters

$R_s, \Omega$	$C_s, \text{pF}$	$L_s, \text{mH}$	$C_0, \text{pF}$
5333	21.3	29.8	77.1

From Figure 3 it can be seen that transducer exhibit serial and parallel resonance:

$$\omega_s = \frac{1}{\sqrt{L_s C_s}}, \quad \omega_p = \frac{1}{\sqrt{L_s \frac{C_s C_0}{C_s + C_0}}}. \quad (3)$$

The series resonance frequency of such mechanical system is the optimal point of operation, because the oscillation magnitude is reaching its maximum value. At this complex impedance of  $L_s$ ,  $C_s$  series connection is zero and equivalent transducer circuit is simplified to parallel connection of  $R_s$  and  $C_0$ .

## 2.2. Matching circuits

In general two approaches can be used for matching [8-11]:

- LC circuit(s)
- RF transformer

LC circuit is used to neutralize the imaginary part of ultrasonic transducer input impedance and (or) to transform the impedance.

In LC resonant implementation, as indicated in [1] the additional inductor should resonate with clamping capacitor  $C_0$  in order to remove it from the circuit (Figure 4).

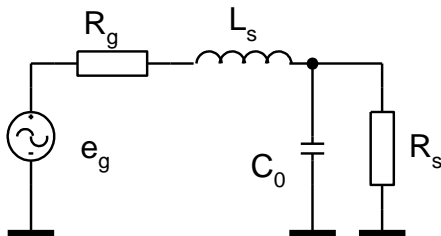


Figure 4. LC resonant matching

Serial  $L_s$  or parallel  $L_p$  inductance value then is calculated as:

$$L_s = L_p = \frac{1}{(\omega_s)^2 C_0}. \quad (4)$$

In [1] It was indicated that decision when to use additional inductance in series or in parallel can be arrived by solving the transfer coefficient. For serial case it is:

$$K_s = \frac{\rho/R_g}{1 + R_s/R_g}, \quad (5)$$

and for parallel case:

$$K_p = \frac{1}{1 + R_s \cdot R_g / \rho^2}, \quad (6)$$

were  $\rho$  is characteristic impedance of resulting resonant tank. From (5) and (6) it is seen that  $K_s > K_p$ , when  $\rho > R_g$  and  $K_s < K_p$ , when  $\rho < R_g$ . For  $\rho = R_g$  case both solutions are equivalent.

The LC resonant circuit has highest sensitivity when operating close to mechanical resonance. High sensitivity of LC resonant circuit is serious disadvantage [2] since output filter is suitable only for particular transducer. Due transducer heating, aging and loading mechanical resonance is changed. In order to account for these effects  $L_s$  is chosen to resonate slightly below unloaded transducer resonance.

The LLCC resonant implementation (Figure 5) is similar: resonant frequency is chosen close to the mechanical resonance of ultrasonic transducer.

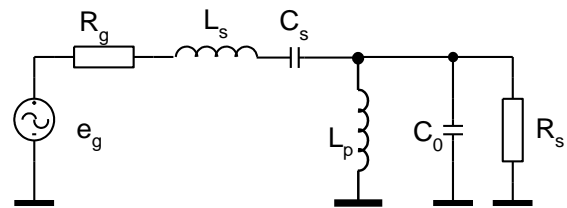


Figure 5. LLCC resonant matching

Equation (4) is used for  $L_s$  and  $L_p$  calculation and  $C_s$  is chosen equal  $C_0$ . In practical operation filter will be detuned, source [2] explains how to control the peaks position.

The "L" matching [12] is implemented using by placing two reactive components between amplifier and the transducer (Figure 6).

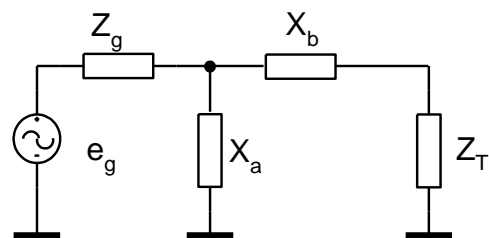


Figure 6. "L" matching structure

First, transducer impedance at mechanical resonance is converted to serial form:

$$R_T = \frac{R_s}{1 + (R_s \omega_s C_0)^2},$$

$$X_T = \frac{R_s^2}{\omega_s C_0 [1 + (R_s \omega_s C_0)^2]}. \quad (7)$$

Then, corresponding reactance are:

$$X_a = -\frac{R_g^2 + X_g^2}{Q R_g + X_g},$$

$$X_b = Q R_T - X_T, \quad (8)$$

where

$$Q = \pm \sqrt{\left( \frac{R_g}{R_T} \left[ 1 + \left( \frac{X_g}{R_g} \right)^2 \right] - 1 \right)}. \quad (9)$$

Taking both Q solutions and swapping source and load positions four configurations are available.

RF transformer [11,13] is mainly used for impedance transformation therefore capacitive part of the load should be compensated using additional LC circuits. The magnetizing transformer [13] inductance  $L_m$  is defining the lowest applicable frequency. In general  $L_m$  is chosen that reactance at mechanical resonance is ten times larger the source impedance:

$$L_m = \frac{10 R_g}{\omega_s}. \quad (10)$$

Transformer turns ratio is set:

$$n = \sqrt{\frac{R_s}{R_g}}. \quad (11)$$

### 2.3. Excitation electronics

Beside the transducer, also the excitation electronics play an important role in the system performance [14,15].

The application of the transformer as impedance matching element allows considering the push-pull B class amplifier as amplifier output stage [14] (Figure 7).

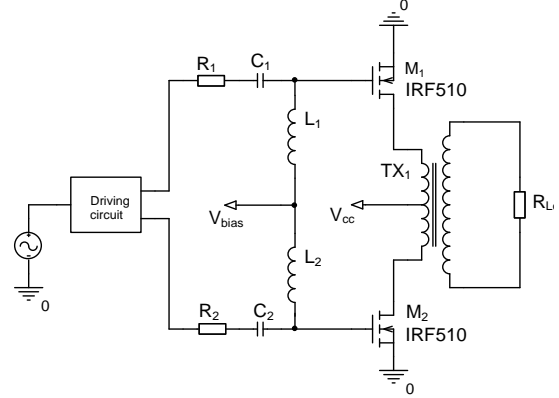


Figure 7. Push-pull output amplifier

In such setup active elements are operated at collector/drain voltages of twice the supply voltage. But the symmetrical power delivery and the ability to use same carrier type transistors make it attractive in ultrasonic transducer excitation. Therefore we will favor this topology over single-sided drive [15] or purely active amplifier stage [11].

### 3. Modeling results

The ultrasonic transducer and excitation generator combined performance have been studied. Assuming that low output impedance generator is matched to high input impedance load, introduction of the matching circuit should cause the voltage step-up. The voltage set-up ratio is proportional to impedances:

$$k_{up} = \frac{|Z_T|}{\sqrt{R_g R_s}}. \quad (12)$$

Modeling has assumed that excitation generator has pure active output impedance of  $R_g=50 \Omega$  and transducer has parameters listed in the Table 1. Modeling results for transducer clamps voltage  $U_T$  for matching circuits mentioned above are presented in Figure 8.



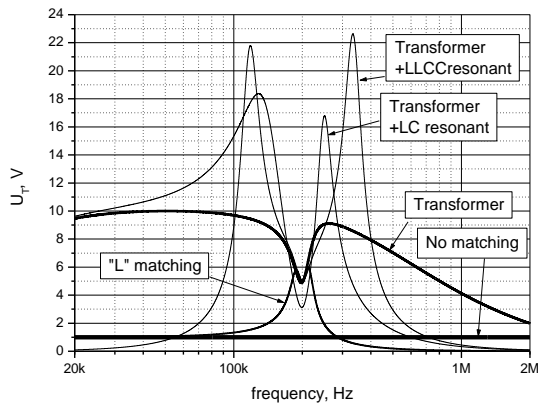


Figure 8. Transducer voltage  $U_T$

Analysis of results presented indicates that almost all matching circuits have similar voltage step-up ratio at mechanical resonance. The only difference is the voltage behavior beyond the resonance frequency. Table 2 carries the voltage step-up ratios obtained for various matching conditions.

Table 2. Voltage step-up at resonance

Matching circuit	Step-up
No matching	0.99
Transformer	4.9
Transformer + LC rez	3.1
Transformer + LLCC rez	5
"L" matching	5

Notable that for unmatched case the voltage on transducer clamps is not changing over frequency. Since power the matching goal is the maximum acoustic emission, it is interesting to analyze the voltage on acoustic emission representing resistor  $R_s$ . Graphs on Figure 9 are demonstrating the voltage  $U_{R_s}$  for various matching conditions.

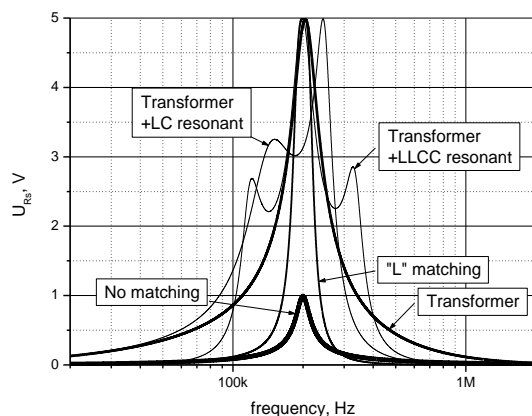


Figure 9. Emission representative  $U_{R_s}$

Again, all the matching circuits produce similar voltage on emission resistor. Only one peak is aside main (Transformer+LC resonant) resonance. This circuit is deliberately detuned as recommended in [2]. Notable, that behavior over frequency range is different for all matching circuits. Therefore power on  $R_s$  was calculated and normalized to its peak. Results of normalized emission power are presented in Figure 10. After normalization it was expressed in dB.

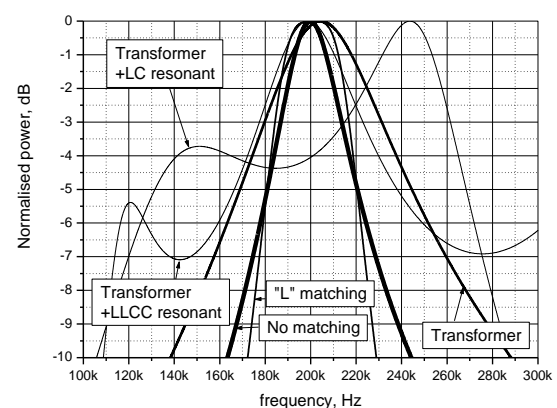


Figure 10. Normalised power on  $R_s$

Using results on Figure 10 the -3dB bandwidth was calculated for various matching configurations. Results are presented in Table 3, column labelled B to indicate the bandwidth in kHz.

Table 3. Bandwidth and energy of  $R_s$

Matching circuit	B, kHz	E, J
No matching	27.2	8.24
Transformer	51.9	370
Transformer + LC rez	46.6	421
Transformer + LLCC rez	45.7	462
"L" matching	32.8	180

It can be seen that transformer introduction in matching circuits has improved bandwidth response. But it is interesting to combine both bandwidth performance and the voltage step-up. Therefore integral of power on  $R_s$  was taken over whole frequency band. The generator voltage was unity. The result can be treated as energy which can be delivered to media (Table 3, row "E").

## 4. Conclusions

Investigation carried out indicates that if the matching at single frequency is needed then all matching circuits perform the same. But if bandwidth is under consideration transformer introduction allows for significant bandwidth increase. If both the power delivered and the available bandwidth is important then transformer and resonant LC or LLCC matching circuits should be considered.

## Acknowledgments

Authors would like to thank Prof. B. Dekeris for support of presentation of this work.

## References

- [1]. V. Domarkas, R. Kazys, "Piezoelectric transducers for measuring devices", Mintis, Vilnius, 1975, p.255.
- [2]. C.Kauczor, N.Frohleke, "Inverter Topologies for Ultrasonic Piezoelectric Transducers with High Mechanical Q-Factor" 35th Annual IEEE Power Electronics Specialist Conference, 2004, pp.2736-2741.
- [3]. L.Capineri, L.Masotti, M.Rinieri, S.Rocchi, "Ultrasonic Transducer as a Black-Box: Equivalent Circuit Synthesis and Matching Network Design", IEEE Transactions on ultrasonics, ferroelectrics and frequency control, Vol. 40, No. 6, 1993, pp.694-703.
- [4]. W.P.Mason, "Electromechanical Transducers and Wave Filters", Princeton, NJ, Van Nostrand, 1948
- [5]. M.Redwood, "Transient Performance of a Piezoelectric Transducer", JASA, 33, 1961, pp.527-536,
- [6]. R.Krimholtz, D.Leedom, G.Matthaei, "New Equivalent Circuit for Elementary Piezoelectric Transducers", Electron Letters, Electron. Lett. 6, pp. 398-399,1970
- [7]. L.Svilainis,V.Dumbrava," Measurement of complex impedance of ultrasonic transducers", Ultragarsas, 2007, No.1(62), pp. 26-29.
- [8]. "Notes On The Design Of Matching Systems For Piezo Elements" Application Note Airmar Technology Corporation, 2005, p.4.
- [9]. L.Besser, "Practical RF circuit design for modern wireless systems: Passive circuits and systems", Norwood, USA, Artech House, 2003, p.529.
- [10]. R.W. Brounley "Matching Networks for Power Amplifiers Operating into High VSWR Loads", High Frequency Electronics, 2004, pp.58-62.
- [11]. L. Svilainis, V. Dumbrava "The RF transformer application for ultrasound excitation: the initial study" Ultragarsas, 58, Kaunas, 2006, pp.25-29.
- [12]. G.Petersen, "L-Matching the Output of a RITEC Gated Amplifier to an Arbitrary Load", RITEC Inc., USA, p.8
- [13]. Ch.Trask, "Designing wide-band Transformers for HF and VHF Power Amplifiers", QEX/Communications Quarterly,2, 2005, pp.3-15.
- [14]. L.Svilainis, G.Motiejunas, "Power amplifier for ultrasonic transducer excitation", Ultragarsas, Kaunas, 2006, No.1(58),pp.30-36.
- [15]. J.A. Brown, G.R. Lockwood, "A Low-Cost, High-Performance Pulse Generator for Ultrasound Imaging", IEEE transactions on ultrasonics ferroelectrics and frequency
- [16]. control, Vol 49, No 6, 2002, pp. 848-851.

# SOFTWARE CONSIDERATIONS FOR ULTRASONIC DATA COLLECTION AND EVALUATION SYSTEMS

L. Svilainis, L. Sinkunas

Signal processing department, Kaunas University of Technology  
Studentu str. 50, LT-51368 Kaunas, Lithuania  
T, +370 37 300532; F, +370 37 753998; E, linas.svilainis@ktu.lt / linas.sinkunas@delfi.lt.

## Abstract

*The ultrasonic data acquisition and analysis system software concept is analyzed. Modular software configuration is suggested. It should be capable to adapt to new hardware configurations. The core-based structure is suggested. External units planned are: acquisition, imaging, processing, analysis and tools. Acquisition unit is for hardware control, data exchange and communication. Structure is controlled by separate software and core is only using the defined DLL module. Imaging unit is responsible for visualization of data as line plot A-scan, color coded, mesh, surface or contour plot of B- or C-scan, volume rendering. Graphic user interface (GUI) is planned to be two-fold. One part of GUI resides in core such as menu, toolbars, views, controls and status bar management. Remaining parts of GUI are coming together with external units. Only essential for the current state controls are displayed so user is not disrupted by variety of buttons and whiskers.*

## 1. Introduction

Nowadays many applications are using ultrasound. It can be used in technical diagnostics, navigation, security, or in medical diagnostics and treatment.

Large variety of measurement devices are created for this purpose. How-

ever, market is missing not expensive, portable, yet sufficiently functional and flexible ultrasonic measurement system dedicated for scientific research. Such system should be configurable and with possibility to extend and adapt to different scientific or commercial applications.

Hardware of such system is already under development [1]. This hardware will need the modern software. The aim of this publication is to analyze the modern design techniques and concepts of software dedicated for data acquisition and processing. The software considerations for ultrasonic data collection and evaluation system should be rectified.

## 2. Software architecture

Currently existing commercial frameworks with image processing and visualization capabilities [2] include Amira, Analyze, AVS[3], IDL[4], IRIS Explorer, Matlab [5]. Commercial versions of VolView [6], and MeVisLab [7] are also available. But commercially available frameworks are expensive and not suitable for budget application that we target. In this case we consider that would be the best to use popular freeware open source libraries or frameworks [2,9,10]. It can be MITK, VolView, MeVisLab or SCIRun [2]. MITK is oriented for end-user applications with fixed algorithm configurations. VolView

is the best for non-repetitive end-user applications based on existing functionality. MeVisLab and SCIRun are the best for creating applications prototypes using visual data-flow programming.

However all of them can not satisfy our needs because they have already defined user interface and limited number of algorithms and functionality. Therefore decision was taken to write our framework on the base of ITK and VTK libraries using the C++ language as glue and QT library for GUI (graphical user interface). Suggested tools hierarchy is in Figure 1.

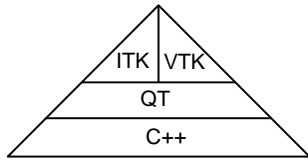


Figure 1. Tools hierarchy

The justification for such decision is:

- libraries are open source therefore are wanted for budget applications;
- they are multiplatform, permanently under development and already popular in academic community so the availability of solutions similar to ours is high.

The software architecture structure is presented in Figure 2.

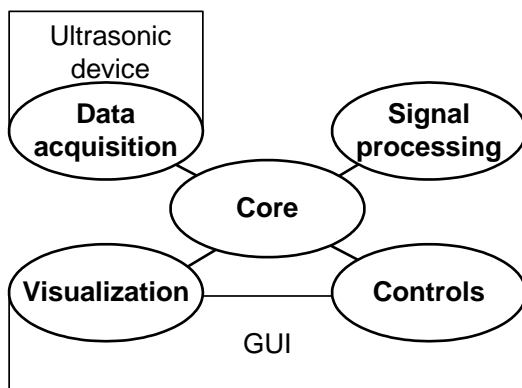


Figure 2. System architecture

The top agent in PAC hierarchy is Core that is mostly responsible for organizing connections and data exchange between different agents. The sub-

agents can be distributed into several groups: Data acquisition (DA), Signal processing (SP), Visualization (Vi) and Controls (Ctrl).

## 2.1. Core agent

Core is responsible of control of underlying agents and their interaction. This agent also builds GUI screens and widgets into composition. The whole hierarchy of the application is composed according to Presentation – Abstraction – Controller design pattern where each agent of the hierarchy is responsible for certain functionality of the system and is implemented according to Model –View - Controller pattern. All the units are derived from base unit class single for every agent.

## 2.2. Data acquisition agent

This agent is responsible for data acquisition from ultrasonic device. The structure ultrasonic device is shown in Figure 3 [11].

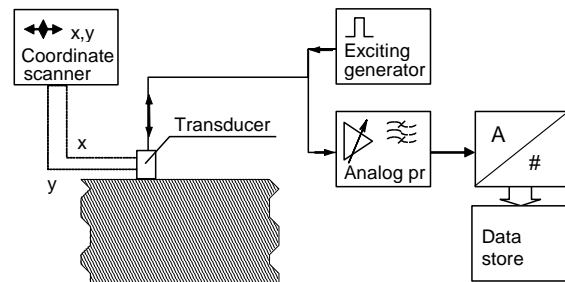
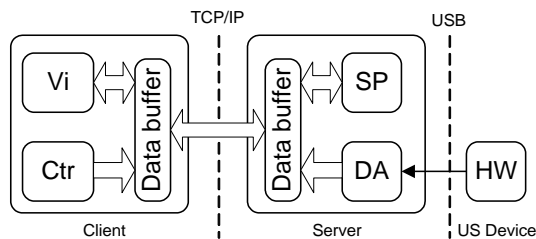


Figure 3. Hardware structure

The connection with external hardware is accomplished via USB interface, but the possibility to use other data collection and control interfaces as well as other USB device types is foreseen. For this purpose software acquisition agent must be derived from base data acquisition agent class. Hardware structure is described and DA agent structure is controlled by separate software and Core is only using the defined DLL module.

During acquisition process DA agent work as separate thread in parallel with other threads. All the data obtained for the hardware is stored in agent's data buffer. We suggest using client – server computing architecture which separates a client from a server. Suggested structure of workflow is presented in Fig. 4.



**Figure 4.** Workflow structure

The data acquisition and signal processing agents are located on server side. The server always takes data from data acquisition device, makes signal processing and sends to client by request.

The visualization and controls agents can be located at client side. The Core agent resides both on client side and on application side since it is responsible for task synchronization and GUI which interacts with user.

Such workflow structure allows to be realized in simple way, when server and client are in one single process. Still they work as separate threads but use common memory. Workflow can be made more complex, when server and client threads are working as separate processes on different computers. Then number of servers can be increased, allowing for multiple data source management (Figure 5).

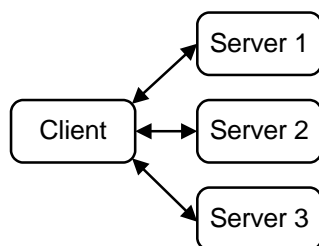


**Figure 5.** Multisource manager

The communication can be done by using TCP/IP connection increasing the remote capabilities of the system.

### 2.3. Signal processing agent

Signal processing agent is responsible for signal processing. Notable that thanks to template based data interface signals supplied for the same processing routine can be 1D, 2D 3D-dimensional. It can be used as standalone processing unit with individual data input and output nodes and parameters node. Or, single SP units can be combined to create more complicated processing branches (Figure 6).

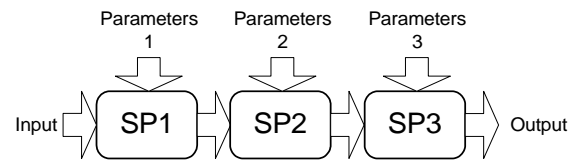


**Figure 6.** Chaining of signal processing units by forced execution

Every unit has one or more inputs and outputs and one or several parameter inputs. Several units can be combined into serial or split branch. Every unit has its own GUI for parameters and can be stored in separate DLL file. Same is applicable for all agents.

The execution of split branches is complicated. By default it is processed forward. But execution on request principle can be applied. Such approach is extremely useful if algorithm has a lot of branches and is time time-consuming. Then unit should be made of two parts: processing and run manager (Figure 7).

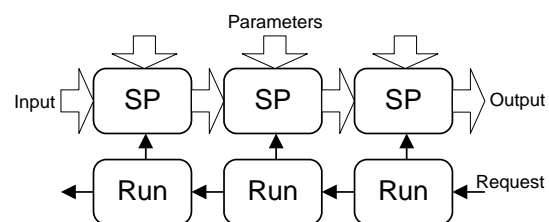


**Figure 7.** Signal processing unit chain with requested execution

Chained units can pass the processing request up to the desired branch, so whole tree update is not necessary. Here we present the example from the ITK library:

```
filter2->SetInput( filter1->GetOutput() )
filter3-> SetInput( filter2->GetOutput() )
filter3-> Update()
```

Predicted units for SP agent:

- FFT
- Filters;
- Arithmetic operations;
- Morphological operations;
- Cross-correlation processing;
- Radon transformation;
- Segmentation (thresholding);
- Averaging (moving average);
- Wavelet processing;
- Color coding;
- Detector (peak, min, max);
- Geometry measurement.

## 2.4. Visualization agent

Visualization agent is responsible for data imaging. Since data can be of different dimensionality, it is necessary to have the corresponding imaging possibilities. The most popular imaging modes are presented in Figure 8.

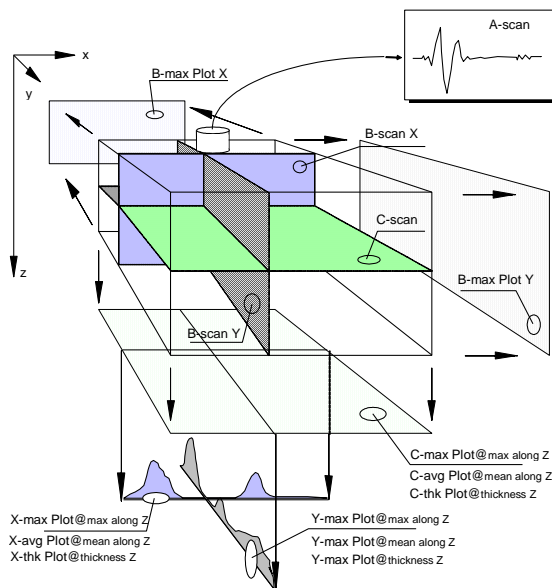


**Figure 8.** Possible imaging modes

In general visualization can be grouped in 1D, 2D and 3D modes. The 1D imaging example is an A-scan (Figure 9).

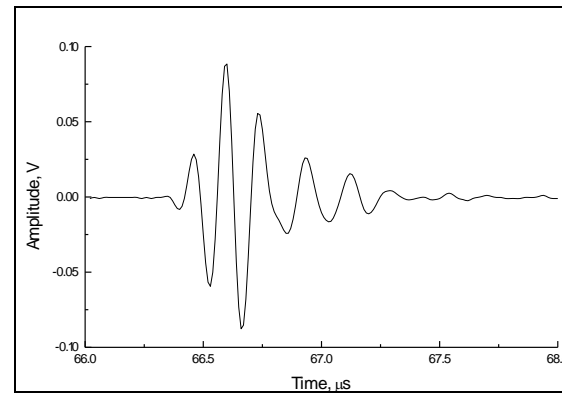


**Figure 9.** Line plot of received signal (A-scan)

The two most popular 2D imaging modes are B-scan (Figure 10) and C-scan (Figure 11).

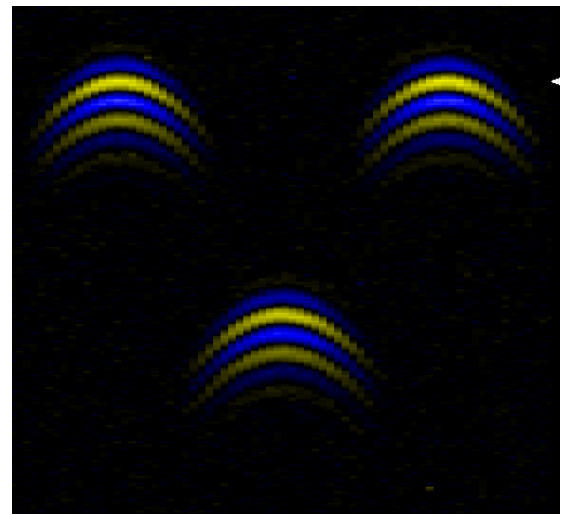


**Figure 10.** B-scan of 3 reflectors

Another subdivision of 2D images can be grouped into:

- color coded;
- grey scale;
- mesh;
- surface lighting;
- contour plot;
- or can be a combination of mentioned above.

In general 2D images can be obtained also from other sources such as line scan or matrix optical cameras, X-

ray devices. Software should be capable of multiple data source data fusion both coordinate and imaging sense.

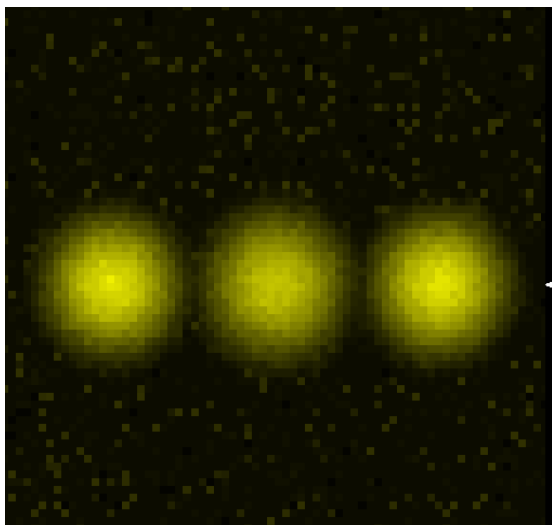


**Figure 11.** C-scan of 3 reflectors

The most attractive imaging mode is 3D (Figure 12 [12]).

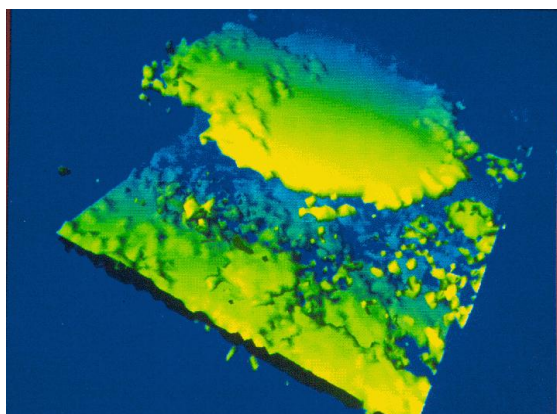


**Figure 12.** 3D-scan

3D scan is volume visualization and needs more processing time. Now with new computer performance, 3D image processing and visualization becomes more and more popular.

There are two types of 3D visualization:

- segmentation;
- volume rendering.

Segmentation is the application of synthetic geometric primitives which are obtained from thresholded volume objects.

Volume rendering is more realistic, but more difficult for human eye perception. Very often a combination of segmentation and volume rendering is used.

In our software 1D, 2D and 3D visualization will be realized as screen agent derived from base screen agent class.

## 2.5. Controls agent

Controls agent is responsible for setting and passing the parameters to units. These tools are planned into new software:

- image navigation;
- distance, angle measurement;
- algorithm execution;
- absolute coordinates measurement;
- subvolume selection.

## 3. Conclusions

The described software architecture allows for budget and fast software development for ultrasonic data acquisition system. Flexible software configurability is embedded. Such architecture allows connecting another type of data acquisition equipment such as optical, infrared cameras, X-raying devices etc.

Simple software configuration can be easily grown for more complex tasks.

## References

- [1]. L.Svilainis, G.Motiejunas, "Data acquisition system for air-coupled navigation study: the concept", *Ultragarsas*, No.2(62), 2007, pp.21-25.
- [2]. I.Bitter, et.al. "Comparison of Four Freely Available Frameworks for Image Processing and Visualization That Use ITK", *IEEE Transactions on visualization and computer graphics*, Vol. 13, No. 3, pp.483-493.
- [3]. Advanced Visual Systems, AVS, <http://www.avs.com>, 2006.
- [4]. The Data Visualization & Analysis Platform, IDL, <http://www.rsinc.com/idl>, 2006.

- 
- [5]. MatLab, <http://www.mathworks.com>, 2006.
- [6]. VolView: A Volume Visualization System, Kitware Inc., <http://www.VolView.com>, 2006.
- [7]. MeVisLab: A Development Environment for Medical Image Processing and Visualization, MeVis, <http://www.MeVisLab.de>, 2006.
- [8]. J.Blanchette, M.Summerfield, "C++ GUI Programming with Qt 4", Prentice Hall, 2006.
- [9]. W.Schroder et.al., "The visualization toolkit: an object oriented approach to 3D graphics", 4-th edition, Kitware, 2006, p.512.
- [10].L.Ibanez et.al., "The ITK Software Guide", Insight, 2005. p.836.
- [11].L.Svilainis, V.Puodziunas, "Ultrasonic NDE system: the hardware concept.", Ultragarsas, No.29, 1998, pp.34-40.
- [12].L.Svilainis, N.Saffari, H.Mahlouji, "Signal processing for ultrasonic imaging of composites", conf. proc. Inspection of structural composites, Bentham Press, London, 1994, pp.138-153.



# SIMULATION OF REVERBERATION FOR ACOUSTIC TEACHING

Snejana Pleshkova-Bekiarska, Damian Damianov

*Technical University – Sofia, Bulgaria  
St. Kliment Ohridski, 8  
Tel.: +359 965 3300; E-mail: [snegpl@tu-sofia.bg](mailto:snegpl@tu-sofia.bg)*

## Abstract

Reverberation is an important sound wave propagation process, which provoke the different human perceptions of the original sounds. It is very important for the students and other people learning acoustic to understand the reverberation phenomena in natural and artificial occasions.

Matlab is good instrument for doing reverberation simulation in all kinds of aspects: testing the different methods mathematically describing the reverberation, subjective perception and evaluation of each method etc.

The goal of this paper is to present the structure of programs for simulation of reverberation, that are build in Matlab. The steps, which each student can make, in order to follow the simulation algorithm and to understand the characteristics and applications of artificial reverberation are shown. Some graphical and visualization means to improve the sound wave human perception are also presented.

## 1. Introduction

The phenomena “reverberation” exists in the concert halls recording rooms or in the other places, where the music or other sounds are played [1]. It is very important to know the sound wave propagation in such halls. If there are no walls or other objects, the sound waves consist only off the direct wave

from the source. But this is an unreal situation. There are always reflected sound waves, which are added with direct waves. Therefore the resulting sound wave in each point of the hall is a sum from direct sound wave and an infinite number of reflected sound waves from walls, objects etc.

In a general case it is impossible to know, to calculate or to predict the amplitude and phase of the resulting sound wave in an arbitrary point in a hall. But there are some models and algorithms, which give the possibilities to present the sound wave image in a hall with some admissible tolerances and errors, respectively [2]. To teach students of these methods and algorithms is very usefully and necessary. The students learn the mathematical representation of each method for reverberation modeling. The work with a real programming system gives them the ability for practical simulation of different hall reverberation situation. The students can also better understand the reverberation methods, estimating the sound quality.

The other reason to teach the student of algorithms for reverberations is that the knowledge of these methods let the students realize many special effects using an artificial reverberation system in a concert hall. This is very important for the sound producers and sound operators.

## 2. Matlab simulation of reverberation algorithms

### 2.1. Reverberation algorithm

Figure 1 presents a possible reverberation algorithm [3].

The input signal is first put to a Pre-delay block. After that it is necessary to have a Multitap delay line with a set of n-outputs Tap 1L, Tap 1R, Tap 2L, Tap 2R, ..., Tap nL, Tap nR for left and right stereo sound channels, respectively.

The important parts of each the reverberation algorithm are the blocks of all-pass and comb filters (EQ filters) for recirculation of the early reflections.

The reverberation output (Reverb output) is a mixed sound signal from the early reflections (amplified) and late decay.

It is shown in Fig.1, that in the algorithms, for an extension of the decay time it is necessary to have a Feedback path (Fig. 2).

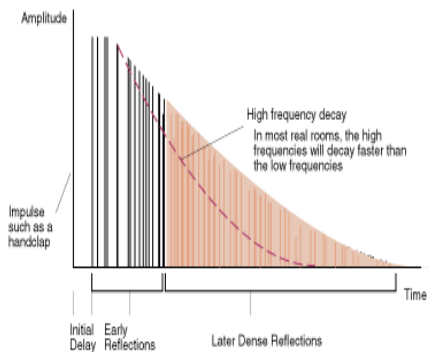


Figure 2. Decay time

### 2.2. Filters representation

In the reverberation algorithm, which is present in Figure.1 the blocks of the filters are present. Some of them are low pass, other – all pas filters. All of them use the output of the Multitap delay line. Its transfer function can be written as:

$$H(z) = z^{-k} \quad (1)$$

The low pass filter transfer function is given by the expression:

$$H(z) = \frac{1-g}{1-gz^{-1}} \quad (2)$$

The low pass filters are used to simulate the air absorption. The gain of the filter is:

$$g = 2 - \cos\left(2\pi \frac{f_c}{f_s}\right) - \sqrt{\left(\cos\left(2\pi \frac{f_c}{f_s}\right) - 1\right)^2 - 1} \quad (3)$$

The low pass filter block diagram used in the Matlab Simulation of the reverberation algorithm is shown in Figure 3.

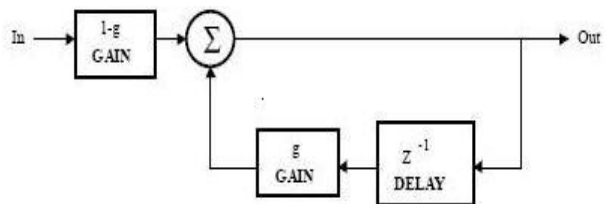


Figure 3. Low-pass filter

### 2.3. Matlab simulation

All of the blocks presented in algorithm of Figure 1 are simulated with Matlab.

There are two ways to make this simulation: as a Matlab program or as a Simulink block diagram representation. Each of these methods has some advantages.

The simulation of the reverberation algorithm as a program allows the students to understand each step of the algorithm precisely, making the program by themselves.

Simulink representation of reverberation algorithm is useful in other direction – there it is possible to make quick changes and to analyze the results with the help of the embedded visualization.

The results of the simulations are given in the Figure 4 and Figure 5.

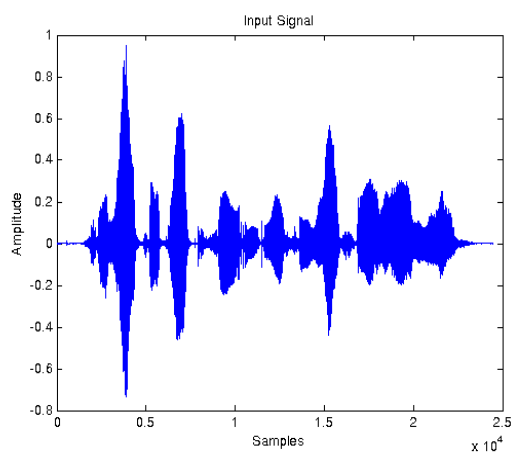


**Figure 4. Input Signal**

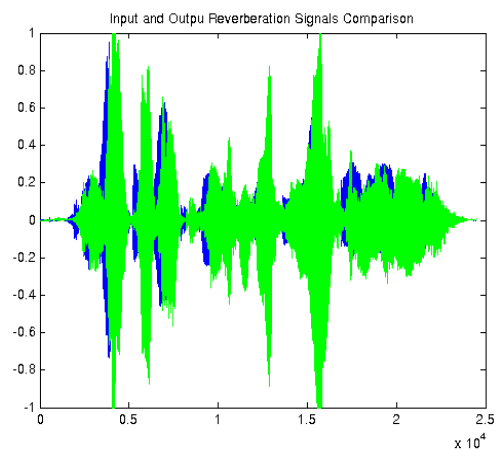


**Figure 5. Input and Output Signal**

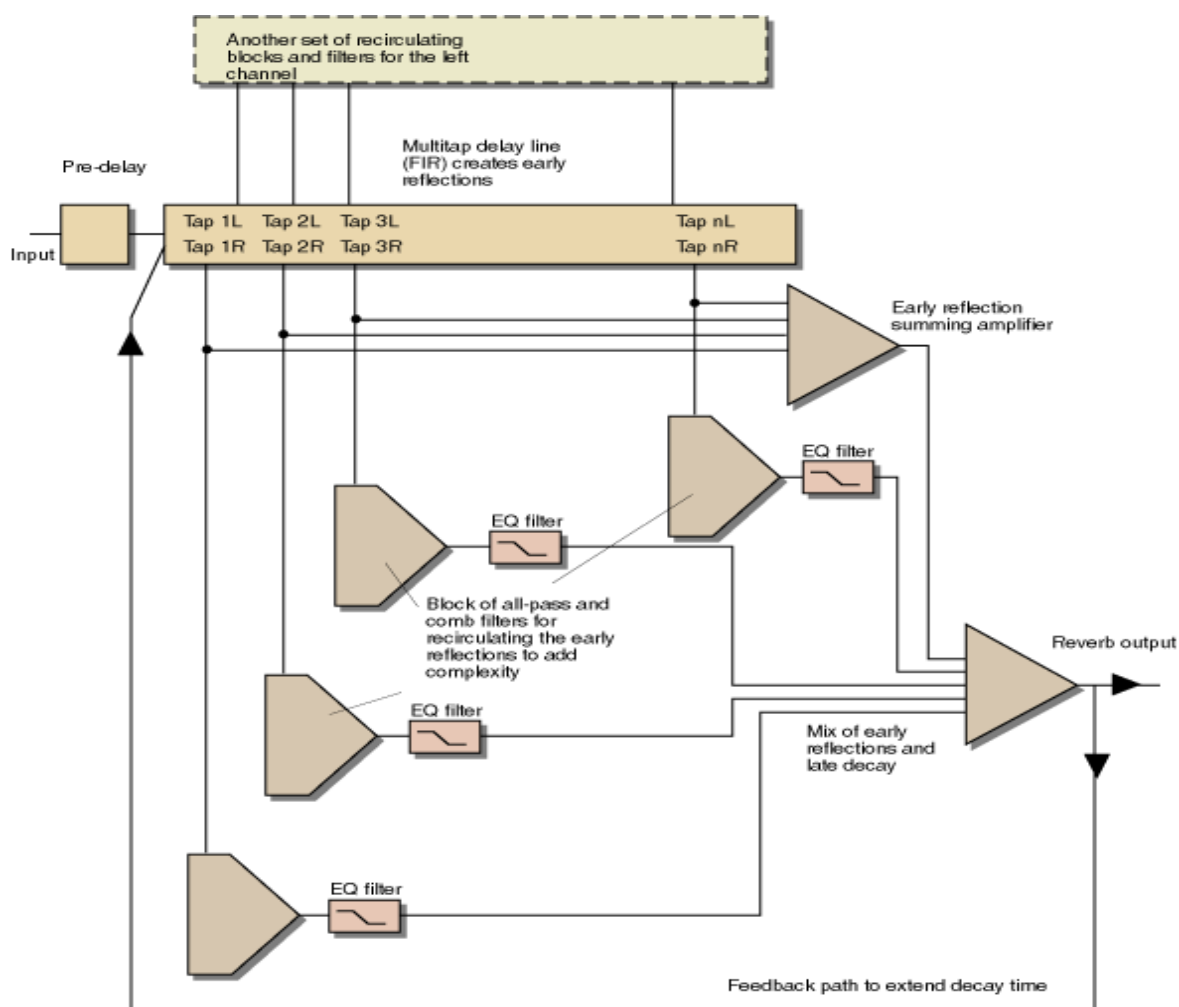


**Figure 1.** Reverberation algorithm

### 3. Conclusion

In the conclusion, it could be summarized that the proposed Matlab simulation of reverberation algorithms in this paper provides a good tools for practical education of the students learning acoustics, for the reverberation is an important part of this course.

### References

- [1]. M. R. Schroeder, "Natural Sounding: Artificial Reverberation", J. Audio Engineering Society. Vol. 10, No. 3, 1961.
- [2]. W. G. Gardner, "Applications of Digital Signal Processing to Audio and Acoustic. Chapter 3. Reverberation Algorithms", Kluwer Academic Publishers, 1998.
- [3]. J. Dattorro, "Effect Design. Part 1: Reverberation and Other Filters", J. Audio Engineering Society. Vol.45, No. 9, 1997.

# COVERAGE PREDICTIONS AND PERFORMANCE ANALYSIS OF SINGLE BASE STATION AND CELLULAR SYSTEMS BASED ON IEEE 802.16 STANDARD

Marko Porjazoski, Borislav Popovski

*University "St's Cyril and Methodius",  
Faculty of Electrical Engineering and Information Sciences – Skopje  
Karpos 2 b.b. 1000 Skopje, R. Macedonia*

## Abstract

*This work provides a approach to evaluate coverage and performance of WiMAX based metropolitan and cellular systems, comprising the most appropriate coverage models currently available (Hata, Walfisch-Ikegami and Stanford University Interim model) and the key system attributes defined in the IEEE 802.16 standard. Coverage and performance estimates are provided, based on real world operation, in accordance to the current European regulatory rules, which respectively handles operation in licensed 3.5 GHz band. For dimensioning single base station WiMAX system, the worst case CNR is relevant parameter. For cellular WiMAX network, interference generated by co-channel cells that utilize the same frequency channel must be considered.*

*The main contribution of this paper is coverage and performance evaluation of WiMAX systems, assuming ideal transmission power control.*

## 1. Introduction

WiMAX or IEEE 802.16 is a radio access technology that offers performances similar to wired xDSL systems. Different deployment concepts are foreseen for WiMAX networks. They can cover metropolitan or isolated areas, private campus networks, and remote

neighbourhoods. Even more WiMAX can be deployed as a cellular network that offers ever-present broadband services over large geographic regions to mobile subscribers.

Detailed procedures for coverage prediction and performance evaluation of IEEE 802.16 networks are not yet clearly stated in the literature for general operation conditions. This situation is result of lack of appropriate coverage prediction models that comply with operation frequencies requirements of WiMAX, especially for frequencies ranging from 2 GHz up to 6 GHz.

Coverage and performance predictions for metropolitan and cellular systems based on 802.16 standard is in the focus of our work. For these purposes, we are using different path loss propagation models (like Hata, Walfisch-Ikegami and SUI). These models are suitable for modelling different LOS and NLOS operation scenarios, despite the fact that they are inherited from techniques for radio network planning for earlier mobile and wireless systems.

The remaining of this document is organised as follows: Section 2 presents key features of the IEEE 802.16 standard and the major aspects of the technology. Section 3 describes the coverage and performance evaluation of WiMAX wireless networks, based on appropriate propagation models, as

well as on analytical formulas for the OFDM receiver sensitivity and maximum data transmission rate. In Section 4, some basic concepts on WiMAX cellular system dimensioning and deployment are explained. Section 5 concludes the paper.

## 2. OFDM and IEEE 802.16 technology

Basic architecture of IEEE 802.16 based wireless networks comprises Base Station (BS) and Subscriber Station (SS), operating in Point – to – Multipoint mode. BS coordinates medium access control and SS provides network access to the subscriber via a wireless link to the BS. IEEE 802.16 systems can operate in different LOS or NLOS environments. The first step to enable NLOS propagation is to reduce the carrier frequency below 11 GHz. Furthermore, by using appropriate techniques, we can take advantage on multipath that appears at the lower frequencies.

The key technique that enables NLOS operation of WiMAX is Orthogonal Frequency Division Multiplexing (OFDM). OFDM operation consists of multiplexing information on  $N$  narrow-band sub-channels, each modulated by a set of orthogonal sub-carriers.

The OFDM scheme specified in the IEEE 802.16 standard is presented in Figure 1. The OFDM symbol is composed of a useful symbol interval ( $T_b$ ) and the guard interval ( $T_g$ ), named Cyclic Prefix (CP). The resulting symbol duration is  $T_s = T_b + T_g$ , (Figure 1a).

OFDM spectrum consists of different types of sub-carriers (Figure 1c). Only data sub-carriers are employed for data transmission. Other sub-carrier are used for channel estimation and inclusion of guard bands between groups of sub-carriers.

In addition to OFDM multiplexing, adaptive modulation is adopted in the IEEE 802.16 standard. Depending on

the signal-to-noise ratio (SNR) at the receiver, the SS and the BS negotiate the most appropriate modulation scheme, among the available options (BPSK, QPSK, 16 QAM and 64 QAM). Adopted modulation and coding schemes, defined in the IEEE 802.16 standard, along with the required SNR are listed in Table 1.

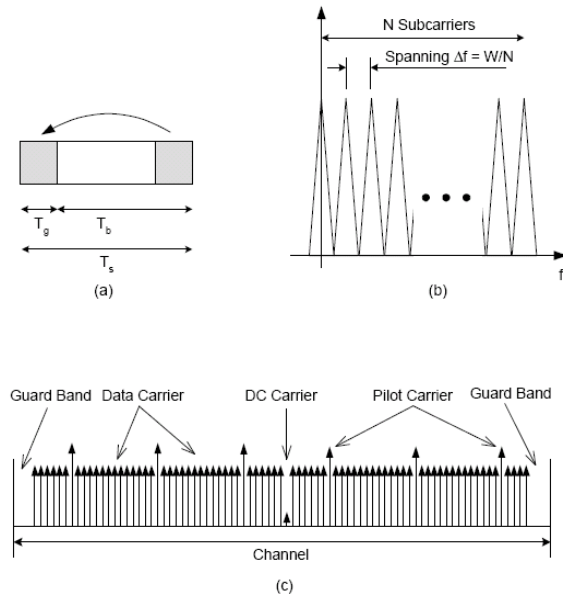


**Figure 1.** OFDM technique in IEEE 802.16: (a) symbol structure; (b) orthogonal subcarriers; (c) data, DC and pilot subcarriers.

### Coding schemes defined in the IEEE 802.16 standard, along with required SNR

Modulation	Coding	SNR
BPSK	1/2	6.4
QPSK	1/2	9.4
	3/4	11.2
16-QAM	1/2	16.4
	3/4	18.2
64-QAM	2/3	22.7
	3/4	24.4

## 3. Coverage and performance prediction of single BS WiMAX system

Coverage and performances of any wireless system are closely related to propagation losses in wireless environment. Propagation loss estimation is a key factor in wireless network planning.

Link budget calculation (see equation 1) defines maximum propagation loss tolerated by system in the specific scenario.

$$P_r = \frac{P_T \cdot G_{BS} \cdot G_{SS}}{L_T} \quad (1)$$

$P_r$  is received power,  $P_T$  is transmission power,  $G_{BS}$  and  $G_{SS}$  are BS and SS antenna gains, and  $L_T$  is total system loss including radio propagation loss  $PL$ , cable losses and fading margin.

Signal to (Noise + Interference) ration is defined by:

$$SNR = \frac{P_r}{P_N + Int} \quad (2)$$

where  $P_N = kTWF$  is thermal noise power at the receiver with effective channel bandwidth  $W$ , noise figure  $F$ , at temperature  $T$  in Kelvin.  $k = 1.38 \times 10^{-23}$  J/K is Boltzmann's constant.  $Int$  is a interference caused by the neighbouring BSs, and in the single BS scenario  $Int=0$ .

Having in mind required SNR for modulation formats defined by the IEEE 802.16 standard, we can calculate receiver sensitivity  $P_{r,min}$  as:

$$P_{r,min} = SNR_{target} (kTWF + Int) \quad (3)$$

Taking into considerations the European regulations about maximum EIRP in the 3.5 GHz band, and using appropriate formula (model) for path loss propagation, we can evaluate coverage for WiMAX system. We are using three different path loss propagation models Hata, Walfisch – Ikegami and SUI, for different deployment arrays: urban, sub-urban and rural.

Having in mind that OFDM scheme in IEEE 802.16 standard does not allocate the entire channel bandwidth for information transmission, the effective bandwidth  $W$  can be computed as:

$$W = \left\lfloor \frac{n \cdot BW}{8000} \right\rfloor \cdot 8000 \cdot \frac{N_{used}}{N_{FFT}} \quad (4)$$

where  $n$  is the sampling factor and  $BW$  is the channel bandwidth in Hz,  $N_{used}$  are data carriers and  $N_{FFT}$  are all available sub-carriers,

Finally, receiver sensitivity for OFDM can be calculated as:

$$P_{r,min} = SNR_{target} \left( kTF \cdot \left\lfloor \frac{n \cdot BW}{8000} \right\rfloor \cdot 8000 \cdot \frac{N_{used}}{N_{FFT}} \right) \quad (5)$$

Parameters, specified by IEEE 802.16d standard, that we are going to use in our calculations are listed in Table 2.

**Table 2. OFDM Parameters, According To IEEE 802.16 Standard**

Parameter	OFDM value
<b>N<sub>used</sub></b>	192
<b>N<sub>FFT</sub></b>	256
<b>G</b>	1/4, 1/8, 1/16 and 1/32
<b>n</b>	8/7, for BW a multiple of 1.75 MHz

In order to compare WiMAX system behaviour in different deployment environments, we used three widely adopted path loss models:

- Hata model-for urban arrays:

$$L = 46.3 + 33.9 \log f - 13.82 \log h_{te} - a(h_{re}) + (44.9 - 6.55 \log h_{te}) \log d + C_M \quad (6)$$

where

$$a(h_{re}) = 3.2(\log 11.75 h_{re})^2 - 4.97 \text{ dB}$$

$$C_M = \begin{cases} 0 \text{ dB} & \text{for medium sized city} \\ 3 \text{ dB} & \text{for metropolitan centers} \end{cases}$$

$f$  is a carrier frequency  $h_{te}$  and  $h_{re}$  are BS and SS antenna heights respectively.

- Walfisch-Ikegamimodel-for suburban arrays:

$$L = \begin{cases} 42.64 + 20 \log(f_c) + 26 \log(d) & \text{if } d < d_c \\ 42.64 + 20 \log(f_c) + 26 \log(d_c) + 40 \log(d/d_c) & \text{if } d \geq d_c \end{cases} \quad (6)$$

where  $d_C = 4h_t h_r / \lambda$  is the break-point distance, with  $h_t$  and  $h_r$  being the transmit and receive antenna heights, respectively.

- SUI model for rural arrays:

$$L = A + 10\gamma \log\left(\frac{d}{d_o}\right) + \Delta L_f + \Delta L_h \quad (7)$$

where:

$$d_o = 100 \text{ m}, A = 20 \log(4\pi d / \lambda)$$

$$\gamma = (a - b h_b + c / h_b)$$

$$\Delta L_f = 6 \log\left(\frac{f}{2000}\right)$$

$$\Delta L_h = \begin{cases} -10.8 \log\left(\frac{h}{2}\right) & \text{for terrain Types A and B} \\ -20 \log\left(\frac{h}{2}\right) & \text{for terrain Type C} \end{cases}$$

Parameters a, b and c specifies different type of terrain, where WiMAX system is planned to be deployed. They are listed in Table 3.

**Table 3. SUI model parameters**

Parameter	Terrain A Mountains	Terrain B Hills	Terrain A Flat Terrain
a	4.6	4	3.6
b	0.0075	0.0065	0.005
c	12.6	17.1	20

For detailed coverage and performance evaluation we have assumed SS antenna height  $h_r = 3$  meters, BS antenna heights  $h_t = 30$  meters, carrier frequency  $f_c = 3.5$  GHz band this break distance  $d_C = 4200$  meters.

**Table 4. Estimated Uplink/Downlink Coverage Radius In Km**

Radius [km]	BW=7 MHz, P <sub>t</sub> = 30 dBm, G <sub>BS</sub> = G <sub>SS</sub> = 3dBi						
	BPSK			16-QAM			
	1/2	1/2	3/4	1/2	3/4	2/3	3/4
W-I	2.49	1.9	1.62	1.02	0.87	0.58	0.50
Hata	1.2	0.98	0.87	0.62	0.55	0.41	0.37
SUI – Type 2	0.86	0.73	0.67	0.5	0.46	0.36	0.33

By using equations (1) - (7), consideration the maximum BS and SS transmis-

sion of 30 dBm, channel bandwidth 7 MHz, antenna gains of 3dBi, we can evaluate maximal distance between BS and SS, and maximum achievable data rate through the radio interface. Results from the evaluation are presented in Table 4 Table 5 and Figure 2, Figure 3.

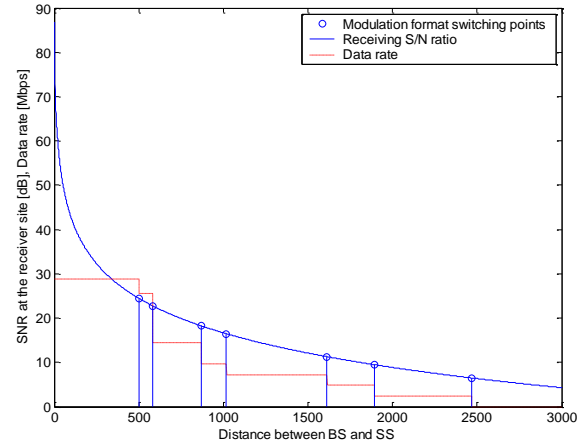


**Figure 2. SNR, Bit Rate and Modulation Switching point dependence on BS-SS distance for W-I path loss model**

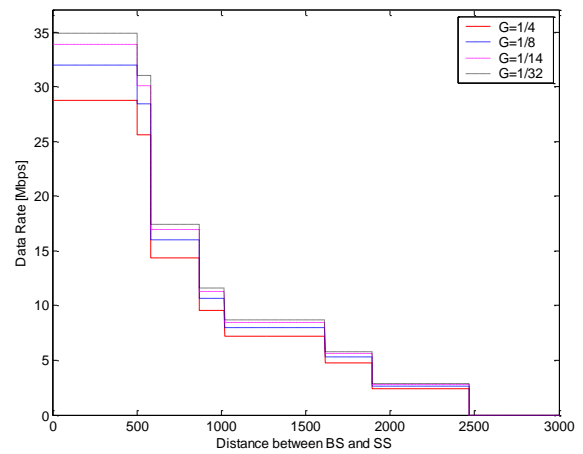


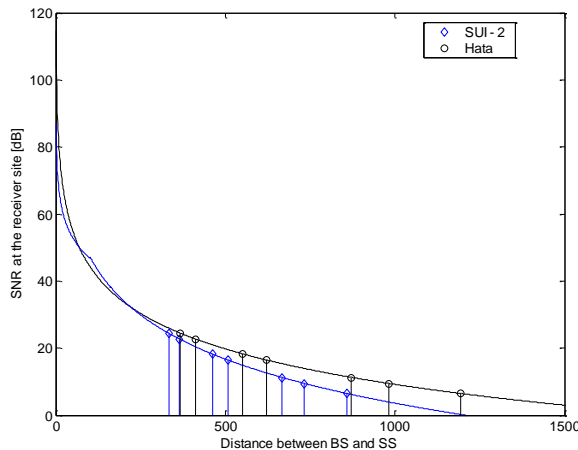
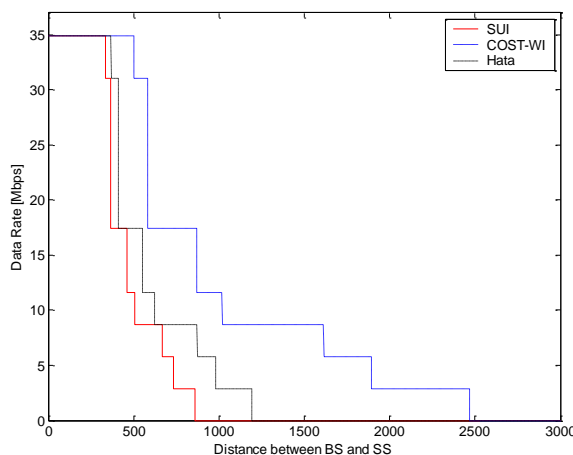
**Figure 3. Bit Rate dependence on cyclic prefix duration and BS to SS distance for W-I path loss model.**

From the presented result, it is clear that maximum data rate approximately 35 Mbps can be achieved with 64-QAM modulation format and  $\frac{3}{4}$  coding rate. But this modulation scheme provides worst coverage. When increasing the distance between BS and SS, level of SNR at the receiver site is decreasing. At certain point, SNR becomes too low to support ongoing modulation format.



**Table 5. Maximum transmission data rates through IEEE 802.16 Air Interface in Mbps**

	BPSK	QPSK		16-QAM		64-QAM	
G	1/2	1/2	3/4	1/2	3/4	2/3	3/4
1/4	2.4	4.8	7.2	9.6	14.4	25.6	28.8
1/8	2.66	5.33	8	10.66	16	28.44	32
1/16	2.82	5.64	8.47	11.29	16.94	30.11	33.88
1/32	2.90	5.81	8.72	11.63	17.45	31.03	34.90

**Figure 4.** Comparison of SNR and modulation switching points dependence on BS-SS distance for Hata and SUI path loss models**Figure 5.** Comparison of achieved bit rate for different path loss models

The system is trying to maintain the connection so it switches on lower modulation format with lower data rates. At some distance SNR becomes so low ( $< 6.4$  dB), that BS can't provide any service to the SS.

Figures 4 and 5 provide comparison of behaviour of WiMAX system in different deployment environments in the

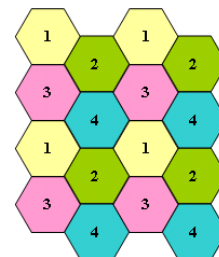
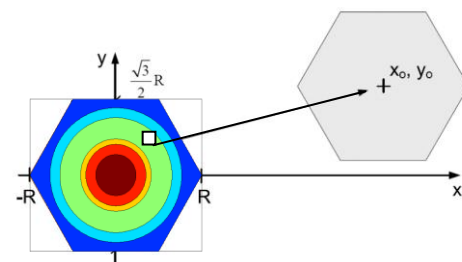
mean of coverage areas and supported bit. Severe propagation conditions decreases SNR and supported data rates more quickly with the distance, presenting smaller coverage arrays.

According to this analysis, coverage array of WiMAX system in NLOS scenarios is:

- 2.5 km according to Walfisch – Ikegami model
- 1.2 km for Hata propagation model and
- 0.86 km for SUI model.

#### 4. Dimensioning Cellular WiMAX

In order to cover grate geographical regions, with limiter number of radio channels, wireless systems are organized in cells. To avoid interference in cellular networks, cells are organized into clusters, assigning unique frequency for each cell in the cluster (Figure 6).

**Figure 6.** Cellular system with cluster order 4**Figure 7.** Co-channel interfering cells

BSs and SSs from the co-channel cells introduce interference into system. In order to minimize interference, we have adopted ideal power control, meaning that transmission power at each

SS is set to minimal value satisfying required Signal to (Noise + Interference) Ratio (SNIR), at the receiver site at its own BS. Maximum transmission power is limited to 30 dBm.

Two interfering co-channel cells are presented in Figure 7. The cell of interest have BS with coordinates  $(x_0, y_0)$ , and co-channel cell that generates interference with BS located at  $(0, 0)$ . Zones in the cell supporting different modulation formats are represented with different colours, starting with BPSK at the cell boundary, up to 64-QPSK at the centre of the cell. Distance between co-channel interfering cells depends on cluster size. Mean uplink interference level at the BS located at  $(x_0, y_0)$  can be calculated averaging received signal from users located at co-channel cell.

We will assume that user located at  $(x, y)$  transmits with power sufficient to satisfy SNIR at BS located at  $(0, 0)$ .

$$P_{T,(x,y)} = \frac{SNR_{target} \cdot L(x, y) \cdot (P_N + 6 \cdot Int)}{G_{BS} \cdot G_{SS}} \quad (8)$$

$SNR_{target}$  is required signal to noise ratio,  $G_{BS}$  and  $G_{SS}$  are BS and SS antennas gain,  $L(x, y)$  is path loss between SS and its own BS located at  $(0, 0)$ ,  $P_N$  is thermal noise power and  $Int$  is averaged interference from one of six co-channel cells in the first tier.

Received power or interference that user located at  $(x, y)$  causes at observed BS, located at  $(x_0, y_0)$ , is:

$$\begin{aligned} P_{R,(x-x_0,y-y_0)} &= \frac{P_{T,(x,y)} \cdot G_{BS} \cdot G_{SS}}{L(x-x_0,y-y_0)} \\ &= SNR_{target} \cdot (P_N + 6 \cdot Int) \cdot \frac{L(x, y)}{L(x-x_0,y-y_0)} \end{aligned} \quad (9)$$

Averaging received signal power from users located in co-channel cell, we can obtain mean interference from one co-channel cell in uplink.

$$Int = \frac{1}{cell\ area} \int \int_{x\ y} P_{R,(x-x_0,y-y_0)} dy dx \quad (10)$$

Using equations (8-10) we have evaluated influence of neighbouring cells on maximum coverage in uplink direction that one cell can provide. Results from this evaluation are presented in Figure 8.

Coverage prediction for downlink can be made by using similar method. In downlink case, BSs from neighbouring cells are interference originators.

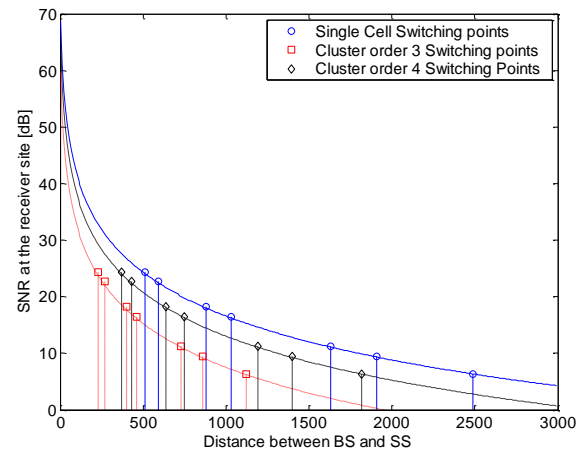


**Figure 8.** Coverage predictions in uplink direction for WiMAX cellular system with cluster order 3 and 4

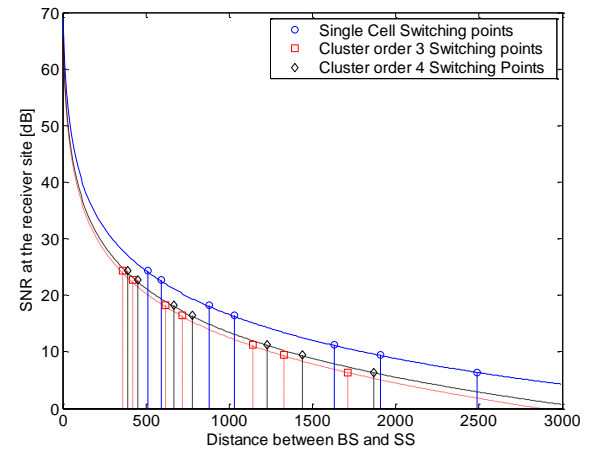


**Figure 9.** Coverage predictions in downlink direction for WiMAX cellular system with cluster order 3 and 4

We have assumed worst case scenario where BS are transmitting with maximum allowed transmission power.

Results from the downlink analysis are presented in Figure 9.

It is obvious that interference from the neighbouring cells isn't negligible. For systems with smaller cluster sizes interference will cause significant reduction of cell coverage.

## 5. Conclusion

This work covers evaluation of coverage and performances of WiMAX system. During this evaluation we came to several important conclusions. Performances and coverage of metropolitan or cellular WiMAX systems depends on propagation conditions and path losses introduced by the radio environment.

By using several propagation models and assuming maximum transmission power of 30 dBm we have obtained single BS coverage in NLOS operation mode. For suburban environments maximal coverage of 2.5 km was calculated and maximum data rate of 35 Mbps for users near to BS.

The analysis of cellular WiMAX system shows that interference in both uplink and downlink can cause significant reduction of cell coverage. This problem can be solved by organizing cells into higher order clusters, consuming

more non-overlapping channels from limited frequency spectrum.

## References

- [1]. Theodore S. Rapaport, *Wireless Communications-Principles and Practice*, Prentice Hall, December 2001,
- [2]. Hassan Yaghoobi, "Scalable OFDMA Physical Layer in IEEE 802.16 WirelessMAN", Intel Technology Journal, Volume 8, August 2004,
- [3]. Christian Hoymann, "Analysis and performance evaluation of the OFDM-based metropolitan area networks IEEE 802.16", Elsevier Computer Networks, No. 49, May 2005,
- [4]. Christian Hoyman, Stephan Goebbels, "Dimensioning Cellular WiMAX, Part I: Singlehop Networks", In Proceedings of European Wireless 2007, p. 7, Paris, France, April 2007,
- [5]. Fabricio Lira Figueredo, Paulo Cardieri "Coverage prediction and performance evaluation of wireless metropolitan area networks based on IEEE 802.16", IEEE Journal of communication and information systems", Vol. 20, No. 3, 2005
- [6]. "Digital Mobile Radio Towards Future Generation Systems", COST 231 Final Report, [http://www.lx.it.pt/cost231/final\\_report.htm](http://www.lx.it.pt/cost231/final_report.htm)
- [7]. V. Erceg et. Al, "Channel Models for Fixed Wireless Applications", IEEE 802.16 Broadband Wireless Access Working Group, Jun 2003.

# THE MEASUREMENT OF WLAN THROUGHPUT USING DIFFERENT SECURITY PROTOCOLS

**B. Dekeris, L.Narbutaite**

*Telecommunication department, Kaunas University of Technology  
Studentu str. 50, LT-51368 Kaunas, Lithuania  
T, +370 37 300505; E,brunonas.dekeris@ktu.lt / lina.narbutaite@ktu.lt.*

## **Abstract**

*802.11 wireless LANs continue to gain market momentum. Now, with this growing adoption of 802.11 wireless LANs, security has become a focal point regarding the decision to deploy a wireless LAN.*

*In this paper we analyze the wireless LAN throughput using different security protocols. While defining the right security layout, theoretical throughput of channel was calculated and compared to practical rates of wireless local area network channel, using different safety layouts.*

*This paper also addresses the different issues related to the security protocols currently used in WLAN IEEE 802.11 and demonstrates how these issues affect the final results of the experiments conducted. The results show that within the same access point range the security adds moderate degradation on the throughput that may affect some applications over both infrastructure and ad hoc WLANs.*

## **1. Introduction**

Over recent years, the market for wireless communications has experienced considerable growth. Wireless technologies have found an important place and popularity in business, the computer industry and medical clinics [1-2].

Unlike its wired network counterpart, where the data remains in the cables connecting the end devices, the transmission in a wireless network takes the form of broadcast radio frequency (RF) signals, which uses the open air as a medium for its movements. Hence the broadcast nature of WLAN introduces a greater risk from intruders who may gain unauthorized access to, or even corrupt, the transmitted data [3].

Since applying security to wireless networks is a very new yet an active area, intensive research was recently devoted to clarify remaining ambiguities, to identify limitations and difficulties, to propose solutions and to improve the performance of these networks[4].

## **2. WLAN security protocols**

To defend the WLAN from the above listed security threats, and others, there are considerable number of security protocols that in the market today. Due to the limited size of this paper, we will discuss only the Wired Equivalent Privacy (WEP) and WPA IPsec VPN, which is considered as the industry standard for WLAN security.

WEP was the original native security mechanism for WLAN developed by IEEE members in order to provide security through a 802.11 network. WEP allows a person to set up a 40 or 128-bit security key that is shared between

a mobile device and an access point. This key will encrypt all of the information that is transmitted on the network; however, in order for it to be effective, it must be configuration into all devices that connects to a wireless network through the access point [4-5]. WEP uses the RC4 as its underlying algorithm. RC4 is a symmetric algorithm.

WPA enables 802.1x/EAP authentication along with Temporal Key Integrity Protocol (TKIP) encryption that is based on RC4. The components of WPA include:

WPA delivers a greatly enhanced encryption scheme called Temporal Key Integrity Protocol (TKIP). TKIP increases the key from 40 to 128 bits, and relies on dynamically generated session keys. 802.11i or WPA2 also provides a new encryption scheme called Advanced Encryption Standard (AES). AES enables security between workstations, and uses an algorithm that employs variable keys of 128, 192, or 256 bits [4].

A VPN creates a “tunnel” between each remote site and the host site allowing for communication. A VPN server is needed at the host site to terminate the “tunnel” as well as to provide the authentication and encryption. All traffic passing through the “tunnel” is encrypted. The more significant difference being, the traffic is protected by robust encryption techniques. Many times the encryption technique is IP-Sec, which is considered secure by government standards.

### 3. WLAN 802.11 throughput measurement

The objective of this research was How do different security mechanisms affect the performance (throughput).

#### 3.1. Experimental configuration

The tested network structure is presented in Figure 1.

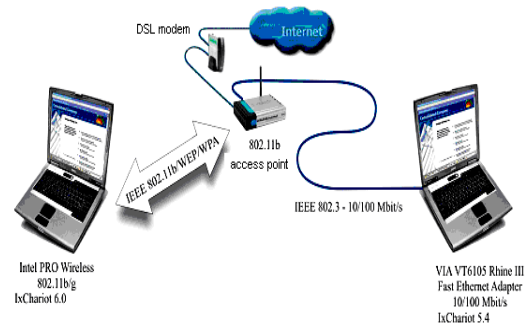


Figure 1. Tested network structure

The experiment were based upon Windows XP (clients). The measurement are used with IxChariot software equipment, SNR~69 dB. The measurement time of every case was 600 sec.

#### 3.2. WEP, WPA measurement

For comparison our results, we used 3 case: non coding channel, WEP 128-bits key and WPA. The results are presented in figures 2-3.

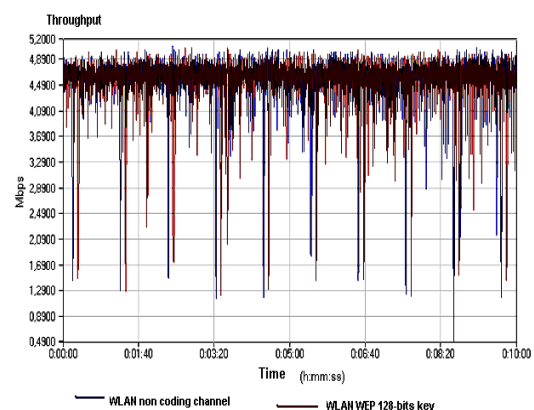


Figure 2. Throughput measurement using non coding and WEP 128-bit key channel

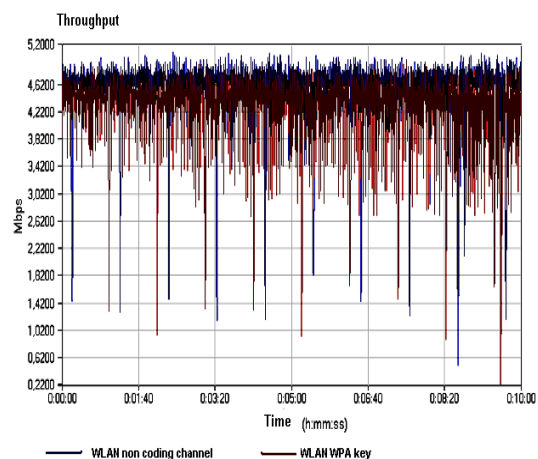


Figure 3. Throughput measurement using non coding and WPA protocol

Figures 2-3 indicate that using all 3 case we got the similar result:

- the maximum channel throughput is 5.06 Mbps;
- the average channel throughput is 4.49 Mbps.

### 3.3. IPsec VPN tunnel measurement

The tested network structure is presented in Figure 4.

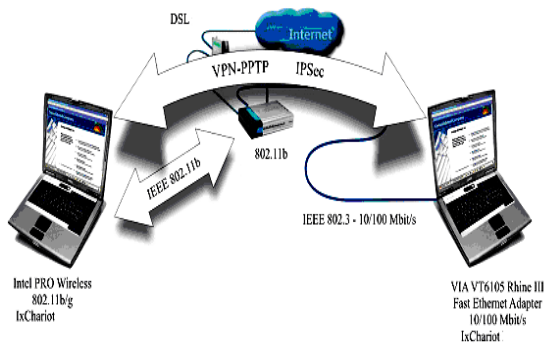


**Figure 4.** Tested network structure using VPN IPsec protocol

In this scenarios we used 1 and 2 VPN tunnels. The results are presented in Figure 5.

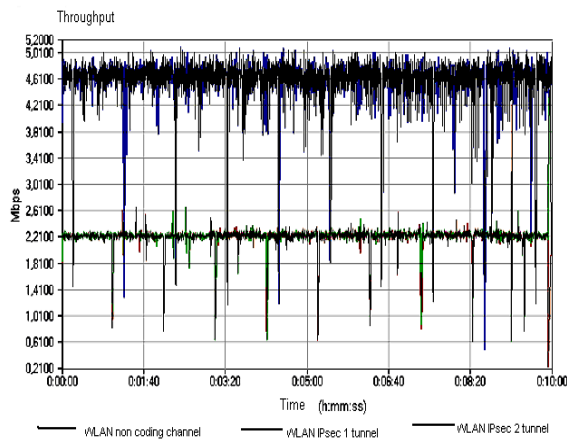


**Figure 5.** Throughput measurement using non coding and IPsec protocol

Comparison with results presented in the figures 2-3, we can see that in this case throughput decrease (2.2 time) than non coding channel throughput. This is due to the fact that encryption

operations performed by these protocols increase the amount of data transmitted and slow down the rate of data being sent or received.

## 4. Theoretical WLAN throughput calculation

In order to determine the throughput of the system it is necessary to analyze the MAC layer of the IEEE 802.11b system. A data packet consists of overhead (preamble and header) and the data portion. The time to transmit this packet is shown below [ 6 ]:

$$T = DIFS + OH + \frac{M}{R} + SIFS + ACK, \quad (1)$$

where OH – overhead; M - data (bits); r – rate (bps).

*DIFS*, *SIFS* as well as *ACK* frame are considered here because they are necessary to ensure a correct reception of packet.

The average time for a correct transmission to be received is given by

$$T_{aver} = T + (1 - p) \cdot \sum_{i=1}^{\infty} i \cdot p^i \cdot T, \quad (2)$$

where p – the probability of a packet being received in error (PER), it is calculated by formula

$$PER = 1 - (1 - P_{ber})^N, \quad (3)$$

where N – number pf bits in the packet,  $P_{ber}$  - the probability of bit error.

The  $P_{ber}$  is calculated [ 7 ]:

$$P_{ber} = \frac{2^{k-1}}{2^k - 1} \left( \sum_{m=1}^{M-1} \frac{(-1)^{m+1} \binom{M-1}{m}}{1 + m + m8\Gamma} \right), \quad (4)$$

where  $M = \frac{1}{2} \cdot 2^k$  - k is a number of bits

in the symbol and  $\Gamma = \sqrt{\frac{2E_b}{N_m}}$ .

Then throughput is

$$C = \frac{M}{T} (1 - PER). \quad (5)$$

MAC frame parameters: SIFS= 10 $\mu$ s, DIFS = 50 $\mu$ s, ACK = 112  $\mu$ s, packet size= 1500 bytes.

The graphs for the throughput for four different rates are presented Figure 6.

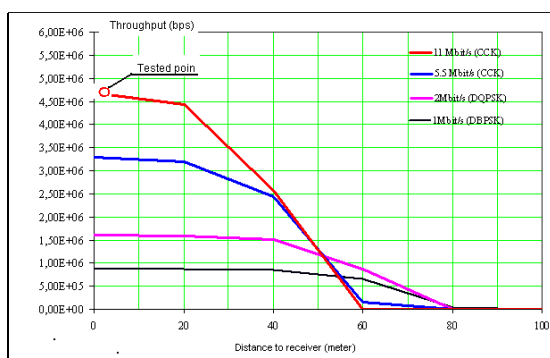


**Figure 6.** Theoretical throughput of the 802.11

From the figure 6 we can observe the efficiency of each data rate versus distance. 11Mbps gives best throughput for the first 20 meters and throughput is 4.7Mbps.

## 5. Conclusions

The theoretical calculation and experimental throughput measurement results present that throughput decreases when security protocol WEP WPA and IPsec are enabled. Using WEP or WPA security protocol the theoretical differ from measurement throughput very small, but if we use VPN IPsec, the throughput decrease 2.2 time.

## References

- [1]. Karygiannis. "Wireless Network Security 802.11, Bluetooth and Handheld Devices". NIST, 2002, 119p.
- [2]. Abderrahmane Lakas. "A Framework for SIP-Based Wireless Medical Applications", IEEE Communications, 2004, pp1-5.
- [3]. Brener P. A technical tutorial on the 802.11 protocol. 2004
- [4]. Nilufar Baghaei. Security performance of loaded IEEE 802.11b wireless networks. Computer Communications 27, 2004, pp.1746–1756.
- [5]. Aaron E. Earle. "Wireless Security Handbook", Taylor & Francis Group, 2006, p 347.
- [6]. Rindzevičius, Grimaila. Pilkauskas, "Traffic analysis of the next generation wireless access technologies", IPSI - 2006 AMALFI, 2006, pp.1-7.
- [7]. Fainberg M. "Performance analysis of the IEEE 802.11b local area network", 2001, pp 26-35.



# NON-RELATIVISTIC MOTION OF IONS IN LIVE TISSUES

Boncho Angelov Bonchev

Technical University of Sofia, Bulgaria  
[boncho71@abv.bg](mailto:boncho71@abv.bg)

## Abstract

*In this paper certain aspects are considered of the motion in live tissues of ions under influence of an electromagnetic field. Some results of computer simulation of space configuration of low frequency magnetic field around the human body is presented, also.*

## Introduction

The problem that presents itself is that of solving the equations of motions given in relativistic form, namely

$$\frac{d}{dt} \left[ \frac{m_0 \vec{v}(t)}{\sqrt{1 - \frac{|\vec{v}(t)|^2}{c^2}}} \right] = e[\vec{E}(t) + \vec{v} \times \vec{B}(t)] \quad (1)$$

The problem becomes, in principle, straightforward if it be assumed that  $\vec{E}$ ,  $\vec{B}$  appearing in the right-hand side of (1) is a given field; the difficulties are then of purely technical kind that can also arise in traditional particle mechanical forces. The assumption is often a legitimate approximation, and the most of the work presented here is in this context. In fact, however, the charge itself also contributes to the electromagnetic field, and its contribution depends on its motion. The inclusion of this “self-force” presents quite fundamental difficulties because of the infinities associated with the concept of a point charge. Attempts to describe the motion of an electron

can perhaps be classified in terms of the following alternatives (a) abandon the idea that the electron is a point charge, and give it some intrnal structure; (b) introduce into classical mathematical framework some formalism that succeeds in discarding the infinities; (c) abandon the idea that the electron can be described in any fundamental way by classical theory, and insist that appeal be made to quantum laws. The procedure (b) has been given a good deal of attention, and has led to an equation of motion which at least in certain contexts is acceptable theoretically and is in general agreement with practice. A derivation of this equation is given later in paper. Any discussion of alternatives(a) and (c) is outside the scope of this paper.

## 1. Equation of motion

In attempting to solve (1) it may helpful to make use of the associated energy equation

$$\frac{d}{dt} \left( \frac{m_0 c^2}{\sqrt{1 - \frac{v^2}{c^2}}} \right) = e \vec{E} \cdot \vec{v} \quad (2)$$

If the electric field is purely static, so that  $\vec{E} = -\text{grad} \phi$ , this gives

$$\frac{m_0 c^2}{\sqrt{1 - \frac{v^2}{c^2}}} + e\phi = \text{const} \quad (3)$$



In the important special case  $\vec{E} = 0 \Rightarrow \vec{v} = \text{const}$ . Since a time-varying magnetic field cannot exist without an associated electric field. When

$v = \text{const}$   $\vec{v}$  is along the principal normal to the trajectory and of magnitude

$\frac{v^2}{p_p}$ , where  $p_p$  is the principal radius of curvature; hence

$$p_p = \frac{m_0 v}{eB \sin \theta \sqrt{\left(1 - \frac{v^2}{c^2}\right)}}, \quad (4)$$

where  $\theta$  is the angle between  $\vec{B}$  and  $\vec{v}$ , commonly called the pitch angle.

Often it is not necessary to take account of relativistic effects, and the equations of motions and energy equation can then taken as

$$m \frac{d\vec{v}(t)}{dt} = e[\vec{E}(t) + \vec{v}(t) \times \vec{B}(t)] \quad (5)$$

$$\frac{d}{dt} \left( \frac{1}{2} m v(t)^2 \right) = e \vec{E} \cdot \vec{v} \quad (6)$$

It may be noted that in the case  $\vec{E} = 0$ ,

Where the field is purely magnetostatic, the relativistic equations are the same as the non-relativistic, except only that  $m$  in the latter is replaced by the constant

$$\frac{m_0}{\sqrt{\left(1 - \frac{v^2}{c^2}\right)}}.$$

It is well known that the equations of motion can be cast into two alternative forms, familiar in classical mechanics as Lagrangian and Hamiltonian forms. In the present calculations no extensive use is made of these forms, but it is convenient to state theme here. In the non-relativistic treatment the usual form of Lagrange's equations is equivalent to (5) if the Lagrangian is taken as

$$L = \frac{1}{2} m v^2 + e \vec{v} \cdot \vec{A} - e \phi, \quad (7)$$

where

$\phi$  is scalar potentials of the electromagnetic field

$\vec{A}$  is vector potentials of the electromagnetic fields.

Likewise the usual form of Hamilton's equations is equivalent to (5) if the Hamiltonian is taken as

$$H = \frac{1}{2m} (\vec{p} - e \vec{A})^2 + e \phi, \quad (8)$$

where

$$\vec{p} = m \vec{v} + e \vec{A}$$

is generalized momentum.

To recapture the relativistic equation (1) the Llagrangian has to be

$$L = -m_0 c^2 \sqrt{\left(1 - \frac{v^2}{c^2}\right)} + e \vec{v} \cdot \vec{A} - e \phi. \quad (9)$$

The corresponding relativistic Hamiltonian is

$$H = c \sqrt{\left\{ m_0^2 c^2 + (\vec{p} - e \vec{A})^2 \right\}} + e \phi,$$

whit

$$\vec{p} = \frac{m_0 \vec{v}}{\sqrt{\left(1 - \frac{v^2}{c^2}\right)}} + e \vec{A}. \quad (10)$$

in what follows consideration is given first to exact solution of (5) for some simple special cases, starting with uniform and constant

$$\vec{E}(x, y, z, t) = \text{const} \wedge \vec{B}(x, y, z, t) = \text{const}$$

## 2. Non-relativistic motion in simple in live tissues

### 2.1. Uniform static fields

When both  $\vec{E}$  and  $\vec{B}$  constant in time and uniform in space, that is, each vector always and everywhere

has the same magnitude and same direction, the full solution in the non-relativistic approximation is easily obtained.

First it is noted that in a uniform electrostatic field  $\vec{E}$ , with no magnetic field, the particle simply travels in a straight line with constant acceleration  $e\vec{E}/m$ .

Next, motion in a uniform magnetostatic field  $\vec{B}$ , with no electric field, is considered. The speed  $v$  is then constant; so is  $v_{\parallel}$ , since the force is at right angles to  $\vec{B}$ , and so also therefore is the magnitude  $v_{\perp}$  of  $\vec{v}_{\perp}$ , where suffices  $\parallel$  and  $\perp$  are used to denote components parallel and perpendicular to  $\vec{B}$ . Now for motion perpendicular to  $\vec{B}$  the force is  $e\vec{v}_{\perp} \times \vec{B}$  at right angles to

$\vec{v}$ , since the acceleration at right angles to  $\vec{v}$  is  $v_{\perp}^2 / \rho$ , where  $\rho$  is radius of curvature of the projection of the path on to a plane perpendicular to  $\vec{B}$ . It follows that

$$p = \frac{mv_{\perp}}{eB}, \quad (11)$$

which is constant. Of course, (11) is just a special case of the non-relativistic form of (4), with  $p_p \sin^2 \theta = p, v \sin \theta = v_{\perp}$ .

The general motion is therefore an arbitrary constant velocity along  $\vec{B}$ , superposed on circular motion perpendicular to  $\vec{B}$  described with constant angular velocity

$$\Omega = eB/m. \quad (12)$$

It is readily checked that a positively charged particle spirals in the sense of a left-handed screw about the magnetic field direction, a negatively charged particle in a right-handed sense.

The expression  $\Omega$  and  $\rho$  are commonly called the (angular) gyro (or Larmor) frequency and radius. In this non-

relativistic approximation  $\Omega$  is independent of the energy of the particle; for an electron in the earth's magnetic field of, say,  $B=0.05\text{mT}$  it is about  $8.8 \times 10^{-6} \text{ rad sec}^{-1}$ . But  $p$  is proportional to the square root of the energy; for a 10 eV electron in a field of  $B=0.05\text{mT}$  it is about 0.21 m.

If  $\vec{E}$  and  $\vec{B}$  are both present, and each is constant and uniform, the motion can be obtained in following way. Along  $\vec{B}$  there is constant acceleration  $eE_{\parallel}/m$ . Perpendicular to  $\vec{B}$ , the equation of motion (5) is

$$\vec{E}_{\perp} + \vec{u} \times \vec{B} = 0 \quad (13)$$

giving, for motion perpendicular to  $\vec{B}$ ,

$$\vec{u} = \frac{\vec{E} \times \vec{B}}{B^2} \quad (14)$$

In (13) it is convenient to single out the velocity  $\vec{u}$  explicitly by writing

$$\vec{v}_{\perp} = \vec{u} + \vec{v}'_{\perp} \quad (15)$$

say. The substitution of (16) into (13) then gives

$$m\vec{v}'_{\perp} = e\vec{v}'_{\perp} \times \vec{B} \quad (16)$$

and this equation for  $\vec{v}'_{\perp}$  is precisely what would obtain for  $\vec{v}_{\perp}$  in the case  $\vec{E} = 0$ .

### 3. Sources of low frequency magnetic field in medical therapy

Usually the above description of ion's movement is useful in medical therapy for visualization and optimization of parameters of medical apparatus. The low frequency magnetic field is provided by coils. A girdle coil is applied usually (fig. 1).

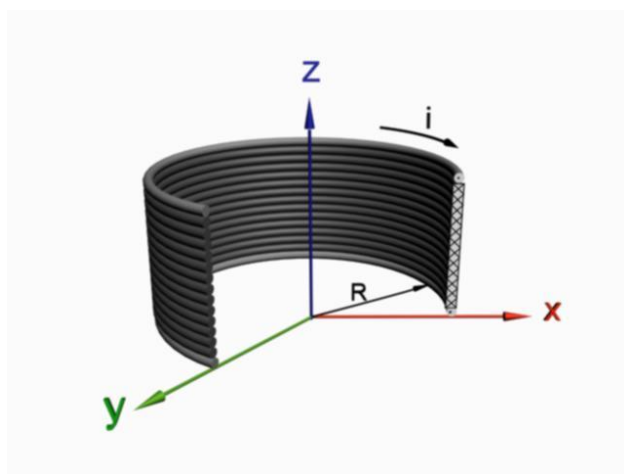


Fig. 1

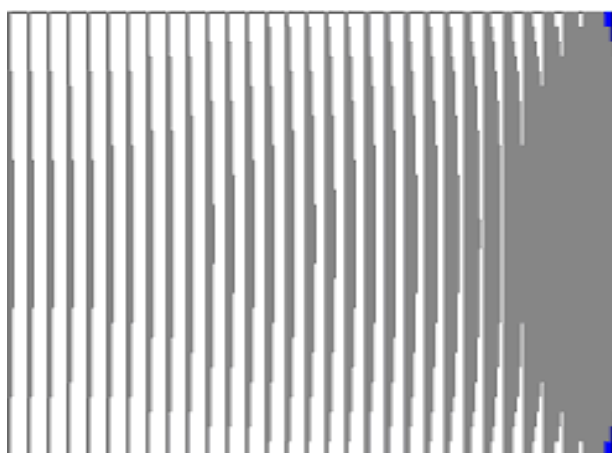


Fig. 2

The human body is in the girdle coil during the procedure. The space distribution of the module of magnetic induction in the coil can be seen on the fig. 2.

## Conclusion

The general motion can therefore be visualized simply by observing that the additional motion arising from the electric field  $\vec{E}$  is a constant acceleration  $eE_{\parallel}/m$  along  $\vec{B}$ , and a constant velocity perpendicular to both  $\vec{E}$  and  $\vec{B}$ , in the sense of a right-hand screw from  $\vec{E}$  to  $\vec{B}$ , of magnitude  $E_{\perp}/B$ .

## References

- [1]. [1.] D.Tz. Dimitrov, Computer Simulation of Space Configuration of Low Frequency Magnetic Field in Magnetotherapy, p.28-32, Journal "Electronics and Electrical Engineering", Lithuania, ISSN 1392-9631, 2005, -No.3(59).
- [2]. [2.] D.Tz. Dimitrov, Improving the Performance of Program Package for 3D Simulation of Low Frequency Magnetic Field in Medical Therapy, p.69-72, Journal "Electronics and Electrical Engineering", Lithuania, ISSN 1392-9631, 2007, No.1(73)
- [3]. [3.] D.Dimitrov, Visualization of a Low Frequency Magnetic Field, generated by Girdle Coil in Magnetotherapy, p.57-60, Journal "Electronics and Electrical Engineering", Lithuania, ISSN 1392-1215, 2007, -No.6(78), Fig.1.

# A MOTION OF IONS IN LIVE TISSUES UNDER INFLUENCE OF PERMANENT OR LOW FREQUENCY MAGNETIC FIELD

Boncho Angelov Bonchev

Technical Univesrsity of Sofia, Bulgaria

boncho71@abv.bg

## Abstract

*In this paper the case is presented in which there is no electric field, and in which the magnetic field is constant in time and everywhere has the same direction but not necessarily the same magnitude. A motion of ions in live tissues is observed..*

## 1. Introduction

Vector of electric field  $\vec{E} = 0$ , in rectangular Cartesian coordinates

$$\vec{B} = [0, 0, B(x, y)] \quad (1)$$

say, where the requirement  $\text{div } \vec{B} = 0$  ensures that  $B$  cannot depend on  $z$ . Unless  $\vec{B}$  is uniform  $\text{curl } \vec{B}$  does not vanish and there is a current density associated with the field.

## 2. Motion of ions in uni-directional magnetic field

Clearly now both  $v_x$  and  $v_y$  and so therefore is

$$v_{\perp} = \sqrt{(v_x^2 + v_y^2)}. \quad (2)$$

Furthermore, the projection of the path of the particle on the  $x$   $y$ -plane has radius of curvature

$$p(x, y) = \frac{mv_{\perp}}{eB}. \quad (3)$$

The curvature of the projected path is therefore a constant multiple of the magnetic induction. This fact can lead to a general appreciation of the nature of the path, and could be used for accurate computation.

To investigate the possibility of an analytic solution it is noted that the equation of motion are

$$\dot{v}_x = \Omega v_y, \quad \dot{v}_y = -\Omega v_x, \quad (4)$$

where the local gyro-frequency

$$\Omega = eB/m \quad (5)$$

is now a function of  $x$  and  $y$ , and only motion in the  $x$   $y$ -plane need be considered, with  $v_{\perp} = v$ .

Since equations (4) can be written

$$\frac{dv_x}{dy} = \Omega, \quad \frac{dv_y}{dx} = -\Omega. \quad (6)$$

it is clear that a solution by quadratures is possible if  $\Omega$  depends on only one of  $x$  or  $y$ . For if it be supposed that  $B$  is independent of  $y$ , say, the second equation of (5) gives

$$v_y = -\int \Omega(x) dx, \quad (7)$$

so that  $v_x = \sqrt{(v^2 - v_y^2)}$  is a known function of  $x$ , and  $t$  is given in terms of  $x$  by a further integration. Alternatively, the

path can be determined directly from the fact that

$$\frac{dy}{dx} = \frac{v_y}{v_x} = \frac{v_y}{\sqrt{(v^2 - v_y^2)}} \quad (7)$$

is a known function of  $x$ .

The same results follow readily from the Lagrangian formulation. The vector potential

$$\vec{A} = [0, A(x), 0]$$

corresponds to magnetic induction

$$\vec{B} = (0, 0, \frac{dA}{dx});$$

and Lagrangian formulation reads

$$L = \frac{1}{2}m(\dot{x}^2 + \dot{y}^2 + \dot{z}^2) + e\dot{y}A(x),$$

the  $y$ -coordinate is ignorable and corresponding Lagrange equation has first integral

$$\frac{\partial L}{\partial v_y} = 0,$$

that is

$$mv_y + eA = \text{const}, \quad (8)$$

which is the same as (6).

The example leading to the most elementary analytic details seems to be

$$\Omega = \frac{\text{const} \tan t}{x^2}. \quad (9)$$

For if  $mu = \text{const} \wedge ux_0 = \text{const}$  are chosen as the respective constants in (8) and (9), then these equations give

$$v_y = -u(1 - x_0/x), \quad (10)$$

from which (7) can evidently be integrated in terms of elementary functions. Without pursuing the details, the topology of the path can be ascertained from

the fact that  $v_y^2$  cannot exceed the constant  $v^2$ . Stated algebraically

$$(v^2 - u^2) \left( x + \frac{ux_0}{v-u} \right) \left( x - \frac{ux_0}{v+u} \right) \geq 0. \quad (11)$$

Since (9) is symmetric in  $x$ , and the particle cannot cross the plane  $x=0$ , there is no loss of generality in confining attention to positive values of  $x$ . let it also be assumed that  $ux_0 > 0$  corresponding to a magnetic field in the positive  $z$ -direction. Then if  $|u| < v$ , (11) shows that the path goes to infinity and that

$$x > \frac{ux_0}{v+u}; \quad (19)$$

if also  $u > 0$  (implying  $x_0 > 0$ ) then (19) is less than  $x_0$ , the value of  $x$  for which  $v_y$  vanishes. If  $|u| > v$ ,  $u$  must be positive, and the particle is confined to the range

$$\frac{ux_0}{u+v} < x < \frac{ux_0}{u-v}; \quad (20)$$

this range contains  $x=x_0$ , where  $v_y$  vanishes.

Another comparatively simple example of some interest is that in which the magnetic field varies linearly with  $x$ . If, say,

$$\Omega = \frac{2|u|}{x_0^2} x, \quad (21)$$

Then (6) can be written

$$v_y = u - \frac{|u|}{x_0^2} x^2, \quad (15)$$

where  $u$  is an arbitrary constant and the constant  $x_0$  can be taken as positive. The solution of (7) can be expressed in terms of elliptic integrals, but again the general picture is most easily obtained

from the fact that  $v_y^2$  cannot exceed  $v^2$ . For this now reads

$$(v^2 - u^2) \left[ 1 + \frac{|u|x^2}{(v-u)x_0^2} \right] \left[ 1 - \frac{|u|x^2}{(v+u)x_0^2} \right] \geq 0, \quad (16)$$

which shows that three cases can be distinguished as follows. If  $|u| < v$ , then

$$x^2 \leq \frac{v+u}{|u|} x_0^2 \quad (17)$$

and the particle is confined between the two planes  $x = \pm \sqrt{[(v+u)/|u|]} x_0$ ; if, also,  $u > 0$ , the range of  $x$  includes  $\pm x_0$ , the values of  $x$  for which  $v_y$  vanishes.

Suppose, now, that instead of being a function of  $x$  only the field is a function only of  $r = \sqrt{(x^2 + y^2)}$ , that is, there is cylindrical symmetry about the  $z$ -axis. To conclude this sub-section it is noted that this is a second case where solution by quadratures is possible, and a specific example is considered.

In cylindrical polar coordinates  $r, \theta, z$ , with

$$\vec{B} = [0, 0, B(r)] , \quad (22)$$

the equation of motion in the  $\theta$ -direction is

$$\frac{1}{r} \frac{d}{dt} (r^3 \dot{\theta}) = -\Omega \dot{r} ,$$

giving

$$v_\theta = r\dot{\theta} = -\frac{1}{r} \int r\Omega(r) dr . \quad (23)$$

Then

$$\dot{r}^2 = v_r^2 = v^2 - v_\theta^2$$

is a known function of  $r$ , and  $t$  is given in terms of  $r$  by a further integration. Or again, the equation of the path is given directly by integrating

$$r \frac{d\theta}{dr} = \frac{v_0}{\sqrt{v^2 - v_\theta^2}} . \quad (24)$$

For the Lagrangian formulation the vector potential in cylindrical polar co-ordinates can be taken as

$$\vec{A} = [0, A(r), 0] , \quad (25)$$

where

$$B = \frac{1}{r} \frac{d}{dr} (rA) . \quad (26)$$

Then

$$L = \frac{1}{2} m (\dot{r}^2 + r^2 \dot{\theta}^2 + \dot{z}^2) + eA(r) r \dot{\theta} ,$$

so that  $\theta$  is ignorable and

$$\frac{\partial L}{\partial \theta} = \text{const} ,$$

which is readily seen to be identical with (23).

An example for which the analytic details are elementary is  $A = \text{constant}$ . If the constant is written as

$$\vec{A} = \frac{mu}{e} = \text{const} , \text{ then}$$

$$\Omega = u/r , \quad (27)$$

and (23) gives

$$v_\theta = -u(1 - r_0/r) , \quad (28)$$

where  $u$  can be taken positive, but  $r_0$  may be positive or negative. The analysis is evidently virtually the same as that in the first example considered in this sub-section, which was based on equation (10). The requirement that  $v_\theta^2$  cannot exceed the constant  $v^2$  shows that there are three types of path.

### 3. Application of low frequency magnetic field in medicine

The motions of ions under permanent or low frequency magnetic field is used often in medicine for treatment of knee. (fig. 1). The low frequency mag-

netic field in this case is provided by two inductors.

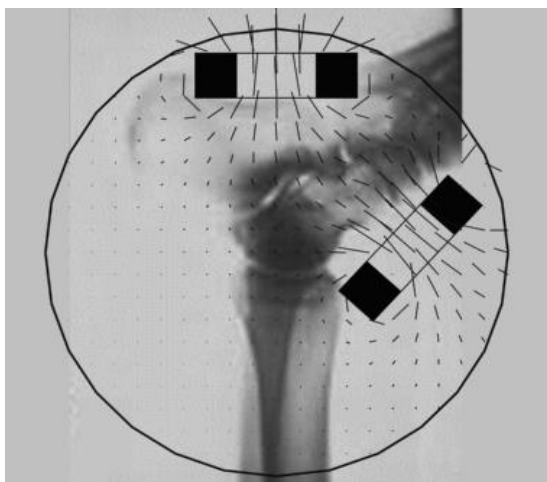


**Fig. 1**

## Conclusion

The conclusion exemplifies the main results and the fundamental ideas presented in the paper. It should allow to fully recognize the goals of the presentation. In the conclusion, papers concerning educational activities should include an opening to the education community.

## References

- [1]. <http://mania.cats.rwth-aachen.de/developer/tools/cfd>
- [2]. <http://www.sci.utah.edu/bisti/static>
- [3]. <http://www.sci.utah.edu/ncrr/overview/background.html>
- [4]. D. Tz. Dimitrov, Computer Simulation of Space Configuration of Low Frequency Magnetic Field in Magnetotherapy, p.28-32, Journal "Electronics and Electrical Engineering", Lithuania, ISSN 1392-9631, 2005, -No.3(59),
- [5]. D.Tz. Dimitrov, Improving the Performance of Program Package for 3D Simulation of Low Frequency Magnetic Field in Medical Therapy, p.69-72, Journal "Electronics and Electrical Engineering", Lithuania, ISSN 1392-9631, 2007, No.1(73)
- [6]. D.Dimitrov, Visualization of a Low Frequency Magnetic Field, generated by Girdle Coil in Magnetotherapy, p.57-60, Journal "Electronics and Electrical Engineering", Lithuania, ISSN 1392-1215, 2007, -No.6(78)

# A SIMULATOR FOR WiMAX NETWORKS

Valentin Panchev Hristov

South- West University- Blagoevgrad,  
66 Ivan Mihajlov Street, Blagoevgrad- Bulgaria  
Phone (+359)738889132; E-mail v\_hristov@aix.swu.bg.

**Keywords:** polling system, simulator, wireless networks

Broadband wireless access (BWA)  
base station(BS)  
subscriber stations (SSs)

The present paper aims at presenting the process of designing the simulation model of 802.16 Networks and Investigation of Bandwidth Request Mechanisms under Point-to-Multipoint Mode.

In response to BWA need, the IEEE 802 committee set up a working group to develop such standard- IEEE 802.16. Later, an industrial association, the Worldwide Interoperability for Microwave Access (WiMAX) Forum, was formed to promote the 802.16 standard.

WiMAX specifies interoperable air interfaces from 2 to 66 GHz with a common medium access control – MAC layer (fig.1).

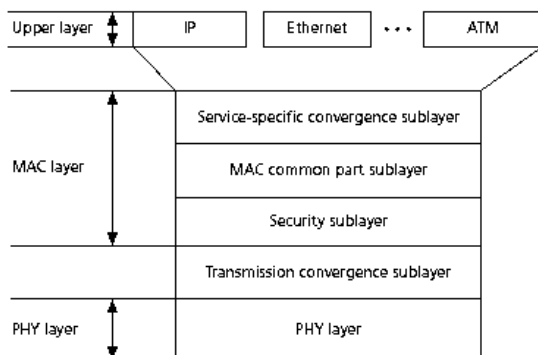


Fig. 1

The 802.16 WiMAX air interface supports two operational modes: a manda-

tory point to multipoint- PMP mode and an optional mesh mode. In PMP mode, a centralized BS controls all communications among the SSs and the BS, whereas in the mesh mode, SSs can also serve as routers by cooperative access control in a distributed manner.

## WIMAX AND BW-REQ MECHANISMS

Under the PMP architecture, all transmissions between the BS and SSs are coordinated by the BS. The TDMA/TDD frame structure is illustrated in Fig. 2; it consists of a downlink subframe for transmission from the BS to SSs and an uplink subframe for transmissions in the reverse direction. The Tx/Rx transition gap (TTG) and the Rx/Tx transition gap (RTG) are specified between the downlink and uplink subframes, and between the uplink and following downlink subframes in the next frame duration to allow SS terminals to turn around from reception to transmission and vice versa. In the downlink subframe, both the downlink MAP (DL-MAP) and uplink MAP (UL-MAP) messages are transmitted, which comprise the bandwidth allocations for data transmission in both downlink and uplink directions, respectively.

Moreover, the lengths of uplink and downlink subframes are determined dynamically by the BS and are broadcast to the SSs through UL-MAP and DL-MAP messages at the beginning of



each frame. Therefore, each SS knows when and how long to receive data from and transmit data to BS. The bandwidth allocated to each direction can be tuned dynamically to match the traffic in the corresponding direction. This means that if an SS needs some amount of bandwidth, it makes a reservation with the BS by sending a

request. On accepting the request from an SS, the BS scheduler should determine and grant it a transmission opportunity in time slots by using some scheduling algorithms, which should take into account the requirements from all authorized SSs and the available channel resources.

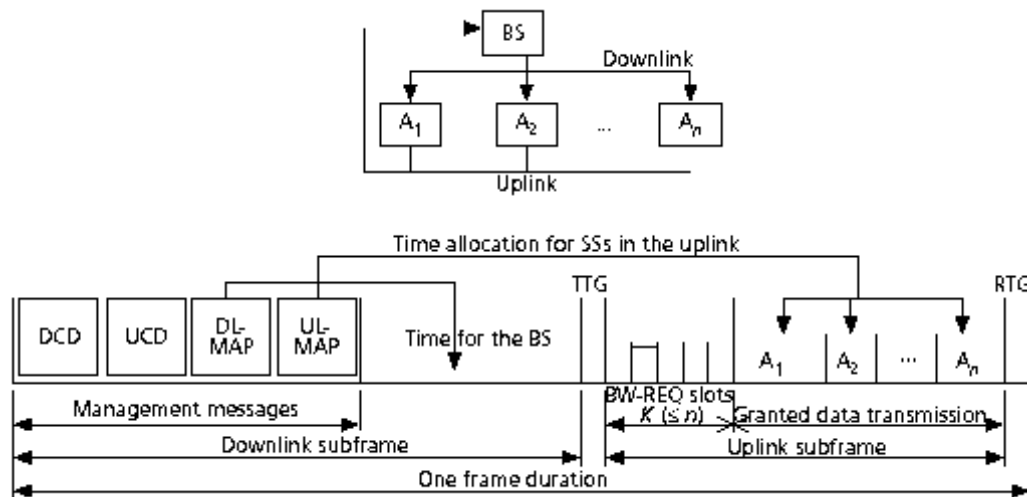


Fig. 2

Two main methods are suggested in the WiMAX standard to offer transmission opportunities for SSs to send their bandwidth request (BW-REQ) messages: centralized polling and contention-based random access. In the first case each SS station is only allowed to send its request when it is polled by the BS.

### MODELING POLLING-BASED BW-REQ MECHANISMS

No specific polling algorithms are defined in the standard. The following simple round-robin polling scheme is considered for the analysis: Each of  $K$  slots is assigned equally to all of the  $n$  stations in the system. In most cases,  $n$  is larger than  $K$ .

If  $K > n$ , the system will be very lightly loaded, and there are more slots than the total number of SSs in the system. All the SSs will be able to send BW-REQs within a frame. The Maximum

delay can be easily determined, i.e., one frame duration.

The Q-scheme includes  $N$  queues, which is serviced by one server, and a synchronizing process switching between polling and vacation periods. Compared to model described here, the Contention-Free Period (CFP) and Contention Period (CP) correspond to the polling period and vacation period, respectively. The ON-OFF model is assumed to be the source for each of the  $N$  queues.

On MAC layer is developing the following processes: The queues filled with a continuous bit stream when the source is in the ON state; The synchronizing process schedules transmission opportunities among all queues during polling periods; A vacation can occur at arbitrary points within a polling cycle, even it can occur multiple times within one polling cycle.

The initial conditions for wireless network are given bellow:

- Number of sources-  $N$ ;
- Superframe length - $T_s$ ;
- Minimum fraction allocated to vacation period-  $\theta$ ;
- Maximum vacation stretch-  $V_{Smax}$  ;
- Parameters for CP stretch;
- SS rate;
- Service rate.

The modelling process aims at getting the following results, when preliminaries given at hand simulation conditions are available: Maximum and average time for delay from the access (the time from coming of BW-REQs till their transmitting).

### PERFORMANCE ANALYSIS OF BW-REQ MECHANISMS

In this section we investigate the polling BW-REQ mechanism, by using the proposed model above under error-

free channel condition. For the WiMAX PHY layer, 256- carrier OFDM and 5 MHz bandwidth are chosen. The frame duration is set to 2.5 ms. In the following plots the arrival rates  $\{1/1000, 1/500, 1/250, 1/167, 1/125\}$  are chosen and axe is denoted by  $\square \square$

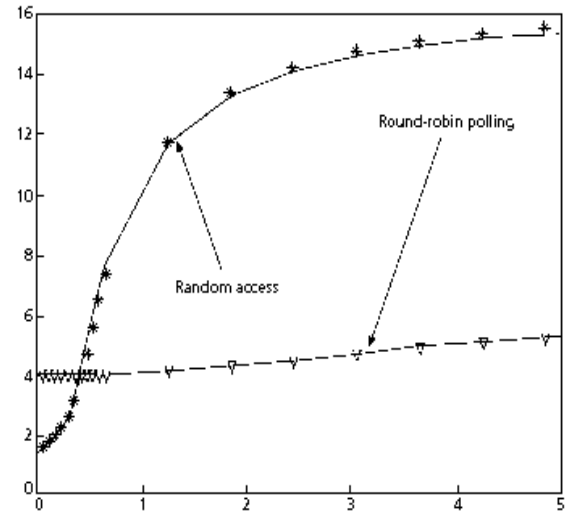


Fig. 3

# ZIGBEE BIOTELEMETRY APPLICATION

M. Penhaker, J. Floder, M. Cerny, M. Rosulek

VSB Technical University of Ostrava, Faculty of Electrical Engineering and Computer Science, Department Measurement and Control, Biomedical engineering laboratory

17.listopadu 15, 708 33 Ostrava – Poruba, Czech republic  
T.+420597323510; F.+420597323138;  
E.{marek.penhaker; jan.floder; martin.cerny}@vsb.cz

## Abstract

*The mobile telemetry system of biological parameters serves for reading and wireless data transfer of measured values of selected biological parameters to an outlying computer.*

*This article is focused on ZigBee networks solution used in this project and using of dry textile electrodes for ECG measurement.*

*ZigBee communication is not so often used in biotelemetry branch even if it has many advantages contrary to other commercial wireless personal networks solutions. There are used two different hardware ZigBee solutions.*

*ECG measurement is realized by designed bio amplifier. Measured data are sampled and filtered in ZigBee module. Dry Textile electrodes are based on polyanilin. These electrodes were tested in our laboratory and used in this telemetry project*

## 1. Introduction

In the present time the health telemetry systems forge an integral part of our everyday lives. Comparatively in the near future embedded systems will ward over our lives and health.

It was created function prototype of wireless biomedical (and any other) data transmission and data analysis sys-

tem. System transfers data about race vehicle drivers condition and some additional data about ride. These drivers' signals are collected: SpO2, pulse, ECG, and body temperature. Besides these signals data about acceleration of vehicle in X and Y axis (front-back, left-right) and air temperature is measured.

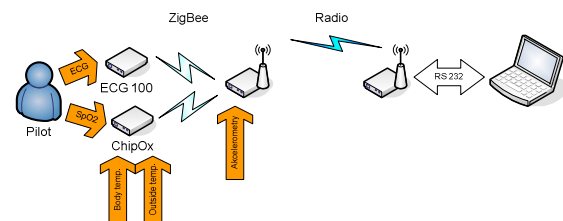


Figure 1. Designed telemetry system

There is realized bipolar one lead ECG measurement using designed bio amplifier. There is used special new type of textile electrodes, which were designed and tested in our laboratory with cooperation of Czech Academy of science.

The SpO2, body and outside temperature is measured by OEM SpO2 module ChipOx. These measured biomedical data are transmitted by ZigBee technology to module, which provides next data transmission to remote PC.

For data transmission between this module and remote PC are used radio modems. Transmitted data are in PC visualized and saved for next analysis.

## 2. Materials and methods

Data transmission is ZigBee based. ZigBee is a standard for wireless data transmission. It is based on the IEEE802.15.4 standard for WPANs (wireless personal area networks). It is aimed to applications where extended battery life ( $15 \div 40$  mA when transmitting – depends on chip producer) is needed and only low data rate (in kbps) is required. Bands available for ZigBee are 868MHz and 2.4GHz (Europe). Devices available are either modem like when they only retransmit data they receive (XBee) or equipped by programmable MCU where user can create own applications.

### 2.1. PAN4551/4555

SIP PAN4551 is based on the Freescale's first generation ZigBee transceiver MC13193 and 8-bit MCU. PAN4555 is based on 2nd generation Freescale SiC MC13213. Both two are fully programmable and with full support for the SimpleMAC and the 802.15.4MAC. Data transmission band is placed in 2.4 GHz and divided into 16 channels. Power consumption is about  $28 \div 40$  mA during transmission (receive or send). It predetermines it to be battery powered.

### 2.2. XBee

The XBee/XBee-Pro is MaxStream's modem based on the the ZigBee standard. Unlike PAN4551/4555, XBee is not fully programmable. Its idea is to be a wireless UART replacement or an universal ZigBee transmitter (commanded by some control device) participating in the 802.15.4 networks.

### 2.3. Pulse oximetry

Pletysmograph OEM module ChipOX measures the non-invasive saturation

by oxygen ( $SpO_2$ ), plethysmogram, pulse rate, body temperature and temperature of surroundings.

## 3. ECG measurement

### 3.1. ECG electrode treatment

A great problem occurs at ECG measurement. The medical instrument should be transportable and that's why the electrodes has to be part to not to manipulation illimitability. The problem rises how to create the electrodes which can by only put on the skin and not to be stickered by conducting stick or gel (dry electrode). Resulting this is clear that for constructing kind of the electrode should be no metal and gel. For the construction of this kind electrode the same principles were used as in common electrode. So the interface skin - electrolyte (gel) – metal. Instead electrolyte there was used aterial referred to as conducting polymer (Figure 2).

Charge transmission occurs with the help of alternating structure single bond and double bond and by the charge carrier furred similar to dosed operation.



**Figure 2.** Thin film of polyanilinu with thickness 100nm on lab dish

From that reason the polyamide is suitable matter for making dry bio potential electrode.

Conducting polymers are composed of long repeated constitutional group of chain. Common polymers like polyety-

len or polyvinylchloride are non-conducting and they are usually use as an insulating material. There has however been group of polymers which chemically conducting is. Examples include polyacetylene, polypyrrol, polythiofen, polyfenilen or poly (p-fenylen-vinilen).

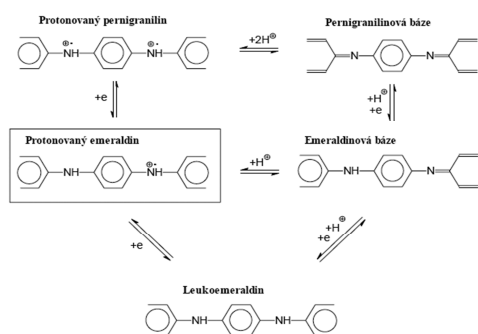


**Figure 3.** Forms of polyaniline

Their conductivity is  $4 \text{ S.cm}^{-1}$  is sufficient because they are settled in thin film form with thickness 100nm.

A production this type of electrode takes apx. 15 minutes and there is also a need for another 12 hours of desiccation. The production is very cheap and easy to attach for single use. For manufacturing the electrodes we can use it with advantages that weren't registered any toxic or irritable character. We can qualify it as harmless. The other advantage is to utilization of the material can be manufacture electrode on any matter to resisted acidic medium. Textile materials are fine to use it for electrodes and that is why the electrodes on Velcro fastener were made. Both side of Velcro fastener is covered by polyanilin.

### 3.1.2. ECG electrode tests

During a testing on three leads ECG were found of that manufactured electrodes are well usability. The measurement were done on ECG being short (pectoral) bipolar placement gained by bioamplifier g.BSamp, 16 channels from

g.tec medical engineering GmbH and digitalized by A/D card NI DAQPad-6052E. The results were measured with common stick electrodes on computer at the same time. The result was mathematically compared and results were very good.

Electrodes were mounted on flexible t-shirt made on elastics fiber. Adherence pressure was too small to well connect skin with electrode and that is why the great interference voltage arose. Consequently were added the elastic belt on thoraxes to improve adherence pressure of the electrodes Figure 5.



**Figure 4.** Distribution of ECG electrodes on the T- shirt

Out of signal record we can clearly see the changing level of a signal same direction constituent and also extend of a signals amplitude which is very interesting. This could be explained by the person who breathed in the moment and the tissue capacity under the electrode reduced. The signal could get into smaller tissue capacity. On the next picture there is a signals amplitude life cycle signified and its same direction component Figure 6. In the same time you can see low-frequency breathing caused by impedance changes.

## 4. Network design

IEEE 802.15.4 standard network was chosen because of cooperation with

XBee. XBee can participate in 802.15.4 star networks as an end device or a coordinator or in peer-to-peer networks. Because the structure of communication is mostly from data-gathering nodes to the storage and analysis device (computer in this case), star network was chosen (one PAN coordinator and two end devices). But in fact the peer-to-peer network can be used too.

Parameters of the network are: non-beacon, no security, acknowledge, logical channel is one of 13-23 selected by PAN on its startup (the one with the least energy / the preset one). Addressing is 16-bit in default but the coordinator handles also 64-bit (device serial number). Coordinator's PAN ID is preset.

The coordinator allows end device association by comparing with its table of granted devices (table of serial numbers) non-granted devices is refused automatically. End devices have the same table of granted coordinators so it cannot happen that device will associate to different coordinator.

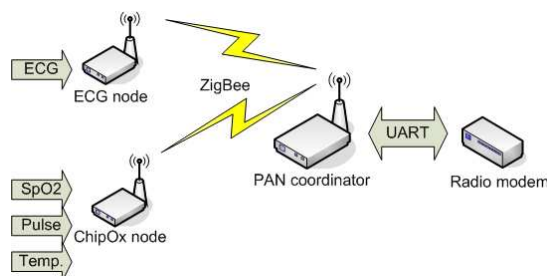


**Figure 5.** ZigBee Network Topology

Main data flow is from the ECG node (it has to transmit huge amount of sampled and filtered analog data) it transmits approximately every 100ms and total amount is about 600B per second. Second node (ChipOx) with XBee sends significantly lower amount of data - at about 200 Bytes per second.

The PAN coordinator translates all the data and retransmits them to the PC.

## 5. Network realization

As can be see from network structure, network consists of three nodes. The first one is the PAN coordinator.

The PAN coordinator used is PAN4551. It was necessary to use PAN4551 because the coordinator has to handle communication with the PC initialization/de-initialization of end devices translate incoming packets, recognize devices. It is created as FFD without support for beacons networks and without security. Program part is modified Freescale Beekit's output. Packets send to a PC have the same format as in the past project – original visualization can be used.

### 5.1. ChipOx Node

ChipOx node is based on the XBee. XBee here has the only obligation – to transmit incoming coded data from the ChipOx and send them to the coordinator. Communication from the coordinator to this device is direct because ChipOx does not know periodical polling (without sleep).

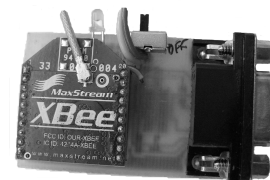


**Figure 6.** ChipOx node PCB

### 5.2. ECG node

ECG node uses PAN4551. PAN4551 is advantageous because it has 10bit ADC and can be programmed to buffer data and do some filtration. It samples data every 1ms and filters them before sending (or samples data every 2ms but without filtering). The only suitable filter for a biomedical signal and that sampling speed (combined with 8-bit processor) is a FIR filter.

This FIR filter (Hamming window) is a low-pass filter with cutoff frequency 150Hz and cuts undesired high frequencies and is used to downsample data to the half frequency. This filter had to be quantized to the 16bit binary unsigned fixed-point with range of 0 to  $\sim 1$  ( $\rightarrow$  shifted 16bits right). This was the only way for the 8-bit architecture to handle calculations at so high frequencies.

Filter calculations can be divided in 8bit multiplications and 16bit additions (8bit and carry). To speed up calculations some additions can be removed (results in calculation error – but maximally error of 2). Whole filtering consumes from at about 10% of MCU time (11th order filter and downsampling) to 5% (7th order filter and downsampling) – for MCU bus frequency of 16MHz.

The data is buffered for 0.4 second. Filtering was used due to “bottleneck” of the radio-modem

## Conclusions

The biomedical data transmission system was successfully created using IEEE 802.15.4 standard cooperating with XBee.

There we used OEM modules for pulse oxymetry measurement and designed bioamplifiers for ECG measurement. There were used ECG dry textile electrodes.

Designed telemetry system were used for monitoring base life function of pilot of race vehicle powered by hydrogen

From so far acquired results of experiments we are able to observe that polyamides are suitable material for bio-potential electrodes construction. But there is a need now to concentrate on measuring and monitoring of parameters long term firmness both an electro-technical and a mechanical.

## Acknowledgments

The work and the contribution were supported by the project Grant Agency of Czech Republic – GACR 102/05/0467 Architectures of embedded system networks and grant GACR 102/05/H525 The Postgraduate Study Rationalization at Faculty of Electrical Engineering and Computer Science VSB-TU Ostrava. This work was partially supported by the faculty internal project Biomedical engineering systems II.

Many thanks to Mr. Jaroslav Stejskal PhD. and Mrs. Elene Konjusenko from Academy of science, Institution of macromolecular chemistry in Prague and to Prof. Ing. Kamil Wichterle, DrSc from VSB – TU Ostrava.

## References

- [1] Bronzino J.D. et al. The biomedical engineering handbook (Book style), CRC Press, Boca Raton, 1995
- [2] Gardner J. W. Microsensors: Principles and Applications (Book style), John Wiley & Sons Ltd, 1999
- [3] Ohba R. Intelligent sensor technology (Book style), John Wiley & Sons Ltd, 1992
- [4] Penhaker M., Imramovský M., Tiefenbach P. Kobza F. Lékařské diagnostické přístroje (Book style), VŠB-TU Ostrava, 2004
- [5] <http://butler.cc.tut.fi/%7Emalmivuo/bem/book/index.htm#contents>
- [6] <http://www.vivometrics.com/>
- [7] Mrázová, J. (2005). Bio-signals classification into groups, In TRANSCOM Section
- [8] Mrázová, J. (2005). Rozdelenie biosignálov podľa rôznych kritérií, In Trendy v BMI 2005, Žilina
- [9] Panasonic: PAN4551, PAN4555 datasheets, [www.pedeu.panasonic.de](http://www.pedeu.panasonic.de)

Application of Z-Transform for calculating  
locations and amplitudes of extrema:  
the case of *sinc* and related functions

Jean Le Bihan

*Ecole Nationale d'Ingénieurs de Brest, RESO, CS 73862, 29238 BREST cedex 3, France*  
*Tel. +33 298 05 66 35, Fax +33 298 05 66 06, E-mail Jean.Le\_Bihan@enib.fr*



**Abstract.** Expressions of the form  $\text{sinc } x$ ,  $(\sin x/x)^r$  or  $(\sin^2 x)/x$  may occur in engineering problems, for instance in signal processing or communications. Using Z-Transform techniques, it can be shown that the locations and amplitudes of the extrema of the sinc function, when expressed under the form of series expansions, can be calculated very fast through a straightforward recursion formula. Moreover, very simple accurate algebraic expressions can be derived for evaluating these locations and amplitudes. Using a similar approach, recursion formulae and algebraic expressions can be obtained for the locations and amplitudes of the extrema of  $(\sin x/x)^r$ , and of those of  $(\sin^2 x)/x$  as well.

## I. INTRODUCTION

The  $\sin x/x$  function (Fig. 1a) plays a key role in the fields of signal processing and communications [1, 2], so its properties have been extensively studied. Its Fourier transform, the rectangular function, is also widely used. On the other hand, the convolution operator and its counterpart regarding the Fourier Transform, the product operator, are of great importance. This paper presents the computation of the extrema of the function  $(\sin x/x)^r$ , where  $r$  is a positive integer. This function can be viewed as the result of the Fourier transform of a product of  $r$  identical rectangular pulses. A useful case is that of the function  $(\sin x/x)^2$  (Fig. 1b) which represents the Fourier transform of a triangular function.

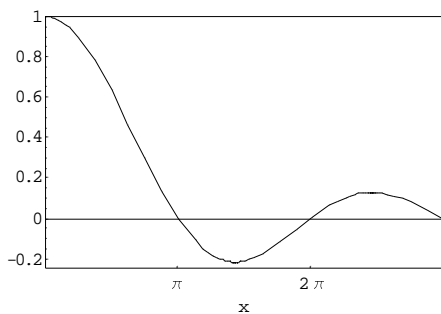


Fig. 1a.  $\sin x/x$

For example, a window is frequently used in the time domain to limit the duration of a signal before calculating its Discrete Fourier Transform. Many kinds of windows can be considered. Generally, the window is chosen with

a smooth return to zero at its ends, in order to avoid discontinuity between two successive replicas of the periodized signal. This leads to enhanced properties of its Discrete Fourier Transform. The well known rectangular window does not satisfy this criterion, but its multiple convolutions do. The smoothness at the ends of the so-called polynomial windows [3] increases with the number of convolutions. So the frequential properties of a polynomial window, which corresponds to the convolution of  $r$  rectangular windows of duration  $T$ , are given by its Fourier Transform proportional to  $(\sin x/x)^r$ , with  $x = \pi T f$ . In particular, the triangular window and the parabolic window are relative to  $r = 2$  and  $r = 3$ , respectively.

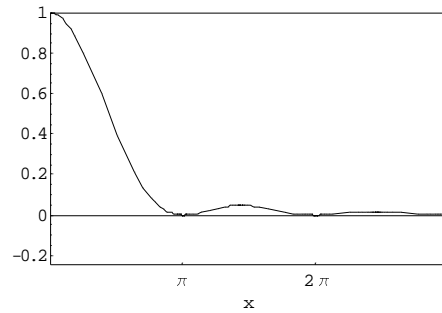


Fig. 1b.  $(\sin x/x)^2$

The  $(\sin x/x)^r$  function may appear in other applications, for instance when studying random processes [4]. In the case of a simple random binary wave, with pulses of amplitude  $+A$  and  $-A$  and duration  $T$ , the autocorrelation function has a triangular waveform and the expression of the power spectral density, is  $A^2 T (\sin x/x)^r$ , with  $x = \pi T f$ .

In this paper, it will also be presented the computation of the extrema of the function  $y = (\sin^2 x)/x$ , which can also be written  $y = \sin x (\sin x/x)$  (Fig. 2). Such an expression may be encountered in signal processing or communications problems, and also in other fields of physics or engineering.

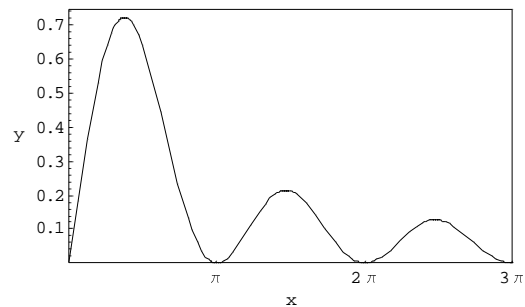


Fig. 2.  $y = (\sin^2 x)/x$

For example, if we consider the signal  $A(\Pi((t-\theta/2)/\theta) + \Pi((t+\theta/2)/\theta))$  (with  $\Pi(t) = 1$  if  $|t| \leq 1/2$  and 0 if  $|t| > 1/2$ ), i.e. the sum of two rectangular pulses symmetrical towards the origin (or the convolution of a rectangular pulse  $A\Pi(t/\theta)$  by two Dirac impulses  $\delta(t-\theta/2)$  and  $\delta(t+\theta/2)$  symmetrical towards the origin), its Fourier transform is expressed as follows :  $2jA\theta \sin^2(\pi f\theta)/(\pi f\theta)$ .

## II. EXTREMA OF $(\sin x/x)^r$

### II.1. Equation

It is clear that the zeros of the function  $(\sin x/x)^r$  are at  $\pm k\pi$  ( $k = 1, 2, \dots$ ) and the global maximum, which equals 1, is at  $x = 0$ . The minima of  $(\sin x/x)^r$  for an even  $r$  are at  $\pm k\pi$  ( $k = 1, 2, \dots$ ) and equal 0. But the local extrema  $(\sin x/x)^r$  for any  $r$  are not at  $\tilde{x}_m = \pm(2m+1)\pi/2$  ( $m = 1, 2, \dots$ ). Their locations  $x_m$  are, for all  $r$ , the solutions of

$$x = \tan x \quad (1)$$

Once the  $x_m$  obtained, the extrema amplitudes  $y_{m,r}$  can be deduced from

$$y_{m,r} = \cos^r x_m \quad (2)$$

or  $y_{m,r} = (-1)^{mr}(1 + x_m^2)^{-r/2}$ .

In some applications, accurate determination of the extrema is needed [5]. In [5], a closed-form approximation and a recursion formula were proposed to determine the locations of the local extrema, with a good accuracy. In a more recent paper [6], methods were presented and used for the computation of both the locations and the amplitudes of the  $\sin x/x$  function's extrema. Especially, series expansions were introduced to express the extrema locations and amplitudes, as well as simple algebraic approximations, allowing to reach an excellent accuracy. These results were extended to the function  $(\sin x/x)^r$  in [7]. In particular, it was shown how to compute the coefficients of the  $y_{m,r}$  series expansions and give approximate algebraic expressions for  $y_{m,r}$ .

### II.2. Locations of the extrema

#### II.2.1. Series expansion

Let us denote  $e_m = \tilde{x}_m - x_m$  the difference between each exact extremum location  $x_m$

and its nearest odd multiple of  $\pi/2$ , i.e.  $\tilde{x}_m$ . Then let us write  $e_m$  under the form of a series expansion in successive powers of  $(\tilde{x}_m)^{-1}$ :  $e_m = \sum_{n=0}^{+\infty} e_m^n (\tilde{x}_m)^{-n}$ . Therefrom the expansion coefficients of the extrema locations  $x_m = \sum_{n=-1}^{+\infty} x_m^n (\tilde{x}_m)^{-n}$  can be immediately deduced :  $x_m^{-1} = \tilde{x}_m$ ,  $x_m^n = -e_m^n$  ( $n \geq 0$ ).

We show now that using basic z-Transform techniques allows to derive the coefficients of the expansions. Changing  $\tilde{x}_m$  into  $z_m$  for this purpose and leaving out the index  $m$  for the coefficients are independent of  $m$ , eqn 1 takes the form

$$\tan e = \frac{1}{z - e} \quad (3)$$

The first derivative can be expressed as

$$\frac{de}{dz} = -\frac{1}{(z - e)^2} \quad (4)$$

A second derivation leads to

$$(z - e) \frac{d^2 e}{dz^2} - 2 \left( \frac{de}{dz} \right)^2 + 2 \frac{de}{dz} = 0 \quad (5)$$

If  $F(z)$  and  $G(z)$  denote the z-transforms of  $f_n$  and  $g_n$  respectively ( $f_n \rightarrow F(z)$  and  $G(z) \rightarrow g_n$ ), note the following inverse z-transforms :  $z^{-1}F(z) \leftarrow f_{n-1}$ ,  $-z \frac{dF(z)}{dz} \leftarrow n f_n$ ,  $F(z)G(z) \leftarrow \sum_{j=0}^n f_j g_{n-j} = \sum_{j=0}^n f_{n-j} g_j$ .

Interpreting eqn 5 by using basic z-Transform properties allows the straightforward computation of the expansion coefficients of  $e$  through the following relation (where  $n$  in  $e^n$  denotes an upper index)

$$e^n = \frac{1}{n(n-1)} \dots \sum_{j=1, j \text{ odd}}^{n-2} j(2n-j-1)e^j e^{n-j-1}, \quad (6)$$

$$n \geq 3, n \text{ odd}$$

$$e^n = 0, n \geq 0, n \text{ even}$$

with  $e^1 = 1$ . Therefore the expansion of  $x_m$  begins as follows

$$x_m = \tilde{x}_m - (\tilde{x}_m)^{-1} - \frac{2}{3}(\tilde{x}_m)^{-3} \dots - \frac{13}{15}(\tilde{x}_m)^{-5} - \frac{146}{105}(\tilde{x}_m)^{-7} - \dots \quad (7)$$

#### II.2.2. Algebraic approximation

By limiting this expansion, simple closed-form approximations are obtained for  $x_m$ . Table 1 shows the values obtained for  $x_1, x_2, x_3$  using the successive terms of the series expansion (the table starts with  $x_m \simeq \tilde{x}_m$  at rank

$p = 0$  ( $n = 2p - 1$ ). It can be observed for example that after only two ranks, the maximum relative error of the very simple algebraic approximation  $x_m \simeq \tilde{x}_m - (\tilde{x}_m)^{-1} - \frac{2}{3}(\tilde{x}_m)^{-3}$  is  $8.96 \times 10^{-5}$  and it occurs for  $m = 1$ . The relative error is less than  $3.86 \times 10^{-6}$  for the other values of  $m$ . This very simple formula gives results comparable to those of eqn 1 in [5].

Table 1. Successive values for  $x_1, x_2, x_3$ 

$p$	$x_1$	$x_2$	$x_3$
0	4.712388980	7.853981634	10.99557429
1	4.500182390	7.726657680	10.90462861
2	4.493811716	7.725281614	10.90412712
3	4.493438770	7.725252614	10.90412173
4	4.493411825	7.725251859	10.90412166
$\infty$	4.493409458	7.725251837	10.90412166

### II.3. Amplitudes of the extrema

#### II.3.1. Series expansion

Using the same approach as for the locations, the extrema themselves can be directly calculated. From eqn 1, their amplitudes are  $y_{m,r} = (-1)^{mr} \sin^r e_m$ . Assuming that  $y_{m,r}$  can be expanded under the form  $y_{m,r} = (-1)^{mr} \sum_{n=0}^{+\infty} y_{m,r}^n (\tilde{x}_m)^{-n}$ , and changing  $\tilde{x}_m$  into  $z_m$ , eqns 3 and 4 lead to the simple following equation ( $m$  is omitted as above)

$$-(z - e) \frac{d|y_r|}{dz} = r |y_r| \quad (8)$$

Interpreting eqn 8 by using basic z-Transform properties allows here the straightforward computation of the expansion coefficients of  $(-1)^{mr} y_{m,r}$  through the following relation (where  $n$  in  $y_r^n$  or  $e^n$  denotes an upper index)

$$y_{m,r}^n = \frac{1}{n-r} \sum_{j=r}^{n-1} j e^{n-j-1} y_r^j, \quad n > r, (n-r) \text{ even} \quad (9)$$

$$y_{m,r}^n = 0, n \geq 0, (n < r, (n-r) \text{ odd})$$

with  $y_{m,r}^r = 1$ . Therefore the expansion of  $y_{m,r}$  begins as follows, for  $r = 1$  and  $r = 2$  as examples

$$y_{m,1} = (-1)^m (\tilde{x}_m)^{-1} + \frac{1}{2}(\tilde{x}_m)^{-3} + \dots + \frac{13}{24}(\tilde{x}_m)^{-5} + \frac{61}{80}(\tilde{x}_m)^{-7} + \dots \quad (10)$$

$$y_{m,2} = (\tilde{x}_m)^{-2} + (\tilde{x}_m)^{-4} + \dots + \frac{4}{3}(\tilde{x}_m)^{-6} + \frac{31}{15}(\tilde{x}_m)^{-8} + \dots \quad (11)$$

#### III.3.2. Algebraic approximation

By limiting this expansion, simple closed-form approximations are obtained for  $y_{m,r}$ .

Table 2 shows the values obtained for  $y_1^1, y_2^1, y_3^1$  using the successive terms of the series expansion (the table starts with  $y_{m,1} \simeq (-1)^m (\tilde{x}_m)^{-2}$  at rank  $p = 0$  ( $n = 2p + 1$ )). It can be observed for example that after only two ranks, the maximum relative error of the simple algebraic approximation  $y_{m,1} \simeq (-1)^m [(\tilde{x}_m)^{-1} + \frac{1}{2}(\tilde{x}_m)^{-3} + \frac{13}{24}(\tilde{x}_m)^{-5}]$  is  $7.34 \times 10^{-5}$  and it occurs for  $m = 1$ . The relative error is less than  $3.31 \times 10^{-6}$  for the other values of  $m$ .

Table 2. Successive values for  $y_1^1, y_2^1, y_3^1$ 

$p$	$y_1^1$	$y_2^1$	$y_3^1$
0	-0.2122065908	0.1273239545	-0.09094568177
1	-0.2169845959	0.1283560036	-0.09132179296
2	-0.2172176874	0.1283741288	-0.09132516305
3	-0.2172324632	0.1283745424	-0.09132520229
4	-0.2172335359	0.1283745532	-0.09132520282
$\infty$	-0.2172336282	0.1283745535	-0.09132520282

Table 3 shows the values obtained for  $y_1^2, y_2^2, y_3^2$  using the successive terms of the series expansion (the table starts with  $y_{m,2} \simeq (\tilde{x}_m)^{-2}$  at rank  $p = 0$  ( $n = 2p + 2$ )). It can be observed for example that after only two ranks, the maximum relative error of the simple algebraic approximation  $y_{m,2} \simeq (\tilde{x}_m)^{-2} + (\tilde{x}_m)^{-4} + \frac{4}{3}(\tilde{x}_m)^{-6}$  is  $1.95 \times 10^{-4}$  and it occurs for  $m = 1$ . The relative error is less than  $8.91 \times 10^{-6}$  for the other values of  $m$ .

Table 3. Successive values for  $y_1^2, y_2^2, y_3^2$ 

$p$	$y_1^2$	$y_2^2$	$y_3^2$
0	0.04503163717	0.01621138938	0.008271117032
1	0.04705948552	0.01647419853	0.008339528409
2	0.04718124196	0.01647987920	0.008340282860
3	0.04718974044	0.01648002194	0.008340292533
4	0.04719039121	0.01648002587	0.008340292669
$\infty$	0.04719044923	0.01648002599	0.008340292671

## III. EXTREMA OF $(\sin^2 x)/x$

### III.1. Equation

It is clear that the zeros of the function  $y$  are at  $\pm k\pi$  ( $k = 0, 1, 2, \dots$ ). But the extrema are not at  $\tilde{x}_m = \pm(2m + 1)\pi/2$  ( $m = 1, 2, \dots$ ). Their locations  $x_m$  are the solutions of

$$\tan x = 2x \quad (12)$$

Once the  $x_m$  obtained, the extrema amplitudes  $y_m$  can be deduced from

$$y_m = \frac{4x_m}{1 + 4x_m^2} \quad (13)$$

In some applications, accurate determination of the extrema locations and amplitudes may be needed, as for the  $\sin x/x$  function [5]. In [6], methods were presented for the computation of both the locations and the amplitudes of the  $\sin x/x$  function's extrema. Especially, series expansions were introduced to express the extrema locations and amplitudes, as well as simple algebraic approximations, allowing to reach an excellent accuracy. In this paper, we exploit similar ideas to obtain analog results for the function  $(\sin^2 x)/x$ . We show how to compute the coefficients of the  $x_m$  and  $y_m$  series expansions and give approximate algebraic expressions for  $x_m$  and  $y_m$ .

As the function  $y$  is symmetric towards the origin, we will consider  $x \geq 0$  in the following.

### III.2. Locations of the extrema

#### III.2.1. Series expansion

Let us denote  $e_m = \tilde{x}_m - x_m$  the difference between each exact extremum location  $x_m$  and its nearest odd multiple of  $\pi/2$ , i.e.  $\tilde{x}_m$ . Then let us write  $e_m$  under the form of a series expansion in successive powers of  $(\tilde{x}_m)^{-1}$ :  $e_m = \sum_{n=0}^{+\infty} e_m^n (\tilde{x}_m)^{-n}$ . Therefrom the expansion coefficients of the extrema locations  $x_m = \sum_{n=-1}^{+\infty} x_m^n (\tilde{x}_m)^{-n}$  can be immediately deduced:  $x_m^{-1} = \tilde{x}_m$ ,  $x_m^n = -e_m^n$  ( $n \geq 0$ ).

We show now that using basic z-Transform techniques allows to derive the coefficients of the expansions. Changing  $\tilde{x}_m$  into  $z_m$  for this purpose and leaving out the index  $m$  for the coefficients are independent of  $m$ , eqn 12 takes the form

$$\tan e = \frac{1}{2(z - e)} \quad (14)$$

Calculating the first derivative of  $e$  leads to

$$[1 - 4(z - e)^2] \frac{de}{dz} = 2 \quad (15)$$

Interpreting eqn 15 by using basic z-Transform properties allows the straightforward computation of the expansion coefficients of  $e$  through the following relation (where  $n$  in

$e^n$  denotes an upper index)

$$e^n = \frac{n-2}{4n} e^{n-2} + \frac{2}{n} \sum_{j=0}^{n-1} j e^j e^{n-1-j} \dots - \frac{1}{n} \sum_{j=0}^{n-2} \left[ \sum_{k=0}^j e^k e^{j-k} \right] (n-2-j) e^{n-2-j} \quad (16)$$

if  $n$  odd ( $n \geq 3$ ) with  $e^1 = 1/2$ , and  $e^n = 0$ , if  $n$  even. Therefore the expansion of  $x_m$  begins as follows

$$x_m = \tilde{x}_m - \frac{1}{2}(\tilde{x}_m)^{-1} - \frac{5}{24}(\tilde{x}_m)^{-3} \dots - \frac{83}{480}(\tilde{x}_m)^{-5} - \frac{2407}{13440}(\tilde{x}_m)^{-7} - \dots \quad (17)$$

#### III.2.2. Algebraic approximation

By limiting this expansion, simple closed-form approximations are obtained for  $x_m$ . Table 4 shows the values obtained for  $x_0$ ,  $x_1$ ,  $x_2$  using the successive terms of the series expansion; the table starts with  $x_m \simeq \tilde{x}_m$  at rank  $p = 0$  ( $n = 2p - 1$ ). It can be observed for example that after only two ranks, the relative error of the very simple algebraic approximation  $x_m \simeq \tilde{x}_m - \frac{1}{2}(\tilde{x}_m)^{-1} - \frac{5}{24}(\tilde{x}_m)^{-3}$  is less than  $2.85 \times 10^{-2}$ ,  $1.70 \times 10^{-5}$  and  $7.56 \times 10^{-7}$ , for  $m = 0, 1$  and  $2$  respectively. On the other hand, a relative error of less than  $10^{-6}$  is obtained after 21, 3 and 2 ranks, for  $m = 0, 1$  and  $2$  respectively. So, apart the case  $m = 0$ , the convergence is very fast. The relatively low convergence of the series expansion for  $m = 0$  is mainly due to the fact that  $\tilde{x}_0 = \pi/2$  presents a value not much higher than 1, unlike  $\tilde{x}_m$  for  $m > 0$ . It can be observed that very simple algebraic approximations offer accurate results for  $x_m$ , except to some extent for  $m = 0$ .

Table 4. Successive values for  $x_0$ ,  $x_1$ ,  $x_2$

$p$	$x_0$	$x_1$	$x_2$
0	1.570796327	4.712388980	7.853981634
1	1.252486441	4.606285685	7.790319657
2	1.198733883	4.604294850	7.789889636
3	1.180652258	4.604220440	7.789883850
4	1.173062329	4.604216969	7.789883753
$\infty$	1.165561185	4.604216777	7.789883751

### III.3. Amplitudes of the extrema

#### III.3.1. Series expansion

Using the same approach, the extrema themselves can be directly calculated. From eqn 12, their amplitudes are  $y_m = 4x_m/(1 + 4x_m^2)$ . Assuming that  $y_m$  can be expanded under the

form  $y_m = \sum_{n=0}^{+\infty} y_m^n (\tilde{x}_m)^{-n}$ , and changing  $\tilde{x}_m$  into  $z_m$ , eqns 14 and 15 lead to the simple following equation ( $m$  is omitted as above)

$$(1 - \frac{de}{dz})y + 2(z - e)\frac{de}{dz} = 0 \quad (18)$$

Interpreting eqn 18 by using basic z-Transform properties allows here the straightforward computation of the expansion coefficients of  $y_m$  through the following relation (where  $n$  in  $y^n$  or  $e^n$  denotes an upper index)

$$y^n = 2ne^n - \sum_{j=0}^{n-1} (n-1-j)e^{n-1-j}(y^j + 2e^j) \quad (19)$$

if  $n$  odd with  $y_m^1 = 1$ , and  $y_m^n = 0$ , if  $n$  even. Therefore the expansion of  $y_m$  begins as follows

$$y_m = (\tilde{x}_m)^{-1} + \frac{1}{4}(\tilde{x}_m)^{-3} + \frac{7}{48}(\tilde{x}_m)^{-5} \dots \quad (20)$$

$$\dots + \frac{37}{320}(\tilde{x}_m)^{-7} + \frac{8723}{80640}(\tilde{x}_m)^{-9} + \dots$$

### III.3.2. Algebraic approximation

By limiting this expansion, simple closed-form approximations are obtained for  $y_m$ . Table 5 shows the values obtained for  $y_0, y_1, y_2$  using the successive terms of the series expansion; the table starts with  $y_m \simeq (\tilde{x}_m)^{-1}$  at rank  $p = 0$  ( $n = 2p + 1$ ). It can be observed for example that after only two ranks, the maximum relative error of the simple algebraic approximation  $y_m \simeq (\tilde{x}_m)^{-1} + \frac{1}{4}(\tilde{x}_m)^{-3} + \frac{7}{48}(\tilde{x}_m)^{-5}$  is less than  $1.14 \times 10^{-2}$ ,  $1.09 \times 10^{-5}$  and  $4.99 \times 10^{-7}$ , for  $m = 0, 1$  and  $2$  respectively. On the other hand, a relative error of less than  $10^{-6}$  is obtained after 17, 3 and 2 ranks, for  $m = 0, 1$  and  $2$  respectively. So, apart the case  $m = 0$ , the convergence is very fast. The relatively low convergence of the series expansion for  $m = 0$  is mainly due to the fact that  $\tilde{x}_0 = \pi/2$  presents a value not much higher than 1, unlike  $\tilde{x}_m$  for  $m > 0$ . It can be observed that very simple algebraic approximations offer accurate results for  $y_m$ , except to some extend for  $m = 0$ .

Table 5. Successive values for  $y_0, y_1, y_2$

$p$	$y_0$	$y_1$	$y_2$
0	0.6366197724	0.2122065908	0.1273239545
1	0.7011228412	0.2145955933	0.1278399790
2	0.7163724049	0.2146583487	0.1278448589
3	0.7212725914	0.2146605893	0.1278449216
4	0.7231305518	0.2146606837	0.1278449226
$\infty$	0.7246113538	0.2146606884	0.1278449226

## IV. CONCLUSION

Methods for the computation of the extrema of the function  $(\sin x/x)^r$  and the function  $(\sin^2 x)/x$  have been presented. In both cases, the extrema locations and amplitudes are expressed under the form of series expansions. By exploiting Z-transform techniques, it is shown that the expansions coefficients can be obtained through straightforward recursive relations which can be easily implemented on a computer or a DSP. Very simple algebraic expressions are derived which give accurate values of the extrema locations and amplitudes, using only a very few coefficients - except, as far as  $(\sin^2 x)/x$  is concerned, in the case of the first extremum.

For  $(\sin x/x)^r$  as well as for  $(\sin^2 x)/x$ , both methods (recursive relations and algebraic expressions) can be useful for various applications in different domains such as signal processing and communications, but also in other fields of physics or engineering.

## REFERENCES

- [1] H. Stark, F. B. Tuteur, and J. B. Anderson, Modern electrical communications, Englewood Cliffs : Prentice Hall, 1988
- [2] J. G. Proakis, and M. Salehi, Communications systems engineering, Englewood Cliffs : Prentice Hall, 1994
- [3] M. Kunt, Traitement numérique des signaux, Lausanne : Presses Polytechniques et Universitaires Romandes, 3e éd., pp. 107-123, 1999
- [4] S. Haykin, Communication systems, New York : John Wiley & Sons, 3rd ed., ch. 4, pp. 242-264, 1994
- [5] N. C. Beaulieu, "Extrema of  $\sin x/x$  function", Electron. Lett., vol. 31, 15, 1995, p. 1215
- [6] J. Le Bihan, "Straightforward recursive relations for computing the locations and amplitudes of the  $\sin x/x$  function's extrema", Electron. Lett., vol. 34, 25, 1998, pp. 2385-2386
- [7] J. Le Bihan, "Efficient recursive relations and accurate algebraic expressions for computing the extrema of  $(\sin x/x)^r$ ", Electron. Lett., vol. 38, 23, 2002, pp. 1485-1486

---

# A surgical planning software for orthopedic applications and its possible use in telemedicine

## Session Telemedicine

M.Schlimbach<sup>1</sup>, J.Wahrburg<sup>1</sup> H.Roth<sup>1</sup>

<sup>1</sup> University of Siegen, Center for sensor systems,  
Paul Bonatz Straße 9 - 11, D-57076 Siegen  
schlimbach@zess.uni-siegen.de

### INTRODUCTION

With planning software a time-efficient and careful preoperative planning of surgical interventions is possible. Digital planning helps to fulfill the risen requirements to the documentation of operational interventions in the future. In addition the X-Ray foils in the course of digital x-ray units and screen-supported finding stations will ever more disappear.

In this paper on the basis of modiCAS-Planning the modules are described, which should be present in surgical planning software.

modiCAS® is a software framework, which supports the different steps of a surgical interference of preoperative planning over intraoperative navigation up to a mechatronic assistant system. By the modular and universal approach, which is pursued with the modiCAS project, it is possible to use the software for the planning of many different surgical interferences. The current main point of research lies in the hip endoprothetics.

### COMPOSITOIN OF A PLANNING SOFTWARE

The planning software of the modiCAS project is modular developed. The central component contains graphic user interface and visualization. In order to ensure a fast and simple planning process, user-defined workflows can be defined.

For communication with picture servers a DICOM - interface is implemented. Over this interface graphic data will be loaded from a PACS system. Although finished plannings will be send to the PACS system through this interface. ModiCAS-Planning supports different modalities. With the hip and knee endoprothetics radiographs presents the state of the art.

In the planning process it is necessary to measure distances to put on lines or measure angles. These functions are realized in the module of planning objects. This module could be extended by new planning objects, if it is required.

Beside the planning objects also models of the implants are needed. These models can be present in the form of 2D- or 3D-Daten. Due to the large number of implants it is useful to administer the implant data in a data base. This data base illustrates likewise dependence between the individual implants.

Depending upon task and the preoperative existing graphic data for the time of planning not all necessary informations are available to provide an optimal planning. For this reason it is meaningful to complete planning intraoperativ. The necessary interfaces to navigation systems or intraoperativ existing picture-giving procedures must be created.

### GOALS

It is our next goal to design a software framework for online discussion of medical plannings based on our existing framework. The users of this system should be able to make a surgical planning at different locations and to discuss their planning with other users via tele communication systems.

It is new that a whole planning of a surgical intervention will be the base for a discussion. Existing solutions allows it to discuss only 2D or 3D images. With the new solution each member of the discussion round should be able to modify the discussed planning online and visible to all other users.

### CONCLUSIONS

In future digital planning will become ever more important. For an optimal work routine planning programs can be attached to PACS of systems.

For the acceptability it is important that the physician need no longer time as when he makes a conventional planning.

In order to reduce the expenditure of time further, semi automatically assistant functions offers a much promising starting point.

Further advantages arise as a result of the better documentation in the quality management and with forensic aspects.

### REFERENCES

[Wahrburg2001]Wahrburg, J.; Gross, I.: "Computer assisted planning for total hip replacement procedures based on multiple 2D images", Computer Assisted Orthopaedic Surgery Meeting CAOS/USA 2001, Pittsburgh, USA, 06 – 08 July 2001

## AUTHOR INDEX

BEKIARSKA S.	43
BEKIARSKI A.	21
BONCHEV B.	58, 62
BOULTADAKIS G.	25
CERNY M.	69
DAMIANOV D.	43
DECHEVA P.	6
DEKERIS B.	54
DEMIREV V.	1
DIMITROV D. TZ.	6, 13, 16
DONTSCHewa M.	16
DUMBRAVA V.	31
N. DUBAUSKIENĖ	81
FLODER J.	69
FRANGOS P.	25
GAVRILOV M.	6
GRAU M.	21
HRISTOV V.	66
JONYNAS V.	81
KARAKASILLOTIS A.	25
LAZAROV A.	25
LE BIHAN J.	74
MARKEVIČIUS V.	81
MORKVENAS R.	88
MOTIEJUNAS G.	31
NACHEVA I.	21
NARBUTAITE L.	54
D. NAVIKAS	81
PENHAKER M.	69
PETROVA P.	13
POPOVSKI B.	47
PORJAZOSKI M.	47
ROSULEK M.	69
ROTH H.	80
SCHLIMBACH M.	80
SINKUNAS L.	37
SVEIKATA J.	88
SVILAINIS L.	37
TONEV B.	13
VALINEVIČIUS A.	81
VENKOV P.	21
ZAJCHEVA S.	16
WAHRBURG J.	80